Stochastic Acoustic Ray Tracing with Dynamically Orthogonal Equations

by

Michael Jesus Humara

B.S., United States Naval Academy, 2007

Submitted to the Joint Program in Applied Ocean Science & Engineering
in partial fulfillment of the requirements for the degree of

Master of Science, Mechanical Engineering

at the

MASSACHUSETTS INSTITUTE OF TECHNOLOGY

and the

WOODS HOLE OCEANOGRAPHIC INSTITUTION

May 2020

Author .....

Joint Program in Applied Ocean Science & Engineering
Massachusetts Institute of Technology
& Woods Hole Oceanographic Institution
May 15, 2020

Certified by .....

Pierre Lermusiaux
Professor of Mechanical Engineering and Ocean Science and Engineering
Associate Department Head for Research and Operations
Massachusetts Institute of Technology
Thesis Supervisor

Accepted by .....

Nicolas Hadjiconstantinou
Chairman, Committee for Graduate Students
Massachusetts Institute of Technology

Accepted by .....

David Ralston
Chairman, Joint Committee for Applied Ocean Science & Engineering
Woods Hole Oceanographic Institution

Stochastic Acoustic Ray Tracing
with Dynamically Orthogonal Equations

by

Michael Jesus Humara

Submitted to the Joint Program in Applied Ocean Science & Engineering
Massachusetts Institute of Technology
& Woods Hole Oceanographic Institution
on May 15, 2020, in partial fulfillment of the
requirements for the degree of
Master of Science, Mechanical Engineering

Abstract

Developing accurate and computationally efficient models for ocean acoustics is inherently challenging due to several factors including the complex physical processes and the need to provide results on a large range of scales. Furthermore, the ocean itself is an inherently dynamic environment within the multiple scales. Even if we could measure the exact properties at a specific instant, the ocean will continue to change in the smallest temporal scales, ever increasing the uncertainty in the ocean prediction. In this work, we explore ocean acoustic prediction from the basics of the wave equation and its derivation. We then explain the deterministic implementations of the Parabolic Equation, Ray Theory, and Level Sets methods for ocean acoustic computation. We investigate methods for evolving stochastic fields using direct Monte Carlo, Empirical Orthogonal Functions, and adaptive Dynamically Orthogonal (DO) differential equations. As we evaluate the potential of Reduced-Order Models for stochastic ocean acoustics prediction, for the first time, we derive and implement the stochastic DO differential equations for Ray Tracing (DO-Ray), starting from the differential equations of Ray theory. With a stochastic DO-Ray implementation, we can start from non-Gaussian environmental uncertainties and compute the stochastic acoustic ray fields in a reduced order fashion, all while preserving the complex statistics of the ocean environment and the nonlinear relations with stochastic ray tracing. We outline a deterministic Ray-Tracing model, validate our implementation, and perform Monte Carlo stochastic computation as a basis for comparison. We then present the stochastic DO-Ray methodology with detailed derivations. We develop varied algorithms and discuss implementation challenges and solutions, using again direct Monte Carlo for comparison. We apply the stochastic DO-Ray methodology to three idealized cases of stochastic sound-speed profiles (SSPs): constant-gradients, uncertain deep-sound channel, and a varied sonic layer depth. Through this implementation with non-Gaussian examples, we observe the ability to represent the stochastic ray trace field in a reduced order fashion.

Thesis Supervisor: Pierre Lermusiaux
Title: Professor of Mechanical Engineering and Ocean Science and Engineering
Associate Department Head for Research and Operations
Massachusetts Institute of Technology

Acknowledgments

First, thank you to the U.S. Navy's Civilian Institution Program along with the MIT-WHOI Joint Program for providing the funding and resources that made this research possible. I am also grateful to the U.S. Navy Submarine Force for continuing to provide the opportunity and challenge of working alongside some of the brightest people, this time at two world-class institutions.

Thank you to Dr. Pierre Lermusiaux, my research advisor, for his mentorship, guidance, and flexibility throughout my time in the Joint Program as a member of the Multidisciplinary, Simulation, Estimation, and Assimilation Systems (MSEAS) laboratory. While also a leader of the Mechanical Engineering Department at MIT, with a busy and demanding schedule, he made my research, as well as my personal and professional development, a top priority. He empowered me to leverage Navy experience to gain insight into research topics, to participate in Task Force Ocean related projects, and gave me a better understanding of the benefits and challenges of collaboration between academia and the Department of Defense.

Thank you to my MSEAS labmates for the interesting discussions, the shared frustration and levity, and your time. Specifically thank you to Wael Haj Ali, Manmeet Bhabra, and Abhinav Gupta. Without these remarkable individuals' assistance and support this research would not have been possible. They always provided their time to provide insight, correction, and stimulation to my research, while completing demanding research of their own. I am truly grateful for their support and friendship.

Thank you to all of the MIT/WHOI staff, and specifically Dr. Andone Lavery, Dr. Arthur Baggeroer, and Dr. Henrik Schmidt for their support and guidance upon arriving to the Joint Program. Their direction was instrumental at reorienting me to academia and ensuring I was set up for success. Thank you to Lisa Cherin-Mayer, Pat Haley, and Chris Mirabito for the assistance and expertise you provide to MSEAS.

PFJL and the MSEAS group are grateful to the Office of Naval Research for support under Grants N00014-19-1-2664 (Task Force Ocean: DEEP-AI) and N00014-19-1-2693 (IN-BDA) to the Massachusetts Institute of Technology (MIT).

Most of all thank you to my beautiful wife and children. You give me purpose, inspiration, and the love that make all endeavours worthwhile. Our family will always be my greatest source of pride and satisfaction.

THIS PAGE INTENTIONALLY LEFT BLANK

Contents

THIS PAGE INTENTIONALLY LEFT BLANK

List of Figures

THIS PAGE INTENTIONALLY LEFT BLANK

Chapter 1

Introduction

1.1 Motivation

In December of 2018, the Chief of Naval Operations, Admiral Jon Richardson, issued *A Design for Maintaining Maritime Superiority 2.0* to update "...the framework to guide [United States Navy] behaviors and investments." He places specific emphasis on enhancing the "cooperation with academic and research institutions" and the "fielding of [Artificial Intelligence (AI) and Machine Learning (ML)] algorithms on areas that most enhance warfighting [73]." Since releasing this update, the Navy has established and funded the Task Force Ocean (TFO) program to enable academic and research institutions to "initiate new research to better understand and exploit the ocean environment." TFO directs "exploration of analytic techniques linking physical oceanographic variability with acoustic propagation" as one of a few high priority areas for research [67]. This high priority area is the motivation of the present research. One of the present goal is to research, study, and implement innovative computational techniques for principled uncertainty quantification, inference and learning, with the long term vision of enabling and enhancing AI and Machine Learning for naval applications, promoting U.S. Navy goals and overall understanding of the undersea environment.

Due to the relatively high attenuation of visible electromagnetic radiation, acoustic waves are a primary means of observing ocean features, identifying foreign objects, and undersea communication. While acoustic propagation is a means of achieving these objectives, a significant drawback is that acoustic wave propagation is largely dependent on the environment or medium, hence efficient prediction of underwater sound propagation is a non-trivial

matter [32]. In general, modeling the ocean environment is difficult for a number of reasons. The ocean is highly variable, over a very wide range of length and time scales and it is impractical for direct and complete measurements, even with advances in satellite and other remote sensing capabilities. Even with the ability to measure, there exists uncertainty in the measured quantities due to instrument performance and the veracity of the measurement with respect to the desired observation [16]. All of these uncertainties, when input to ocean modeling, can evolve and nonlinear interact, leading to uncertainty growth and limited predictive capabilities [75, 46, 43]. As the ocean fields are commonly input to ocean acoustic modeling, there is a transfer of uncertainties to underwater sound propagation modeling that can result in multiple acoustic propagation regimes. As a result, there are compounded complexities and uncertainties when modeling and predicting ocean acoustic propagation, over a wide range of spatial and temporal scales [28, 47, 76, 72, 40, 100, 53, 89].

Ocean scientists commonly combine measurements and other data with physical conservation laws to derive deterministic models of the ocean acoustic environment. Due to the inherently unknown initial ocean state, it is useful in terms of forecasting or prediction to utilize the data and conservation laws to obtain stochastic models (deterministic+statistics, see [31, 53]) where we not only have a dynamically evolving representation of the environment, but also an understanding of the uncertainty in our predictions due to the uncertain inputs and parameters, model formulations, parameterizations, and other unresolved processes. This stochastic modeling enables the quantification and forecast of probabilities of ocean and acoustic fields. When observations are made, these prior forecast probabilities then also allow data assimilation to improve the nowcasts and forecasts of how sound may propagate and also include some assessment of the reliability of these estimates [77, 47, 44]. This can be done in real-time while at at-sea [40, 53]. A related powerful application is the use of travel times and other acoustic measurements to infer ocean physics fields using acoustic tomography [30, 65, 14]. With all of this in mind, research has evolved to include adaptive sampling concepts such as Adaptive Rapid Environmental Assessment (AREA), where data-assimilation is enhanced by in-situ optimal sampling algorithms to improve acoustic predictions with limited resources (time or energy) [100]. This all begins with our ability to accurately characterize the ocean environment according to measurable parameters and how they affect the sound-speed, to accurately describe the variability in those parameters, model the acoustic propagation, and finally provide an uncertainty characterization or pre-

diction using an end-to-end modeling system [76]. In the next few paragraphs we provide an overview of these components and related tasks, including ocean sound speed estimation, acoustic modeling, uncertainty quantification, and reduced-order modeling.

The variation in ocean acoustic propagation is attributed to the different sound speed properties. Specific undersea acoustic environments are challenging to model or characterize as they require knowledge of three independent parameters: temperature (T in °C), salinity (S in parts-per-thousand), and pressure/depth (z, meters). A commonly used equation to model the relationship of these three parameters to sound speed c is [64]

$$c(r,z) = 1449.2 + 4.6T - 0.055T^2 + 0.00029T^3 + (1.34 - 0.01T)(S-35) + 0.016z \quad (1.1)$$

The term Sound Speed Profile (SSP) describes how the sound speed varies in depth (z) and range (r) and can be depicted as a function or table. In physical and mathematical terms, it is a field varying in space and time. Even if the environment can be accurately measured to produce an accurate representation of the above parameters for a given time over a specified region, ocean acoustic computation remains challenging when considering sub-mesoscale to mesoscale distances ($\sim$ 1 to 100 km) or greater. For common numerical methods such as finite differences, finite volumes, or finite elements, the spatial discretization of the computational domain must be a fraction of the acoustic wavelength (λ) [32]. Shown in (1.2)Assuming a nominal sound speed (c) of 1500 m/s and a signal frequency (f) as low as 1 kHz, the discretization of a 10 km (range) by 3 km (depth) would need to be on the order of less than 1m resulting in exorbitant computational cost.

$$\lambda = \frac{c}{f} = \frac{1500(\frac{m}{s})}{1 \times 10^{-3}(s^{-1})} = 1.5m \quad (1.2)$$

As a result, several simplifications are made to achieve acoustic models that can be utilized in pratice.

Some of the practical acoustic models and computational methods developed specifically for underwater sound propagation include the Wavenumber Integration (Fast-Field Methods), Multipath Expansion (WKB), Normal Modes, Ray Methods, and Parabolic Equations [32]. These methods will each possess benefits and drawbacks in their implementations depending on the acoustic regime they aim to characterize (e.g. high/low frequency, 2/3-D, etc.). Figure 1-1 provides an overview of applications and where these methods may

apply. While the methods in Fig. 1-1 effectively compute expected acoustic propagation,

Model type	Applications							
	Shallow water				Deep water			
	Low frequency		High frequency		Low frequency		High frequency	
	RI	RD	RI	RD	RI	RD	RI	RD
Ray theory	○	○	◑	●	◑	◑	●	●
Normal mode	●	◑	●	◑	●	◑	◑	○
Multipath expansion	○	○	◑	◑	◑	◑	●	◑
Fast field	●	◑	●	◑	●	◑	◑	◑
Parabolic equation	◑	●	○	○	◑	●	◑	◑

Low frequency (<500 Hz)
High frequency (>500 Hz)

RI: Range-independent environment
RD: Range-dependent environment

● Modeling approach is both applicable (physically) and practical (computationally)

◑ Limitations in accuracy or in speed of execution

○ Neither applicable nor practical

Figure 1-1: Domains of Applicability of Underwater Acoustic Propagation Models. Adapted from [23].

they are deterministic in nature - they are defined for one ocean environment at a specific time without uncertainty quantification. Since the undersea environment is highly variable and governed by complex partial differential equation models with significant uncertainties in the initial and boundary conditions, parameters values, and functional forms, the stochastic, thus the SSP is stochastic as in Figure 1-2, forecasting or predicting the acoustic environment requires stochastic computational methods.

Given sufficient time and computational power, applying any of the mentioned acoustic

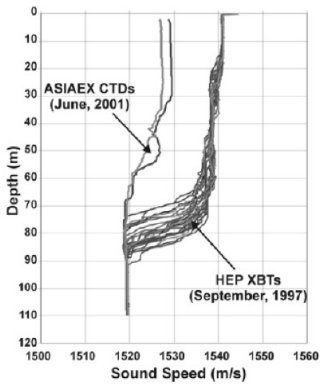

Figure 1-2: SSPs derived from CTD and XBT casts off the R/V Melville in the East China for separated acoustic studies conducted by Ocean Acoustics Services and Instrumentation Systems (OASIS). Adapted from[1].

computational methods in a Monte-Carlo fashion may be feasible and provide a straight forward means of producing acoustic forecasts that accurately capture the uncertainty in the ocean environment and its effects on acoustic propagation. However, when power and time are restricted, such as in autonomous applications, it is necessary to provide reduced-order representations of the ocean acoustic uncertainty. For example, consider two autonomous vehicles required to communicate over mesoscale distances in a variable ocean environment. With respect to the forward problem (how an acoustic signal will propagate from transmitter to the receiver), in order to appropriately position itself to transmit or receive acoustic signals, the vehicle should place itself where it has the best probability of receiving the signal given the uncertainties in the ocean environment. Figure 1-3 depicts a simplified scenario with two possible sound propagation regimes in the arctic. In this case with each regime being equally likely, a vehicle desiring to receive the signal should place itself at a depth less than 100 m to have a better probability of reception. Possibly more interesting, consider a backward problem. If a signal parameter (e.g. travel time) can be measured, this parameter may enable the vehicle to infer a more accurate real-time representation, with associated uncertainty, of the ocean environment through which the signal traveled and an estimate of the signal transmitters position.

There are several computational methods for reduced order modeling and uncertainty quantification. Empirical Orthogonal Functions, also known as Principle Component Analysis, derived from direct measurement, provides a means of capturing variablity in SSPs while reducing the number of computations [103]. We could also consider spectral methods that allow us to exploit the statistics [41]. The stochastic Dynamically Orthogonal differential equations have been derived to evolve stochastic fields while preserving its dominant statistics [78, 97, 25]. With such stochastic predictions, we can use our gained knowledge of the forecast probability distributions to complete non-Gaussian Bayesian data assimilation [80, 58] and optimize the data collection using information-based adaptive sampling and principled model learning [44, 50, 48].

This thesis explores and applies stochastic differential equations and computational methods for underwater acoustic computation pertaining to travel times of signal propagation. For the first time, it then implements and evaluates the method of dynamically orthogonal equations (DO) to acoustic ray tracing (DO-Ray) with a comparison to results obtained from a validated Monte-Carlo computation. This method provides a means of cap-

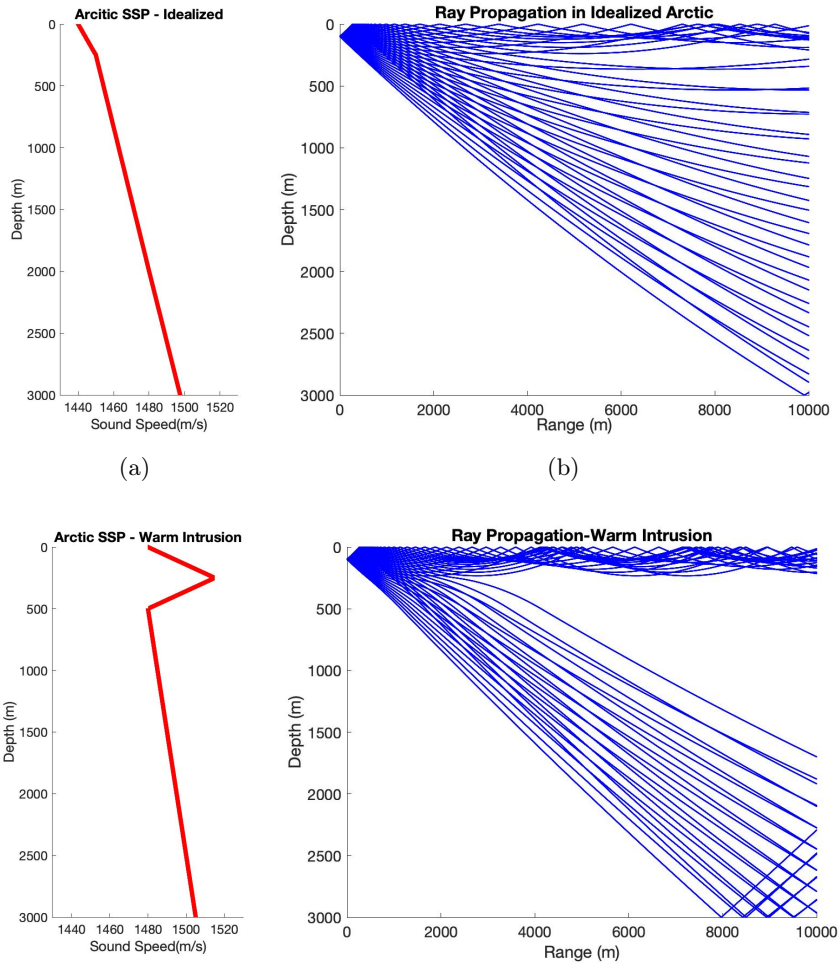

(a) (b)

(c) SSP (d) Ray Trace Plot

Figure 1-3: The typical or ideal Arctic environment consists of a positive sound speed gradient yeilding ray paths that transit throughout the depth of the water column. The warm water intrusion depicted in (c) result in a higher sound speed in the upper portion of the water column resulting in sound being refracted away from the maximum sound speed.

turing the stochastic variation in an ocean's acoustic propagation due to an uncertain SSP, using a dynamic reduced oder representation of the stochastic ray field. Given the ability to efficiently compute ray traces for thousands of ocean environments, we could then extend the algorithm to compute acoustic wave travel times or even intensity.

1.2 Thesis Overview

This thesis utilizes the common acoustic computation methodology, Ray Tracing, with the stochastic computational method Dynamically Orthogonal Equations (DO-Ray) to obtain reduced order representations of an ensemble of ocean acoustic environments. For comparison and validation, it also implements a deterministic ray tracing computation scheme in order to produce individual realizations to compare with the new methodology. The DO-Ray methodology allows for the simultaneous computation of thousands of ocean environments, whose SSP distribution may be Gaussian or non-Gaussian.

Chapter 2 begins with the basic theory of wave propagation in underwater acoustics. The application of numerical methods methods in this thesis emphasizes the prediction and measurement of ocean acoustics travel time. For implementation, Ray methods, specifically ray tracing, is selected, with a focus on higher acoustic frequencies. Other ocean acoustic computational methods can be used to compute travel time but present their own computational challenges. For reference, Chapter 2 includes a review of the most common method Parabolic Equations, and a less known method method of prediction acoustic wave fronts based on Level Sets. Lastly, Chapter 2 highlights three methods of stochastic computation used by ocean acousticians to represent multiple acoustic propagation environments. It finishes with a background on the dynamically adaptive stochastic methodology to be implemented, the DO differential equations.

Chapter 3, on the stochastic DO-Ray Methodology, presents the how the combined methods of Ray Tracing and DO differential equations are implemented and validated. It includes how a deterministic algorithm is implemented and validated to form a basis for comparison. The chapter includes the detailed derivation for DO-Ray and is immediately followed by a detailed explanation of some of the terms and what they imply. Chapter 3 finishes with sections detailing unique computational or numerical challenges associated with the presently implemented algorithms as well an assessment of feasibility and convergence

to Monte-Carlo implementations.

Chapter 4 presents the results of stochastic DO-Ray implementation with three constructed scenarios or regimes of sound speed variability: Constant Gradient, Deep Sound Channel, and Sonic Layer Depth. Each scenario contains thousands of realizations of possible SSPs from which individual realizations can be constructed using the DO-Ray method and compared to individual realizations computed by deterministic method.

Chapter 5 discusses this thesis's conclusions and highlights a few areas for future work. DO has been implemented for several other stochastic problems and enhanced with tools for data-assimilation. With a computationally efficient and accurate DO-Ray implementation, we could apply these schemes to realistic ocean acoustic conditions and utilize the existing non-Gaussian data-assimilation tools. We would then improve our ability to characterize and predict stochastic ocean acoustics environments, with a wide range of real scientific and naval applications.

Chapter 2

Background

2.1 Basic Acoustic Wave Theory

To better understand the complexity of Ocean Acoustic Computation, we first review the underlying physics and equations associated with acoustic propagation. Notations can be a complicating factor; therefore, we lay out the equations in a selected notation in which the remaining derivations will be annotated. The Cartesian system is chosen as the default in this thesis; alternate coordinate systems will be specifically identified when used. For consistency, once a variable is assigned a definition, it will remain that variable for the remained of this thesis.

2.1.1 Wave Equation Foundations

There are multiple ways to mathematically derive the acoustic wave equation both with or without physical intuition. To establish the foundation of the acoustic wave equation as well as viable definitions, we will start from mathematical conservation laws, augmented with an equation of state. The result will be a 3-D wave equation that relates density to pressure.

The first and most simple derivation of what we will refer to as the wave equation is a routine exercise in calculus is now summarized. We consider an continuous function of both space and time that represents a 1-D wave whose amplitude in space is parameterized by time (see Figure 2-1): $g(s) = g(x - ct)$. By taking the derivative with respect to space (x), and applying the chain rule, we obtain

$$\frac{\partial^2 g(s)}{\partial x^2} = \frac{\partial^2 g(s)}{\partial s^2} \,. \tag{2.1}$$

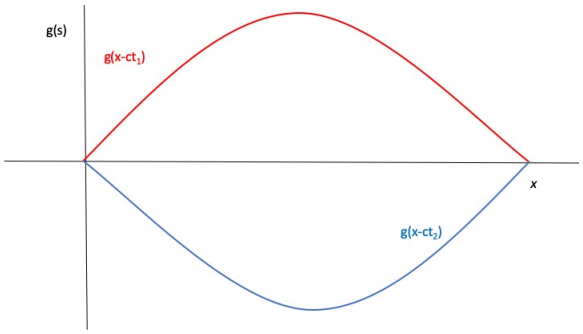

Figure 2-1: 1-D Wave parameterized by time (t) at $t = t_1$ and $t = t_2$

By letting $c^2 = (\partial^2 g(s))/(\partial s^2)$, taking derivativea with respect to time (t), and applying the chain rule, we obtain

$$\frac{1}{c^2}\frac{\partial^2 g(s)}{\partial t^2} = \frac{\partial^2 g(s)}{\partial s^2}\,. \tag{2.2}$$

This is what is commonly known as the second-order 1-D wave equation:

$$\frac{\partial^2 g(x-ct)}{\partial x^2} = \frac{1}{c^2}\frac{\partial^2 g(x-ct)}{\partial t^2}\,. \tag{2.3}$$

In order for a function to satisfy the wave equation it must satisfy the above property. For example, consider a sine wave traversing in space and time with amplitude (A) wave, wave number k, and radial frequency ω:

$$g(x-ct) = A\sin\left(kx-\omega t\right) \tag{2.4}$$

By taking the requisite partial derivative to both sides of (2.4), we observe that (2.4) satisfies the 1-D wave equation (2.2).

This simple derivation is useful in gaining some basic understanding of wave propagation; however, it is the most general application and does not provide intuition or insight into the physics of underwater sound. To understand ocean acoustics, and how the properties of the medium affect it, it is more relevant to derive a three dimensional understanding of the wave equation propagating through a medium. Ultimately we desire an equation that relates the relevant properties of the medium (density) to the parameters of the acoustic field. Depending on the intended application, the 3-D equation can be derived into several forms [32] including for pressure, particle velocity, velocity potential, or displacement potential. While all of these forms are valid, the most useful representation for later derivations is the

pressure representation.

The derivation begins with two governing hydrodynamic conservation equations, mass and momentum, applied to a mass of the medium through which the wave travels. From this point on, we also assume that the medium is seawater and consider the corresponding equation of state. As a whole, we have,

Conservation of Mass:

$$\frac{d\rho}{dt} + \nabla(\rho\overline{V}) = 0 \tag{2.5}$$

Conservation of Momentum:

$$\rho\frac{D\overline{U}}{Dt} = -\nabla p \tag{2.6}$$

Equation of State (Taylor series expansion):

$$\rho = \rho(p) + (p - p_0)\frac{d\rho(p_0)}{dp} + \frac{(p - p_0)^2}{2!}\frac{d^2\rho(p_0)}{dp^2} + \dots \tag{2.7}$$

where ρ is the fluid density, p is pressure, $\overline{V}$ is the 3-D volumetric flow rate of the seawater, and $\overline{U}$ is the 3-D particle velocity that incorporates both particle speed and the fluid speed. The subscript "0" indicates that this is the reference parameter of a reference ocean's properties (i.e. without the propagating sound wave). Sound is produced by the natural or artificial phenomena of forced mass injection [32]. Therefore, assume a small mass injection causes small perturbations denoted by the subscript "1." Hence:

$$p = p_0 + p_1 \tag{2.8}$$

$$\overline{U} = \overline{U}_0 + \overline{U}_1 \tag{2.9}$$

$$\rho = \rho_0 + \rho_1 \tag{2.10}$$

Assume that the perturbation in density (ρ_1) is much smaller than ρ_0, synonymous with seawater being nearly incompressible, and that the reference particle velocity is zero. We then have:

$$\rho_0\overline{U}_1 >> \rho_1\overline{U}_1 \tag{2.11}$$

and

$$\frac{\partial\rho_0}{\partial t} = 0 \tag{2.12}$$

Applying (2.11) and (2.12), and a first-order approximation of (2.7), we can approximate (2.7) through (2.6) with linearized versions of these three hydrodynamic equations:

Equation of State-Linearized:

$$\rho_1 = p_1 \frac{\partial \rho(p_0)}{\partial p} \tag{2.13}$$

Conservation of Mass-Linearized:

$$\frac{\partial \rho_1}{\partial t} + \rho_0 \nabla \overline{V}_1 = 0 \tag{2.14}$$

Conservation of Momentum-Linearized:

$$\rho_0 \frac{\partial \overline{U}_1}{\partial t} = -\nabla p_1 \tag{2.15}$$

By taking the time derivative of (2.14), the divergence of (2.15), and representing the relation of change in $\frac{\partial \rho}{\partial p}$ as the sound speed of the material squared (c^2), the final 3-D acoustic wave equation relating density to pressure is:

$$\nabla^2 p_1 = \frac{1}{c^2} \frac{\partial^2 p_1}{\partial t^2} \tag{2.16}$$

The source of the sound to this point has been left unaddressed, but for now we will rearrange (2.16) to include a time harmonic source where the amplitude (S_f) is a function of range. The computed source level ($s(\mathbf{x}, t)$) in the acoustic field is then also a function of position in relation to the source and time:

$$\nabla^2 p_1 - \frac{1}{c^2} \frac{\partial^2 p_1}{\partial t^2} = s(\mathbf{x}, t) = S_f(\mathbf{x}) e^{-i2\omega t} \tag{2.17}$$

2.1.2 Helmholtz Equation

There are several important points to make regarding the acoustic wave equation in the form presented in (2.16). As mentioned in Chapter 1, though (2.16) appears to be amenable to classical or relatively straight forward computational methods such as finite differences or finite elements, the resolution of the 3-D domain would have to be a fraction of the acoustic wavelength. Also, if solved in a 3-D spatial domain with a given time step, the time domain compounds the complexity and computational expense. The majority of modern

computational methods begin with a simple dimension reduction of (2.16) to an equation known as the Helmholtz Equation. The only coefficient in front of the differential operators is a function of the sound speed. While the sound speed can be variable spatially, due to the fast underwater sound-speed, it can be assumed to not vary with time. This is the so-called frozen-ocean approximation [37, 32]. By application of Fourier Transform, it allows to easily alternate between the time and frequency domains, with the following transforms:

$$f(t) = \frac{1}{2\pi} \int_{-\infty}^{\infty} f(\omega) e^{-i\omega t} d\omega \tag{2.18}$$

and

$$f(\omega) = \int_{-\infty}^{\infty} f(t) e^{-i\omega t} dt \tag{2.19}$$

Through this conversion we achieve a reduction in dimension and obtain a problem simpler to solve for given a specific frequency (ω), the Helmholtz Equation:

$$\nabla^2 p - \frac{\omega^2}{c^2(\mathbf{x})} = S_\omega(\mathbf{x}) \ . \tag{2.20}$$

Moving into the frequency domain thus allows for direct solution methods at discrete frequencies The approach is thus most applicable to narrow-band acoustic applications [32].

The Helmholtz Equation forms the basis of the derivation of several ocean acoustic computational methods, including: Wave-number Integration, Normal Modes, Ray Methods, and the Parabolic Equation.

2.1.3 Source Representation

A practical description of the source represents the sound as being produced by the natural or artificial phenomena of forced mass injection. Several assumptions are then often made about the shape of the source in the time domain [32]. As the methods to be derived are in the frequency domain, the simplest source is represented as a point source at position $\mathbf{x}_0$, and mathematically as a Dirac delta function, resulting in:

$$\nabla^2 p - \frac{\omega^2}{c^2(\mathbf{x})} = -\delta(\mathbf{x} - \mathbf{x}_0) \ . \tag{2.21}$$

2.2 Ocean Acoustic Computational Methods

2.2.1 Parabolic Equation

In 1974, F.D. Tappert wrote about "A New theoretical-numerical method developed which enables one to accurately and efficiently compute the entire two-dimensional low-frequency underwater acoustic field... based on a parabolic equation approximation [90]." In the 1990's, Jensen et al identified the Parabolic Equation Method as becoming "the most popular wave theory technique for solving range-dependent propagation problems in ocean acoustics" [32]. A cursory literature review of ocean acoustics since 2019 up to today yields over 100 publications that use or modify the Parabolic Equation method, making it the most popular as compared to Wavenumber Integration (25), Normal Modes (67), and Ray methods (81). Because of its popularity, the next paragraphs are dedicated to exploring the Parabolic Equation method and its use with Fourier Transforms to compute signal travel times.

The derivation of the Parabolic Equation method presented is the summary of the more detailed derivation provided by Tappert in *"Wave Propagation in Underwater Acoustics"* [91]. Still assuming a time harmonic point source at range = 0 and depth z_s, and shifting to cylindrical coordinates in 2-D (r- cylindrical radius, z - depth), (2.16) becomes:

$$\frac{\partial^2 p}{\partial r^2} + \frac{1}{r}\frac{\partial p}{\partial r} + \frac{\partial^2 p}{\partial z^2} + k_0^2 n^2 p = \frac{-4\pi}{r} S_\omega \delta(z - z_s) \tag{2.22}$$

In (2.22), $k_0 = \frac{\omega}{C_0}$, C_0 is a reference sound speed, and $n = \frac{C_0}{C(r,z)}$ corresponds to the index of refraction.

Away from the source, we define the function u as,

$$p = \frac{u}{\sqrt{r}}\,, \tag{2.23}$$

and make the far-field approximation, $k_0 r >> 1$, to obtain:

$$\frac{\partial^2 u}{\partial r^2} + \frac{\partial^2 u}{\partial z^2} + k_0^2 n^2 p = 0\,. \tag{2.24}$$

We then define the following operators:

$$P = \frac{\partial}{\partial r} \tag{2.25}$$

and

$$Q = (\frac{1}{k_0^2}\frac{\partial^2}{\partial z^2} + n^2)^{1/2} \tag{2.26}$$

which allows us to rewrite (2.24) into

$$(P^2 + k_0^2 Q^2)u = 0\,. \tag{2.27}$$

This is an elliptical equation that can be factored, resulting in a formulation that separately represents the incoming and outgoing portion of a wave:

$$(P + ik_0Q)(P - ik_0Q)u + ik_0[P, Q]u = 0 \tag{2.28}$$

where $[P, Q]$ is referred to as the commutator of operators P and Q, i.e.

$$[P, Q]u = PQu - QPu\,. \tag{2.29}$$

This operator may be ignored in "weakly" range dependent environments. This assumption, and that of a wave that is only outgoing, the Generalized Parabolic Equation is obtained as [17]:

$$Pu = ik_0Qu\,. \tag{2.30}$$

Summarizing to this point in the derivation, (2.30) is now a first-order partial differential equation with respect to r, or "Parabolic" instead of elliptical as in (2.24). Assuming the far-field approximation is valid, it accurately computes outgoing waves by range marching, neglecting any backscatter, with some small error associated by neglecting (2.29).

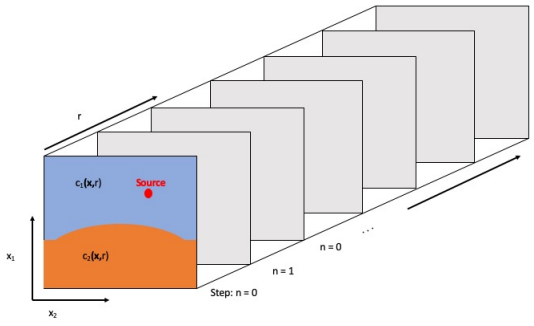

Figure 2-2: The parabolic equation "marches" in range, evolving the acoustic field in 2D slices. Adapted from [4].

The last aspect to discuss with regards to computing with the Parabolic Equation method is how to treat the pseudo-differential operator Q. Computing the square root of a differential operator is non trivial and further compounded by that in implementation, values are discrete in range and depth, thus the square root of a matrix is needed. To enable efficient computations one more approximation is commonly needed, further limiting this computational method. We revise (2.26), and consider its Taylor series expansion:

$$q = \epsilon + \mu \tag{2.31}$$

$$\epsilon = n^2 - 1 \tag{2.32}$$

$$\mu = \frac{1}{k_0^2}\frac{\partial^2}{\partial z^2} \tag{2.33}$$

$$Q = (1+q)^{\frac{1}{2}} = 1 + \frac{q}{2} - \frac{q^2}{8} + \frac{q^3}{16} + ... \tag{2.34}$$

Taking only the first two terms of (2.34) results an a narrow-angle equation, considered accurate for propagation within 10° to 15° off the horizontal [32].

$$Pu = ik_0(1 + q/2)u\,. \tag{2.35}$$

This derivation result, (2.35), is a first-order partial differential equation with respect to r, or "Parabolic" instead of "Elliptic" as in (2.24). Assuming the far-field approximation is valid, it accurately computes outgoing waves by range marching. The errors or limitation of this form is that it neglects any backscatter, makes small errors induced by neglecting (2.29), and is limited to narrow angles due to truncating the Taylor series approximation (2.34).

2.2.2 Ray Methods

Ray methods [32, 34] are used for many applications associated with wave propagation (e.g. Radar, Optics, etc). As stated earlier, they are one of the more popular methods in underwater acoustics. The "Ray" refers to a continuous path that is normal to the wave front. Rays are useful to explain wave propagation because most individuals have been introduced to concepts such as Snell's Law in physics or through the practice of shining a light into a tank of water and observe the results and special effects. By conceptualizing the

wavefront as being composed of an infinite number of rays at a given time, it is also often easier to understand how a wave might refract or reflect as is passes through a medium.

Ray Methods allow for the computation of travel time and the pressure field, but they begin with a process of representing the wavefront in a Lagrangian sense referred to as "Ray Tracing." For relations to level-set methods, we refer to section (2.2.3). Ray Tracing forms the skeleton of the acoustic field, and if computed accurately and efficiently, provides a model to where the sound energy will travel.

The derivation begins with 2.21 and assumes that the solution is of the form:

$$p(\mathbf{x}) = e^{i\omega\tau(\mathbf{x})} \sum_{j=1}^{\infty} \frac{A_j(\mathbf{x})}{(i\omega)^j} \,. \tag{2.36}$$

Taking the associated partial derivatives with respect to $\mathbf{x}$ and inserting them back into (2.21) results in the following sequence of equations:

$$\begin{aligned} &O(\omega^2) : |\nabla\tau|^2 = \frac{1}{c(\mathbf{x})^2} \\ &O(\omega) : 2\nabla\tau \cdot \nabla A_0 + (\nabla^2\tau(\mathbf{x}))A_0 = 0 \\ &O(\omega^{1-j}) : 2\nabla\tau \cdot \nabla A_j + (\nabla^2\tau(\mathbf{x}))A_j = -\nabla^2 A_{j-1}, j = 1, 2, \ldots \end{aligned} \tag{2.37}$$

Typically, this method only requires that the leading terms of (2.37) are used, which is know as the high frequency approximation. While there is no definitive answer to the minimum frequency allowed, it is generally accepted that the wavelength should be significantly smaller than features of the water column (e.g. bottom depth, sound ducts, bathymetric features, etc.) [32]. To obtain estimates of travel time, solving the first equation, also known as the eikonal equation, is required. Reviewing the characteristics of (2.36), we see that constant phase values for $\tau(\mathbf{x})$ correspond to the wave front. By converting the eikonal equation to ray coordinates, and knowing that $\nabla\tau$ is perpendicular to the wave front, the direction of the ray travel, at speed $c(\mathbf{x})$, over a length s can be defined as:

$$\frac{d\mathbf{x}}{ds} = c(\mathbf{x})\nabla\tau(\mathbf{x}) \,. \tag{2.38}$$

By squaring the absolute value of both sides of (2.38) and then substituting the eikonal

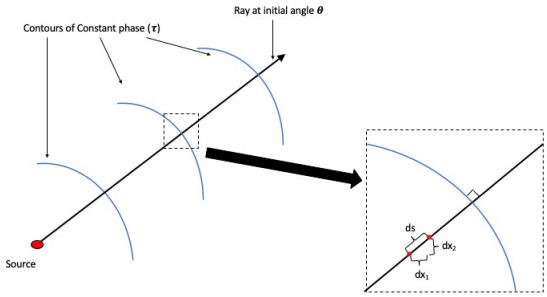

Figure 2-3: The ray leaving the source at a specified angle travels perpendicular to the wave front. Here, we see that infinitesimal changes in the Cartesian plane (x_1,x_2) corresponds to infinitesimal steps along the ray or arc-ength.

equation from (2.37):

$$|\frac{d\mathbf{x}}{ds}|^2 = c(\mathbf{x})^2|\nabla\tau(\mathbf{x})|^2 = \frac{c^2(\mathbf{x})}{c^2(\mathbf{x})} = 1 \tag{2.39}$$

Therefore $\frac{d\mathbf{x}}{ds}$ is of magnitude 1, where s is the arclength of the ray. Taking the derivative of (2.39) with respect to s and using the relationship (2.38), the ray trajectory is expressed as:

$$\frac{d}{ds}(\frac{1}{c(\mathbf{x})}\frac{d\mathbf{x}}{ds}) = -\frac{1}{c(\mathbf{x})^2}\nabla c(\mathbf{x}) \tag{2.40}$$

A practical way to express this second order ordinary differential equation (ODE) consists of using an auxiliary variable $\boldsymbol{\xi}$. This $\boldsymbol{\xi}$ can be interpreted as a vector that, when scaled by $c(\mathbf{x})$, is the tangent vector to the ray trajectory at each step s. The ray trajectories can then be expressed as a coupled set of first-order ODEs. For 2-D (Range = x_1, Depth=x_2) propagation problems, denoting

$$\mathbf{x}(s) = \begin{bmatrix} x_1 \\ x_2 \end{bmatrix}; \qquad \boldsymbol{\xi}(s) = \begin{bmatrix} \xi_1 \\ \xi_2 \end{bmatrix}, \tag{2.41}$$

the coupled set of ODEs are written as:

$$\frac{d\boldsymbol{\xi}(s)}{ds} = -\frac{1}{c(\mathbf{x})^2}\nabla c(\mathbf{x}) \tag{2.42}$$

$$\frac{d\mathbf{x}(s)}{ds} = c(\mathbf{x})\boldsymbol{\xi}(s)\,. \tag{2.43}$$

While these equations could be parameterized by time as easily as by distance along the ray s, given a ray path, it is a straightforward integral to determine the ray travel time in terms

of the ray arclength s (t_s):

$$t_s = \int_0^s \frac{1}{c(s')} ds' \tag{2.44}$$

In summary, to obtain travel times for a given wave front, by taking advantage of the eikonal equation and by representing the wavefront by "rays" that propagate normal to the wave front, we obtained two ODEs that can be easily numerically integrated. They provide the rays path from which one can obtain travel times by numerical integration along the ray paths. We note that in the derivation of the ray trajectories, the ω term is not present. This implies that this representation of the wavefronts is frequency independent, though it still must satisfy the high frequency approximation (i.e. the first term in the approximation does not contain ω).

There are nonetheless significant drawbacks to this method. First, the derivations required shifting into ray coordinates for which boundary conditions in Cartesian coordinates are not directly translated [e.g. 36]. Therefore, reflections must be evaluated when they occur and thus modeled outside of the solver for the ODE pairs. Second, in stratified seabed bottom, a portion of the ray will transmit into the bottom and reflect at another depth to return to the seawater medium. This would require additional rays to track and again require implementations outside solving the ODE pairs. Chapter 3 provides methods for reflection implementation in a stochastic setting but does not account for the transmitted ray.

Third, as seen in Figure 2-4, ray tracing can develop shadow zones that imply the wave transmit no or very small energy into this region. While acoustic energy transmission tends toward areas of low soundspeed, energy would still be transmitted into these zones (e.g. solving for the wavefront could reach these shadow zones). Still practically, if the signal reception is the goal, the shadow zones should be avoided.

Lastly, to determine ray travel time, the ray used for integration must pass from the source to the receiver. We refer to these specific rays as "eigenrays." Since the rays represent a wavefront with discretized points, there is no guarantee that rays will pass through the receiver with a certain tolerance and one may thus require additional processing to identify these eigenrays. Here are three methods that can be used to determine travel times at a specific receiver location:

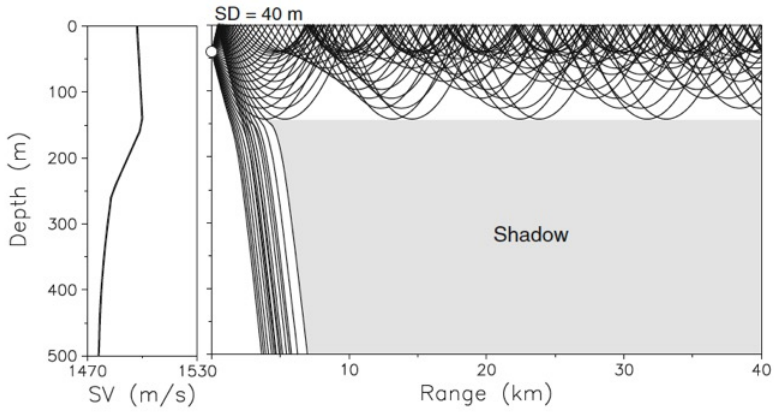

Figure 2-4: Example of a source at a depth of 40 m. Rays show Surface-duct propagation in the Norwegian Sea; however only valid for high frequencies. Adapted from [32]

- Discretize initial ray angles ($\delta\theta$) to minimize distance between rays, add more rays,
- Use a numerical scheme such as bisection to trace rays between θ's that bound the receiver, or
- Interpolate travel time based adjacent rays.

Of course, each of these add computational expense.

2.2.3 Level Sets

Level Sets is another method that is more popular in optics research, but that can also be used to model underwater acoustic propagation as the fundamentals are nearly the same. The Level Sets method is related to the ray tracing method in that both aim to tracking a wave front. While ray tracing represents the characteristics of the wave front one-by-one, the level set methods integrates the whole wave front in space and time. As ray tracing considers discrete points along the wave front that can spread as the wave is propagated in space and time, one issue is that the resolution in the wave front decays as the wave spreads, as shown in Figure 2-5. For this reason an Eulerian representation of the wave front, i.e. a level-set method, may be preferable. Instead of solving for discrete points on the wavefront, level-set methods solve the Hamilton-Jacobi PDE for the wavefront on a grid in space [68]. For relations of level-set methods to characteristics, Hamilton-Jacobi equations, and path planning, we refer to [60, 59, 50, 24, 36].

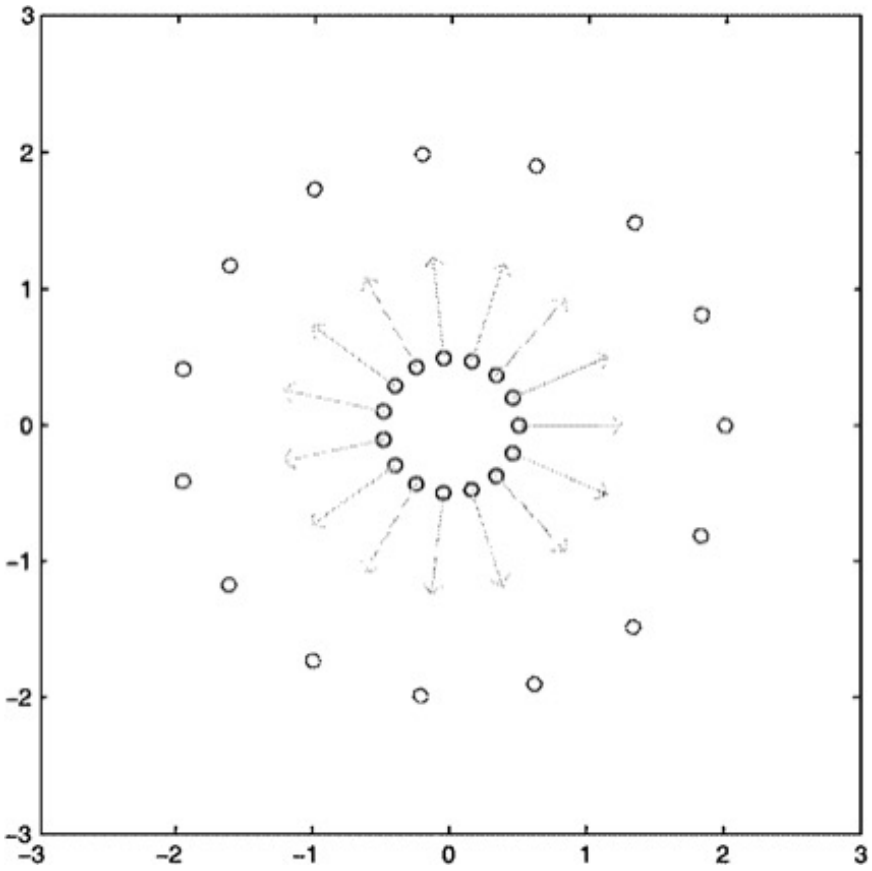

Figure 2-5: Initial set of points forming a circle spread apart during ray tracing. Adapted from [68]

Assuming (2.17) has a solution similar to (2.36), but remaining in the time domain,

$$p(\mathbf{x}, t) = e^{i\omega\tau(\mathbf{x},t)} \sum_{j=0}^{\infty} \frac{A_j(\mathbf{x}, t)}{(i\omega)^j}\,, \tag{2.45}$$

$\tau(\mathbf{x}, t)$ remains the phase function. Substituting (2.45) back into the wave equation, and making a similar high frequency approximation as for Ray Tracing, results in a Hamiltion-Jacobi type partial differential equation (PDE):

$$\tau(\mathbf{x}, t) + c(\mathbf{x})|\nabla\tau(\mathbf{x}, t) = 0 \tag{2.46}$$

For a 2-D system, to account for reflections, this method evolves the acoustic wavefront as a strip in a higher dimensional reduced phase space with coordinates (x_1, x_2, θ) where θ represents the normal direction at any given point along the wavefront [63, 12, 9]. The strip

is represented as the intersection of two level set functions:

$$\frac{\partial}{\partial t}\psi_1(x_1, x_2, \theta) + V(x_1, x_2, \theta) \cdot \psi_1 = 0\,, \tag{2.47}$$

$$\frac{\partial}{\partial t}\psi_2(x_1, x_2, \theta) + V(x_1, x_2, \theta)\psi_2 = 0\,. \tag{2.48}$$

The results are illustrated as the spatial representations of (2.47) and (2.48) in Figure 2-6. The velocity field (the sound-speed-profile, SSP), $V(x_1, x_2, \theta)$, of the strip's propagation is

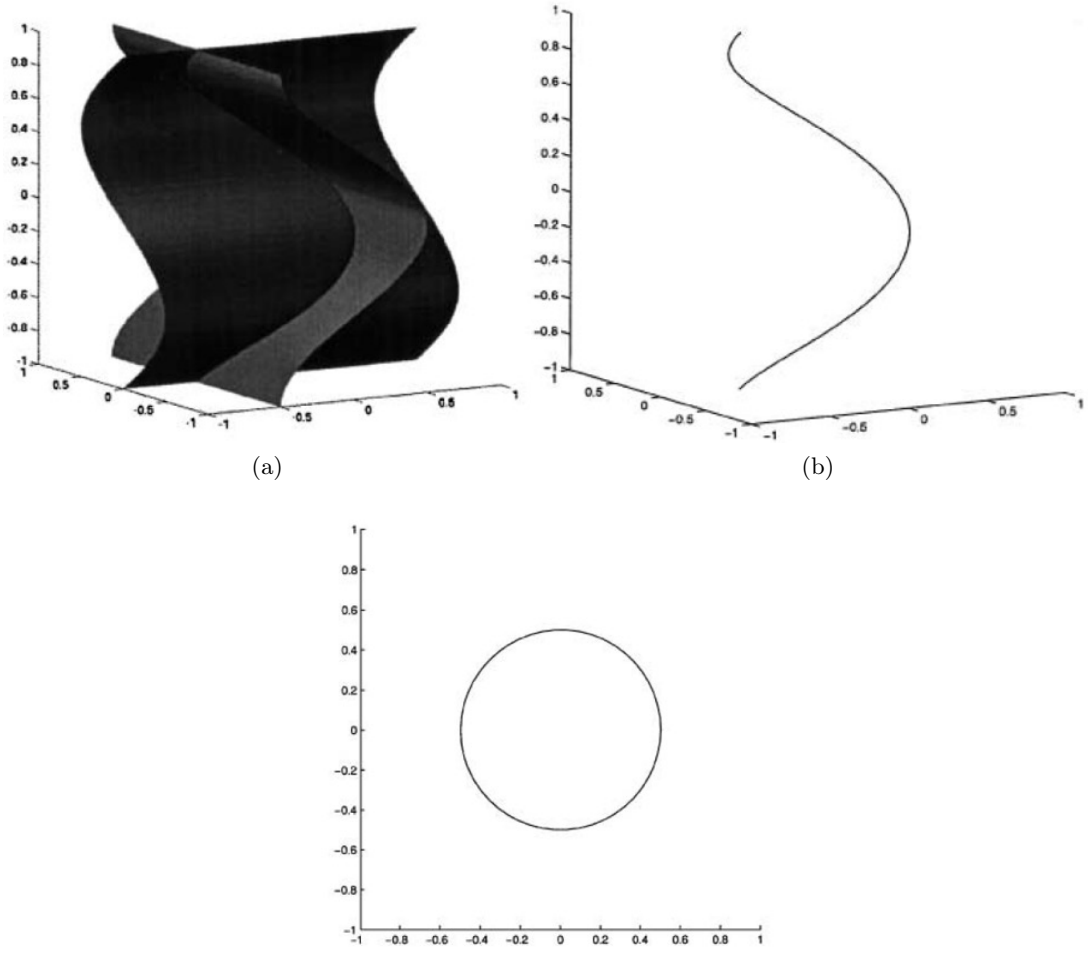

(a) (b)

(c)

Figure 2-6: The first picture shows the zero level set surfaces of two level set functions. The second picture shows the curve of intersection of those surfaces. The final picture shows the wavefront described by that curve. Adapted from [68].

derived from the Liouville equations:

$$V(x_1, x_2, \theta) = \begin{bmatrix} c(\mathbf{x}) \cos\theta \\ c(\mathbf{x}) \sin\theta \\ \frac{\partial c(\mathbf{x})}{\partial x_1} \sin\theta - \frac{\partial c(\mathbf{x})}{\partial x_2} \cos\theta \end{bmatrix}. \tag{2.49}$$

Finally, the wavefront, $W(\mathbf{x}, t))$, in 2-D is defined by:

$$W(\mathbf{x}, t)) = \{\mathbf{x} | \psi_1(x_1, x_2, \theta) = \psi_2(x_1, x_2, \theta) = 0\}. \tag{2.50}$$

Level Sets can be a useful method for computing acoustic travel times with the benefit of high resolution of the wavefront properties. They do not require the use of Fourier transforms and allow for direct application of physical boundary conditions in the same domain as the solver. However, there are several inefficiencies with the Level Sets method as well. The method still makes a high frequency approximation and, to be accurate, the propagation at each time-step should correspond to a distance less than the acoustic wavelength. Due to the need of representing multiple reflections, the method also requires solving a PDE definied in 2-D into a 3-D space by adding the θ parameter representing the direction of propagation. This for example allows tracking additional wave fronts when waves are transmitted to and from the bottom. The Eulerian approach can present difficulties with multi-valued wavefronts, which is likely to occur as waves will fold over on another due to reflections [98, 62]. Lastly it is not easily extended to incorporate the pressure field computation for which we still may require using ray methods [63].

2.3 Uncertainty Quantification Methods and Reduced Order Models (ROMs)

2.3.1 Monte-Carlo

Monte-Carlo Methods are the most popular and the simplest uncertainty quantification method to implement [41]. This is especially attractive when we take into account the complexities associated with acoustic modeling, even for a fixed specific ocean environment. Given the requisite amount of time and computational power, Monte-Carlo methods require nothing more than performing deterministic or stochastic sample path computations on the

sampled distribution of inputs (i.e. a "for" loop). If the underlying distribution is sufficiently sampled, we can obtain an accurate distribution of the stochastic process.

In the preceding paragraph, we included an important caveat that "the underlying distribution is sufficiently sampled." "Sufficiently sampled" implies that we have run our model on a sufficient number of randomly or well-chosen sampled inputs from a known distribution such that our resultant distribution of solutions converges to the real distribution. The convergence rate of the variance based on the number of samples M is on the order of $M^{-\frac{1}{2}}$. In application, it is frequent for the sample sizes required for convergence to be so large that they exceed the computing power of most computers; however there exists many techniques that can reduce the requisite sample size [33].

We discussed Mont-Carlo methods here not to elaborate on the efficiencies to be gained with alternate Monte-Carlo approaches, but instead to make two points:

- Given enough samples and an accurate deterministic model, we can converge on the actual distribution outputs. This is useful in evaluating the results of alternate methods.

- Monte-Carlo though simple and robust, may not be feasible in compact computation scenarios or in large nonlinear problems such as coupled ocean physics and acoustics forecasting.

2.3.2 Empirical Orthogonal Functions

Outside specific fields (climatological, meteorological, or oceanographic), Empirical Orthogonal Function (EOF) is nearly synonymous with the more frequently referred to Principle Component Analysis (PCA). Singular Value Decomposition (SVD) is the key in both of their applications [38]. Scientist studying the ocean and atmosphere have frequently used EOFs since their inception in mid-20^{th} century [39, 61, 65].

With a set of sampled data, EOFs are used to represent the data by performing a linear combination of eigenvectors or functions that provide a reduced-order approximation of the data set that is optimal in the sense of variance explained [61]. The reduced-order model (ROM) arises because it is desirable to use the minimum number of eigenvectors as possible [61]. Conceptually, consider snapshots of SSPs of a given area of the ocean as a stochastic field due to the uncertain nature of the ocean environment. We can then construct the mean

and variance of the field that links SSP information to all data points. Since the covariance matrix will be both real and symmetric, it can be decomposed into [66]:

- Orthogonal Eigenvectors: Statistically independent patterns within the field that are spatially orthogonal

- Positive eigenvalues that correspond to the variance that the eigenvector pattern accounts for

Ocean Acoustic Tomography offers an excellent example of how we may use EOFs as a ROM to compute sound propagation travel times. The aim of Munk et al. [65] is to resolve temperature and current field through sound propagation through matrix inversion, known as acoustic tomography. While we do not intend to explain tomography in detail, outlining the application of EOFs for acoustic inversion is a relevant example and illustrates some of this method short comings. The following explanation follows the derivation for the inversion of travel times in [14].

Since ocean currents and sound propagation speeds are on the order of 10^{-1} and 10^{3} respectively, we assume that current will have a negligible effect on travel times; therefore, given a ray path, we can compute the travel time from a source to the receiver using (2.45). Re-writing (2.45) as:

$$t_n = \int_{S_n} \frac{ds}{c(\mathbf{x})} \tag{2.51}$$

where S_n corresponds to the n^{th} ray path that leaves the acoustic source and arrives precisely at the receiver, for the given SSP field. Acousticians refer to these specific rays as eigenrays. Assume, based on prior knowledge that the best estimate is the mean SSP, $\overline{c}(\mathbf{x})$. We wish to compute the difference in travel time given an SSP field,

$$\delta t_n = t_n - \bar{t}_n = \int_{S_n} \frac{ds}{c(\mathbf{x})} - \int_{\overline{S}_n} \frac{ds}{\overline{c}(\mathbf{x})}\,. \tag{2.52}$$

In (2.52), $\overline{S}_n$ corresponds to the n^{th} ray path in the mean SSP environment. Making the assumption, or synonymous statements:

$$S_n \approx \overline{S}_n \tag{2.53}$$

or applying Fermat's principle [65], we can approximate (2.52) as:

$$\delta t_n \approx \int_{\overline{S}_n} \left(\frac{1}{c(\mathbf{x})} - \frac{1}{\overline{c}(\mathbf{x})} \right) ds \tag{2.54}$$

Because $\delta c(\mathbf{x})$ is $O(10^1)$ and $c(\mathbf{x})$ is $O(10^3)$, making one last assumption we can conclude that (2.52) is:

$$\int_{S_n} \frac{\overline{c}(\mathbf{x}) - c(\mathbf{x})}{\overline{c}(\mathbf{x}) c(\mathbf{x})} ds \approx \int_{S_n} \frac{\delta c(\mathbf{x})}{\overline{c}^2(\mathbf{x})} ds \,, \tag{2.55}$$

where $\delta c(\mathbf{x})$ expresses how much a given SSP, η, varies from the mean SSP. The remainder of this derivation implements the EOFs or PCA to create a ROM that allows for an input of SSPs and creates an output of corresponding perturbations in travel time. Let $\delta c(\mathbf{x})$ can be expressed as a linear combination of M orthogonal functions $f_m(\mathbf{x})$, then (2.55) becomes:

$$\delta t_n \approx \int_{S_n} \frac{\sum_{m=1}^{M} a_m f_m(\mathbf{x})}{\overline{c}^2(\mathbf{x})} ds = \sum_{m=1}^{M} a_m \int_{S_n} \frac{f_m(\mathbf{x})}{\overline{c}^2(\mathbf{x})} ds \,. \tag{2.56}$$

Consider a matrix C, where rows of C correspond to the depth (z) dependence of a range-independent, $\delta c(\mathbf{x})$, and the columns to the individual realizations of the ocean:

$$C = \underbrace{\left[\begin{array}{ccccc} \delta c_1(z_1) & \cdots & \cdots & \cdots & \delta c_H(z_1) \\ \vdots & \ddots & \vdots & & \vdots \\ \vdots & \cdots & \delta c_\eta(z_i) & \cdots & \vdots \\ \vdots & & \vdots & \ddots & \vdots \\ \delta c_1(z_D) & \cdots & \cdots & \cdots & \delta c_H(z_D) \end{array} \right]}_{\eta \epsilon [1, 2, \cdots, H]} \Bigg\} \text{depth}(z_i),\ i\epsilon[1, 2, \cdots, D] \,. \tag{2.57}$$

Let $\delta \mathbf{t}$ consist of N eigenrays passing from the source to the receiver in the mean SSP. By performing the SVD of $\mathbf{C} = \mathbf{U}\mathbf{\Sigma}\mathbf{V}^\mathbf{T}$, we achieve a reduction in the model by determining the number of eigenvectors of U, also known as the orthogonal eigenfunctions of $c_1(\mathbf{x}), \cdots, c_H(\mathbf{x})$, to include based on the relative sizes of the singular values in Σ. We assume M eigenvectors are selected, with $M << rank(C)$. Let $f_m(\mathbf{x})$ be the eigenvectors ($\mathbf{U}$) of $\mathbf{C}$ and $\mathbf{A} = \mathbf{\Sigma}\mathbf{V}^\mathbf{T}$ whose entries correspond to the coefficients a_m. We can now create the following matrix:

$$\mathbf{B} = \int_{S_n} \frac{f_m(\mathbf{x})}{\overline{c}^2(\mathbf{x})} ds; \text{for } n = 1 : N \tag{2.58}$$

$\mathbf{B}$ must be a NxM, and when multiplied by the columns of the MxH $\mathbf{A}$ matrix yields the approximate eigenray perturbations in travel time for each ocean realization:

$$\mathbf{T} = \mathbf{BA} \tag{2.59}$$

where:

$$\mathbf{T} = \begin{bmatrix} \vdots & & \vdots \\ \delta\mathbf{t}_1 & \cdots & \delta\mathbf{t}_H \\ \vdots & & \vdots \end{bmatrix} \tag{2.60}$$

The simplicity of (2.59) is very attractive for two clear reasons. First, given a measured set of perturbations in travel time from the travel time of the mean SSP, for the cost of computing the pseudo-inverse of $\mathbf{B}$ ($\mathbf{B^{-1}}$), we could compute the best fit coefficients a_m, reconstructing a best guess for the SSP. Second it appears as though we could create additional realizations for $\delta\mathbf{t}$ by selecting new coefficients for a_m. While this is a nice feature of this method, it is limited.

Though prevalent in ocean sciences, EOFs remain limited to certain applications. EOFs are highly dependent on the domain for which they are employed, it is difficult to know the number of realizations or samples needed for EOFs to accurately represent the SSP field, and in practice EOFs are based on sparse or non-synoptic sampled environments that will also have some measurement errors. Overall, all of the uncertainties can make it difficult to determine the significant from the insignificant eigenvectors [66, 56]. Upon reviewing the derivation to arrive at (2.61), it is relatively straightforward as to where these limitations are inserted when computing acoustic ray travel times.

2.3.3 Dynamically Orthogonal Equations

Dynamically Orthogonal Equations is a methodology to model and evolve the dominant uncertainty in a dynamical system [78, 79, 97, 25]. It consists of a stochastic expansion to represent the stochastic dynamical system: the mean, an orthogonal basis (modes), and their stochastic coefficients. Governing equations are derived for these three quantities from the knowledge of the original stochastic dynamical systems differential equations. Without loss of generality, a condition of dynamic orthogonality is imposed: the rate of change of the modes is orthogonal to the modes themselves.

We selected this methodology for implementations in Chapter 3 due to the following advantages [78, 25]:

- The modes evolve with the governing differential equations which enables fewer modes to represent the field of uncertainty.

- It is computationally efficient even when capturing non-Gaussian behavior.

- It is amenable to already developed non-Gaussian data-assimilation or Bayesian-inference algorithms [80, 81, 58, 57].

The summary of the DO decomposition and dynamically-adaptive reduced-order stochastic modeling that we provide below is adapted from ([70]) and the references cited therein. Consider that the evolution of a dynamical system state variable x, governed by the following PDE, commonly in space and time:

$$\frac{\partial x(r,t)}{\partial t} = \mathcal{L}(x(r,t))\,. \tag{2.61}$$

Now assume there is uncertainty in the above PDE and/or in its initial and boundary conditions. As a result, the solution of the now stochastic PDE is represented as a stochastic field $X(r,t;\eta)$ where the stochasticity is denoted by the random event variable η. We start with the DO decomposition of the stochastic field:

$$X(r,t;\eta) = \overline{x}(r,t) + \sum_{i=1}^{M} \tilde{x}_i(r,t)\phi_i(t;\eta)\,, \tag{2.62}$$

where $\overline{x}(r,t)$ represents the mean field, $\tilde{x}(r,t)$ are the eigenvectors or basis functions who's linear combinations with coefficients $\phi(t;\eta)$ represent the random components of the field. From this point on, we will refer to $\tilde{x}(r,t)$ and $\phi(t;\eta)$ as DO modes and DO coefficients, respectively. It may be convenient to interpret r as a spatial variable and t as a time, as indicated above. However, t could be interpreted as a range or any other parameter by which the field will "march".

In (2.62), all quantities are time dependent. Since the evolution in t for both the DO modes and coefficients creates redundancy, we can impose the condition that the stochastic

subspace can only evolve in orthogonally to itself, without any loss of generality:

$$\Big\langle \frac{\partial \tilde{x}_i(r,t)}{\partial t}, \frac{\partial \tilde{x}_j(r,t)}{\partial t} \Big\rangle = 0\,. \tag{2.63}$$

We now shift to Einstein notation where summations are implied. Inserting the DO decomposition (2.62) into the governing stochastic PDE, we obtain:

$$\frac{\partial \overline{x}(r,t)}{\partial t} + \frac{d\phi_i(t;\eta)}{dt}\tilde{x}_i(r,t) + \phi_i(t;\eta)\frac{\partial \tilde{x}_i(r,t)}{\partial t} = \mathcal{L}[X(r,t;\eta);\eta]\,. \tag{2.64}$$

This PDE (2.64) is the starting point for the derivation of how the mean, DO Modes, and DO coefficients will evolve with time. In this PDE, we can see that the stochastic DO coefficients render the governing right-hand-side $\mathcal{L}$ stochastic.

To derive the evolution of the mean field, we can simply take the expectation ($\mathbb{E}$) of (2.64) to obtain:

$$\frac{\partial \overline{x}(r,t)}{\partial t} = \mathbb{E}^{\eta}[\mathcal{L}[X(r,t;\eta);\eta]] \tag{2.65}$$

To derive the evolution of the DO coefficients, we start by taking the dot product of (2.64) with the DO modes $\tilde{x}_j(r,t)$:

$$\begin{aligned} \Big\langle \frac{\partial \overline{x}(r,t)}{\partial t}, \tilde{x}_j(r,t) \Big\rangle + \frac{d\phi_i(t;\eta)}{dt}\Big\langle \tilde{x}_i(r,t), \tilde{x}_j(r,t) \Big\rangle + \\ \phi_i(t;\eta)\Big\langle \frac{\partial \tilde{x}_i(r,t)}{\partial t}, \tilde{x}_j(r,t) \Big\rangle = \Big\langle \mathcal{L}[X(r,t;\eta);\eta], \tilde{x}_j(r,t) \Big\rangle \end{aligned} \tag{2.66}$$

Due to (2.63), we know at all t, $\Big\langle \tilde{x}_i(r,t), \tilde{x}_j(r,t) \Big\rangle = 1$ for all $i = j$ and 0 otherwise. Hence, we have:

$$\Big\langle \frac{\partial \overline{x}(r,t)}{\partial t}, \tilde{x}_j(r,t) \Big\rangle + \frac{d\phi_i(t;\eta)}{dt} = \Big\langle \mathcal{L}[X(r,t;\eta);\eta], \tilde{x}_j(r,t) \Big\rangle\,. \tag{2.67}$$

By also taking the dot product of (2.65) with the DO modes $\tilde{x}_j(r,t)$, we can use:

$$\Big\langle \frac{\partial \overline{x}(r,t)}{\partial t}, \tilde{x}_j(r,t) \Big\rangle = \mathbb{E}^{\eta}\Big[\Big\langle \mathcal{L}[X(r,t;\eta);\eta], \tilde{x}_j(r,t) \Big\rangle\Big]\,. \tag{2.68}$$

Hence, we obtain:

$$\frac{d\phi_i(t;\eta)}{dt} = \Big\langle \mathcal{L}(X(r,t;\eta)\eta), \tilde{x}_j(r,t) - \mathbb{E}^{\eta}\Big[\Big\langle \mathcal{L}[X(r,t;\eta);\eta], \tilde{x}_j(r,t) \Big\rangle\Big] \Big\rangle\,. \tag{2.69}$$

To derive the evolution of the DO modes, we begin by multiplying (2.64) by the DO coefficients and taking the average over η. Then we use the fact that $\mathbb{E}^\eta[\phi_j(t;\eta)] = 0$ to obtain:

$$\begin{aligned}\mathbb{E}^\eta\Big[\frac{d\phi_i(t;\eta)}{dt}\phi_j(t;\eta)\Big]\tilde{x}_i(r,t) + \mathbb{E}^\eta[\phi_i(t;\eta)\phi_j(t;\eta)]\frac{\partial\tilde{x}(r,t)}{\partial t} = \\ \mathbb{E}^\eta\Big[\mathcal{L}[X(r,t;\eta);\eta]\phi_j(t;\eta)\Big]\,.\end{aligned} \tag{2.70}$$

We can do the same to (2.69) to obtain:

$$\mathbb{E}^\eta\Big[\frac{d\phi_i(t;\eta)}{dt}\phi_j(t;\eta)\Big] = \mathbb{E}^\eta\Big[\Big\langle\mathcal{L}[X(r,t;\eta);\eta],\tilde{x}_j(r,t)\Big\rangle\phi_j(t;\eta)\Big]\,. \tag{2.71}$$

By inserting (2.71) into (2.70), and defining,

$$C_{\phi_i\phi_j} = \mathbb{E}^\eta[\phi_i(t;\eta)\phi_j(t;\eta)]\,, \tag{2.72}$$

the PDE governing the evolution of the DO modes is:

$$\begin{aligned}\frac{\partial\tilde{x}_i(r,t)}{\partial t} = \Big[\mathbb{E}^\eta\Big[\mathcal{L}[X(r,t;\eta);\eta]\phi_j(t;\eta)\Big] - \\ \mathbb{E}^\eta\Big[\Big\langle\mathcal{L}[X(r,t;\eta);\eta],\tilde{x}_j(r,t)\Big\rangle\phi_j(t;\eta)\Big]\tilde{x}_i(r,t)\Big]C^{-1}_{\phi_i\phi_j}\,.\end{aligned} \tag{2.73}$$

With the above governing DO differential equations, instead of solving a deterministic or stochastic PDE for every stochastic realizations, we can take advantage of the dynamic reduced order DO representation of the stochastic field as a mean plus a linear combination of the DO modes multiplied by stochastic DO coefficients. Using equations (2.65), (2.69), and (2.73), we can evaluate how each marches in time. Furthermore, depending on the type of differential equation given as $\mathcal{L}[X(r,t;\eta);\eta]$, there may be opportunity in further computational savings as complicated non-linear PDEs may be reduced to solving ODEs [70]. There are several examples where DO is successfully implemented including advection and Lagrangian transport [24], for fluid and ocean flows [97, 88], optimal path planning [85, 87], and recently in ocean acoustics through the parabolic equation [5, 3, 2].

2.4 Applications of Stochastic Ocean Acoustic Computation

When considering the applications of stochastic acoustic computation, there are two paradigms that we will review. In both, the ultimate Bayesian goal would be to accurately predict the

probability of the model state variables and/or parameters, given the uncertainties in the inputs (probabilities of the initial, boundary or model formulation conditions) and the in observations (sparse measurement errors, errors of representativeness). However, in many cases, it is only the mean or single most probable state field or parameter values that are estimated. One aim of the present thesis is to provide prior probabilities for acoustic ray predictions such that we can go beyond such single estimate focus and instead aim for Bayesian data assimilation and posterior probabilities. Nonetheless, we first start by reviewing a common application that considers a set of given measurements and aims to estimate the single model state variables or parameters that minimize the error between the actual measured and the model predicted value, a problem known as Matched-Field Processing. We then review existing results in coupled stochastic ocean physics and acoustic predictions and data assimilation. The second application illsuttrates this Bayesian approach and showcase the estimation of the posterior probability of state (bathymetry and sound speed fields), given the prior joint probability, likelihood, and sparse measurements.

2.4.1 Matched-Field Processing for source Localization and Acoustic Tomography

Match-Field Processing (MFP) as a concept has been utilized for a long time [10] with first experiments conducted in the mid 19^{th} century [69]. Since then, various communities have developed new algorithms and methods, with extensive applications to ocean acoustics and array processing [8, 71, 92].

MFP is a parameter estimation technique for localizing a source in the ocean environment. It incorporates acoustic modeling with signal processing [7]. If we assume that we sufficiently understand and model the physics of how sound will propagate, we can compute multiple realizations of the environmental state, parameters, and source locations [94, 8]. Upon taking a measurement of the environment, and leveraging signal processing to account for noise, we should be able to select an environment and source location combination that matches the measured value (within a set tolerance). Similarly, if we were to collect temporally and spatially varied measurements and then compute fields corresponding to the measurements, the fields are likely to focus on a specific source location or environment [95, 93, 71]. Matched-field processing has proven to be very useful in seismic, radar, and underwater acoustics applications [74].

2.4.2 Coupled stochastic ocean physics-acoustics uncertainty quantification and data assimilation

In the past decades, physical oceanography and ocean acoustics modeling research have become more and more interdisciplinary, for both fundamental dynamics and marine applications [76, 21, 19, 22]. The MIT-MSEAS ensemble uncertainty prediction modeling system has been utilized extensively for realistic stochastic coupled ocean-acoustics predictions. Dynamical effects of the ocean environment on underwater sound propagation were forecast in real time in several ocean regions, e.g., Dabob Bay [102], Mediterranean Sea [40], Middle Atlantic Bight [13], and Mediterranean sea [99, 100]. In [53], the complex tidal-to-large-scale dynamics of the northeastern Taiwan ocean region with strong internal tides and their effects of Nx2-D sound propagation were studied and successfully compared to oceanographic and acoustic transmission loss data. The results showed that with a realistic ensemble forecasting and data assimilation scheme (Error Subspace Statistical Estimation, [e.g. 52, 42]), the coupled ocean-acoustic modeling had predictive skill for both the ocean physics and acoustic fields and their uncertainties.

Researchers proposed and implemented Polynomial Chaos Expansions as a means to provide a method of incorporating environmental uncertainty into the computation of acoustic wave propagation. By expressing the variability with a spectral representation of a stochastic process, the wavefields become an expansion of orthogonal random polynomials [15]. Similar to the methods instituted in this thesis, this methodology assumes that the uncertainty inherent in SSP distribution propagates along with the acoustic wave field. Polynomial chaos expansions coupled with acoustic computation (e.g. Parabolic Equations), where uncertainty in the field is in terms of its statistical moments, has been effectively implemented [27, 26].

Interdisciplinary physical-acoustical data assimilation, which combines observations with fundamental dynamical models for field and parameter estimation has also become a powerful methodology [45, 49, 76, 20, 6]. For naval applications, end-to-end systems that couple meteorology-physical oceanography-geoacoustics-ocean acoustics-bottom-noise-target-sonar data and models, and that account and model the dominant uncertainties and their transfers across the end-to-end system are most urgently needed [76]. This transfer of uncertainty within the context of acoustic tracing is the subject of the present thesis. Once such non-

Gaussian uncertainty quantification is for acoustic ray tracing is available, we would be able to complete Bayesian data assimilation [31, 44, 50] for the joint inversion of acoustic rays and ocean fields. We note that the goal of Bayesian estimation is to estimate the posterior probability of the state we estimate, best combining prior model predictions with observations. For example, even though more observed information is provided, the actual uncertainty (e.g. the variance) may increase in the Bayesian update. New approaches to such acoustic Bayesian data assimilation are discussed next, within the context ocean floor mapping and acoustic parabolic equations [5].

2.4.3 Bayesian Inference for Ocean Floor Mapping

Let P(A) be the probability of a specific model for the ocean sound speed environment, Let B be a specific measurement of an acoustic signal. We can apply Bayes' Theorem to update our belief that our acoustic model accurately represents the real ocean acoustic environment:

$$P(A|B) = \frac{P(B|A) * P(A)}{P(B)} \,. \tag{2.74}$$

Bayes rule is for example a powerful tool when selecting a model out of a distribution of models. Not only can we identify the model with the best probability of being correct, but we also have a measure of certainty in the selected model.

Mapping the ocean floor is a daunting task that has received a lot of attention in the past decades [101]. Methods include using high resolution sonar systems, optics, or even satellite imagery. These are accurate, but also come with a high price tag, especially if used to map large portions of the ocean floor at high resolution. MIT Lincoln Laboratory is proposing the use of a sparse-aperture-mapping-technique consisting of autonomous surface vehicles that may leverage a Bayesian approach to identify bathymetric features [5].

Summarizing the approach, the system would compute transmission loss (TL) models and corresponding probability distributions for the given uncertain variable ocean bottom and its probability, accounting for the dominant uncertainties in the ocean sound-speed field and its own probability distribution. Then after measuring the transmission loss field, the Bayesian method first predicts the prior probability of the TL fields for the given probabilities in the ocean, seabed, and bathymetry inputs. It then performs a Bayesian (non-Gaussian) update to the joint probability density function, thereby providing a posterior

joint probability and allowing to improve the knowledge of the ocean bottom features in the Bayesian information sense. Efficient computation of the TL distribution requires accurate deterministic and stochastic computing techniques. The method employed extends the detaerministic Parabolic Equation acoustic computation to DO stochastic computation. For a more detailed description approach and results so far, We direct the reader to [5, 3, 2] and references therein.

Chapter 3

Dynamically Orthogonal Equations for Stochastic Acoustic Rays (DO-Ray): Methodology

3.1 Methods Overview

As discussed in the Thesis Overview, we combine Ray Tracing with Dynamically Orthogonal Equations as a method for stochastic acoustic computation. We start by explaining the intuition provided by Figure 3-1.

For the reduced order DO representation (in Einstein notation) of the stochastic ocean physics fields, $\mathbf{X}$ and $\boldsymbol{\Xi}$, we proceed as follows. We characterize each individual ocean realization, essentially a sound speed profile field realization, as the sum of the mean of the ocean fields with a linear combination of the number of modes determined necessary to capture the variability in the fields multiplied by their respective stochastic coefficients [86, 5].

Due to the stochastic sound-speed field, the underwater sound propagation field will also a stochastic field. In our case, we can decompose the acoustic rays state variables again using a DO decomposition, specifically:

$$\mathbf{x}(s;\eta) = \overline{\mathbf{x}}(s) + \tilde{\mathbf{x}}_i(s)\beta_i(s;\eta) \tag{3.1}$$

$$\boldsymbol{\xi}(s;\eta) = \overline{\boldsymbol{\xi}}(s) + \tilde{\boldsymbol{\xi}}_i(s)\gamma_i(s;\eta) \tag{3.2}$$

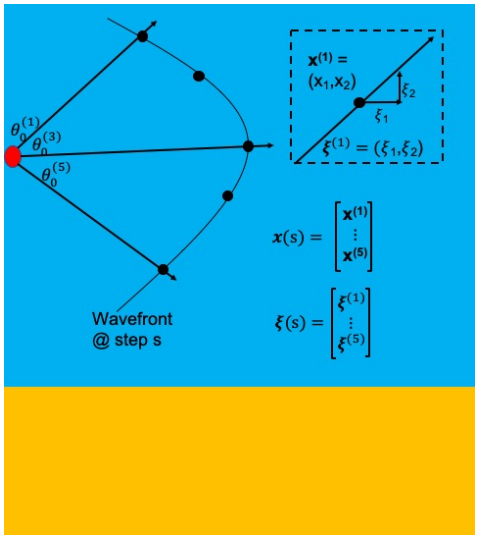

(a) Single Ocean Wavefront Realization at step"s."

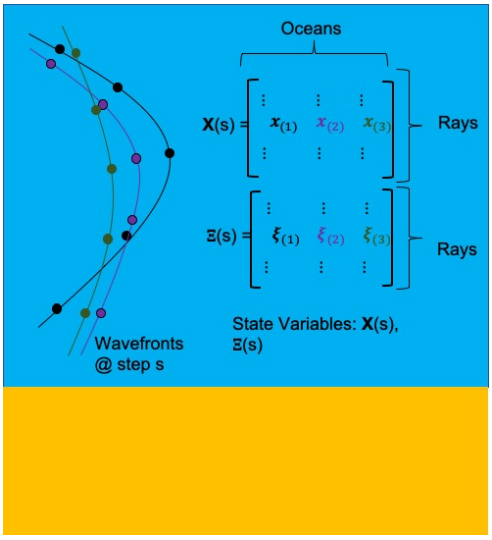

(b) Multiple Ocean Wavefront Realizations at step"s."

Figure 3-1: (a) Depiction of how for a single ocean, the wavefront at a given step along all of the rays "s" can be represented by 2 vectors, each of length $2 \times (\#rays)$. (b) Depiction at the same step along the rays "s," for multiple ocean realizations, $\mathbf{X}$ and $\mathbf{\Xi}$ represent a field of wavefronts for which we can obtain a reduced order representation.

The subscript "i" pertain to the DO modes and "η" pertains to a particular ocean realization event, and the summation over all "i" is implied.

For an alternate way of thinking about all of the $\mathbf{x}_{(i)}$ and $\boldsymbol{\xi}_{(i)}$, consider that for a given number of steps along the rays "s," they jointly describe the acoustic environment of an ocean (i). The ray tracing is not only a discrete representation of the wavefront; as a Lagrangian approach, it also gives a skeleton structure for how acoustic wave energy will propagate in a particular ocean realization (i).

As discussed in Chapter 2, the most straight forward and simplest method to obtain wavefront realizations is through a Monte Carlo implementation, hence solving for each ocean realization in series or parallel. A DO-Ray methodology allows for computing these realizations using a reduced representation of the stochastic field by solving governing ODEs for the stochastic mean $(\overline{\mathbf{x}}(s), \overline{\boldsymbol{\xi}}(s))$, DO modes $(\tilde{\mathbf{x}}_i(s), \tilde{\xi}_i(s))$, and DO coefficients $(\beta_i(s;\eta), \gamma_i(s;\eta))$.

In what follows in Chapter 3, we first describe how we implement and validate a deterministic ray methodology for two purposes:

- To provide a distribution of ray traces to analyze for the feasibility of a DO implementation and reduction, and

- To allow for realization-to-realization comparisons between the deterministic rays computed in Monte-Carlo fashion, and the stochastic realizations computed with the new DO-Ray methodology.

We follow with a principled qualitative and quantitative assessment of the error in our deterministic implementation.

We then evaluate the feasibility of a reduced-order representation for the acoustic field for both ray position and orientation. This analysis confirms the feasibility of a DO-Ray reduced representation, and provides insight for its implementation. We then derive the DO equations for ray tracing, tying together the methods described in Chapter 2.2.2 and 2.3.3. We also study some of the new computational intricacies that we introduce with a DO-Ray implementation. We examine the opportunities for further reduction in our representation, as well as some of the inherent challenges of the implementation. Lastly we analyze the computational cost of our DO-Ray implementation.

3.2 Deterministic Ray Tracing Implementation

3.2.1 Direct Integration

As derived in Chapter 2.2.2, the governing equations for acoustic ray tracing are:

$$\frac{d\boldsymbol{\xi}(s)}{ds} = -\frac{1}{c(\mathbf{x})^2}\nabla c(\mathbf{x}) \tag{3.3}$$

$$\frac{d\mathbf{x}(s)}{ds} = c(\mathbf{x})\boldsymbol{\xi}(s)\,. \tag{3.4}$$

Equations (3.3) and (3.4) are a coupled system of first-order, linear ODEs and are amenable to simple computational solvers. We are solving in a domain defined along a ray "s." At first glance, equations (3.3) and (3.4) appear to have a second independent variable $\mathbf{x}$; however, $\mathbf{x}$ is here merely the specific position of the modeled ray in the $range(x_1)$ vs $depth(x_2)$ plane. In [32], they refer to the methods we use to solve this system of equations as Direct Integration. We solve the equations sequentially in explicit fashion, but still require initial conditions.

The initial condition for $\mathbf{x}$ is self-evident as we consider a ray starting at $\mathbf{x}_0 = \langle x_1 = 0, x_2 = depth \rangle$ given an initial launch angle θ_0, in an acoustic medium described by $c(\mathbf{x})$, taking a step of length ds. Since the direction a ray travels as it marches along its arc length

is $\frac{d\mathbf{x}}{ds}$, we can rearrange equation (3.4) to establish the following initial conditions for an individual ray's components $\mathbf{x}$ and $\boldsymbol{\xi}$:

$$\boldsymbol{\xi}_0 = \begin{bmatrix} \frac{\cos\theta_0}{c(\mathbf{x}_0)} \\ \frac{\sin\theta_0}{c(\mathbf{x}_0)} \end{bmatrix} \;\; ; \;\; \mathbf{x}_0 = \begin{bmatrix} 0 \\ \text{Source Depth} \end{bmatrix} . \tag{3.5}$$

We can now implement an explicit numerical scheme to solve for the next step along the ray. Using a Forward-Difference scheme, or Euler's Method, we can an iterative algorithm to solve for ray position in the water column:

$$\mathbf{x}_{n+1} = c(\mathbf{x}_n)\boldsymbol{\xi}_n \Delta s + \mathbf{x}_n \tag{3.6}$$

$$\boldsymbol{\xi}_{n+1} = -\frac{1}{c(\mathbf{x}_n)^2}\nabla c(\mathbf{x}_n)\Delta s + \boldsymbol{\xi}_n \; . \tag{3.7}$$

Starting at the source with our initial launch angle, the ray takes a step (length = Δs) in this direction to update it's position. Simultaneously, we determine the effect of the sound speed gradient over the same Δs on the ray direction and update the ray direction at it's new position. We acknowledge that there are more accurate schemes than Euler's method though they will incur a great computational cost. Later, we evaluate the error associated with this simple first-order scheme as well as a higher-order scheme for comparison.

SSPs are often obtained by direct measurement and presented in a tabular format, where ample care is applied while interpolating between measurements [32]. We choose to represent the depth dependent sound speed as a table where the rows correspond to the discretized depths. We then apply a Shapiro filter [51, 54] to smooth the profile and discretize the SSP to 1 m depth increments. When computing the sound speed at a specific depth, we can apply piece-wise linear interpolation as opposed to a nearest neighbor approach.

3.2.2 Boundary Conditions

Hard Implementation

Because we have a system of first-order, linear ODEs, mathematically, we only require an initial condition to solve the system: it allows us to march along the ray for as long as $c(\mathbf{x})$ is defined. To account for reflections off the surface or seabed, we must alter the algorithm. The following method is described in more detail in [32].

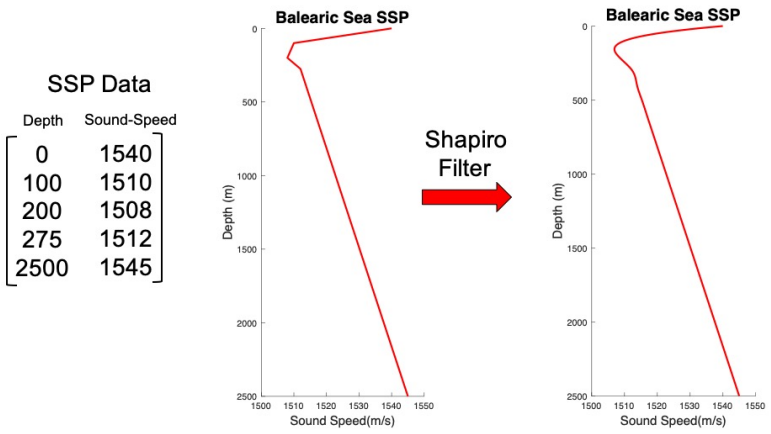

Figure 3-2: This example SSP is adapted from [32]. With only five (depth,sound-speed) points, we are able to smooth the profile using a Shapiro filter.

Consider a ray that interfaces with the bottom as in Figure 3-3. The tangent vector of

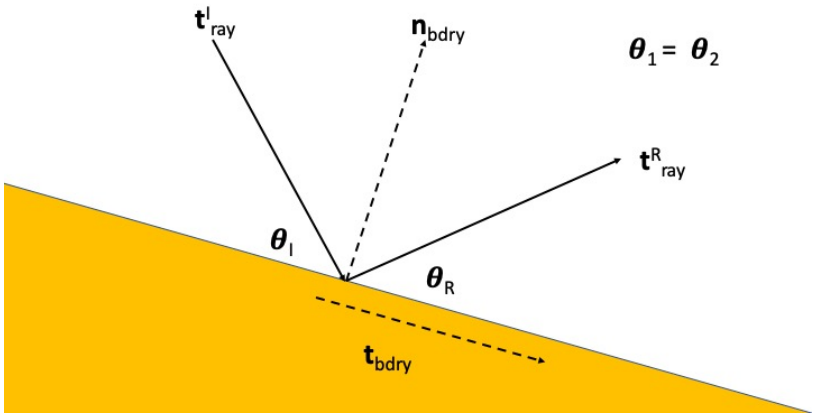

Figure 3-3: Ray reflection off piece-wise linear boundary adapted from [32]. For a reflection, the normal component of the ray changes sign, while the parallel component remaining the same. Of note, on a horizontal surface, we can insert a reflection by reversing the sign of the depth component of $\boldsymbol{\xi}_n$.

the ray at this point is:

$$\mathbf{t}^I_{ray} = \frac{d\mathbf{x}(s)}{ds} = c(\mathbf{x})\boldsymbol{\xi}(s)\,. \tag{3.8}$$

Assume we can also represent the ocean bottom as piece-wise linear for which we can compute the normal vector, $\mathbf{n}_{bdry}$, and tangent vector, $\mathbf{t}_{bdry}$. Therefor we can represent the incident ray's tangent vector as:

$$\mathbf{t}^I_{ray} = \alpha\mathbf{n}_{bdry} + \beta\mathbf{t}_{bdry}\,, \tag{3.9}$$

where:

$$\alpha = \mathbf{t}^I_{ray} \cdot \mathbf{n}_{bdry} \tag{3.10}$$

$$\beta = \mathbf{t}^I_{ray} \cdot \mathbf{t}_{bdry} \ . \tag{3.11}$$

We can now represent a reflected ray as:

$$\mathbf{t}^R_{ray} = -\alpha \mathbf{n}_{bdry} + \beta \mathbf{t}_{bdry} \ . \tag{3.12}$$

We refer to this as a hard implementation. It will require an evaluation of bottom interfaces and altering of the ray path external to the ODE solver.

Reflecting SSPs for Stochastic Rays on flat boundaries

Evaluating bottom interfaces and subsequent alteration of the ray path can be computationally expensive. It presents additional challenges in stochastic implementation. Since the ray reflections are not governed as boundary conditions for the coupled ODE system, we consider a method to account for reflections in post processing. Consider a ray that

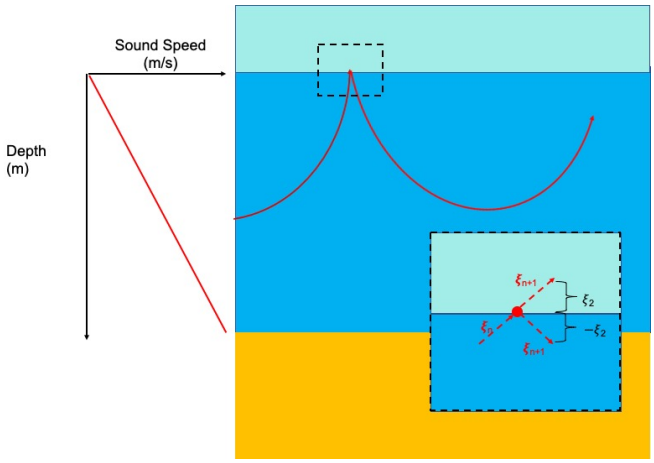

Figure 3-4: Ray reflection off a flat sea surface. We insert the reflection by negating the depth component of $\boldsymbol{\xi}_n$.

interfaces with the ocean surface assumed to be flat. As shown in Figure 3-3, the switch in the ray trajectory only requires switching the sign of the depth component of $\boldsymbol{\xi}$ (ξ_2). The result is illustrated in Figure 3-4.

Now, rather than evaluating for rays at or near the boundary, instead we allow the

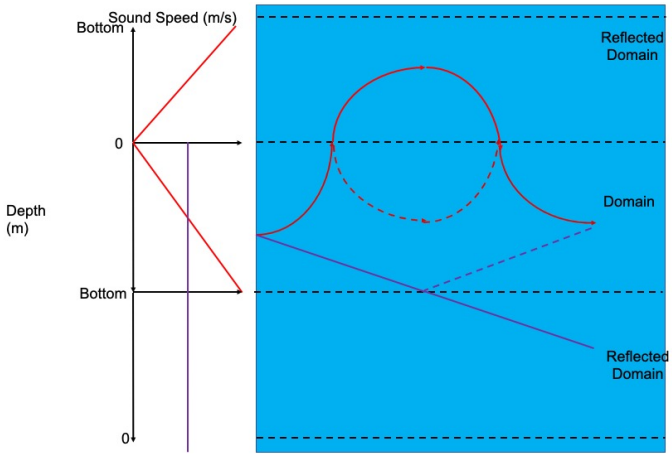

Figure 3-5: Two example oceans with a single ray in each ocean. The red corresponds to a constant positive gradient SSP. The purple corresponds to an isovelocity profile. By reflecting the domain, we no longer have to impose boundaries as we march along the ray. The ray will propagate into a reflected medium were the effect of sound speed is reversed. The ray is simply reflected back into the real domain (dashed) after it is computed.

algorithm to propagate the wave into a reflected ocean where it now behaves as a mirror image to the actual propagation. Once the ray trajectory is computed, we can reflect the images back into the real physical domain as illustrated in Figure 3-5.

This method is limited in that it requires a flat boundary, e.g. a flat bottom or flat sea surface. However it will prove useful because it is computationally efficient in stochastic implementations where hard implementations can hamper numerical efficiency.

3.3 Validation of Deterministic Ray Tracing Implementation - Error Analysis

In order to analyze the error of our deterministic ray discretization and implementation, ideally we would like to compare our results with an analytical expression for how the ray will travel; however this does not exist for realistic ocean fields. Still, with the knowledge that sound will bend toward the regions of lower sound speed and that how it bends is dependent on the gradient of the sound speed profile, we can write the equation for the ray

in a geometrical form [35]:

$$\sigma = -\frac{1}{g}\frac{c(\mathbf{x}_0)}{\cos\theta_0}$$
$$g = \frac{dc(\mathbf{x})}{dx_2} \tag{3.13}$$

where σ is the radius of curvature. For a constant-gradient, "g", given the starting point with initial angle of a particular ray, we can solve for its path analytically. We thus have an analytical solution for a ray. Using different sound speed gradients, we can analyze how well our finite difference implementation compares to the solution characterized as a circle of radius σ. By computing results for varying step-size, we can also observe expected convergence rates

First we implement and analyze both a forward Euler scheme with expected first-order error and a Runge-Kutta scheme with expected second-order error against the analytical solution for an idealized constant gradient ocean. Due to the constant gradient, we also have an analytical solution to compute sound-speed as a function of depth. As a result, we observe the characteristic errors and convergences of both first-order forward Euler and second-order Runge-Kutta implementations.

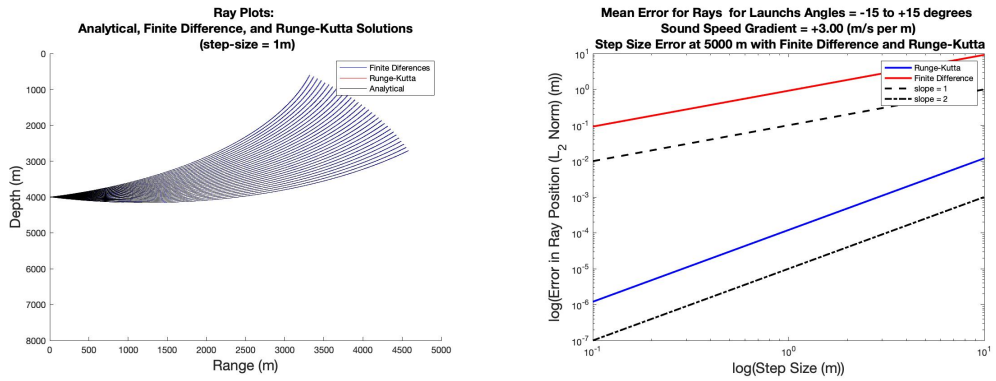

(a) Ray plots

(b) Convergence Plots.

Figure 3-6: This test case is is an idealized ocean scenario. The sound speed profile has a constant gradient of 3 m/s per m resulting in unrealistic sound-speeds closer to the surface and the bottom. a) Ray paths evenly spaced between 15° above and below the horizontal and computed using a step-size of 1 m. At this scale, the difference in the ray paths are indistinguishable. (b) We observe the expected convergence rate as step size decreases confirming the first-order convergence of forward Euler and second-order convergence of Runge-Kutta.

Figure 3-6(a) shows that the rays appear indiscernible when observing the rays in their

entirety hence the general paths are retained by both implementations as compared to the analytical solutions. Figure 3-6(b) both confrims our expected order of convergence, and shows that if an analytical solutions were not available, the extent to which we can approximate the analytical solution given a step size. Since we confirmed the expected convergence for the Runge-Kutta, we see that by selecting a step size two orders of magnitude smaller than our implementation ($\Delta s = 10^{-3}$ m vs $\Delta s = 1$ m), the relative difference between the analytical solution and the higher resolution is negligible. Therefore, we will use the Runge-Kutta deterministic solver with the stepsize of $\Delta s = 10^{-3}$ m as our reference to compute future assessment of the error.

We now insert additional computational error to the model by computing sound-speed by piece-wise linear interpolation. We discretize the sound speed profile between the 1 m increments use a function that computes sound speed by conducting piece-wise linear interpolation between depths.

Again, we observe the expected convergence for both the Runge-Kutta and forward Euler implementations. Based on the results displayed in Figure 3-7, for a constant positive gradient, we can assume that a step size less than 1 m for both implementations should be acceptable. We have also validated that our method of computing the sound-speed and sound-speed gradients do not introduce any appreciable error. We now can observe how the implementations perform when there is no analytical solution by again comparing both schemes of a similar step size (1 m) to that of a Runge-Kutta scheme using a step-size several orders of magnitude smaller (10^{-3} m).

As a test case, we choose the SSP respresentation of the Balearic Sea listed in [32] where a negative over a positive sound speed gradient results in rays ducting in the regions of minimal sound speed (see Figure 3-2).

Due to the increased complexity of the Balearic Sea SSP, we observe that the error associated with each implementation converges as expected with step size, with some small oscillations. Based on these results, and previous implementations, we are confident that this methodology produces reliable ray traces within an acceptable tolerance using first-order forward Euler (avg. error < 0.25 m with $\Delta s = 1$) or second-order Runge-Kutta (avg. error $< 5 * 10^{-3}$ m with $\Delta s = 1$).

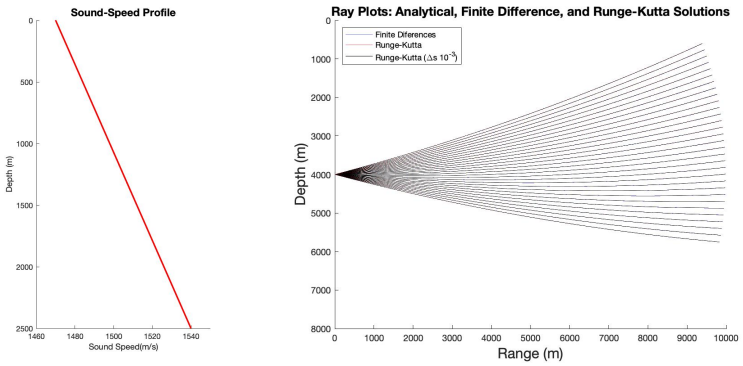

(a) SSP (b) Ray plots

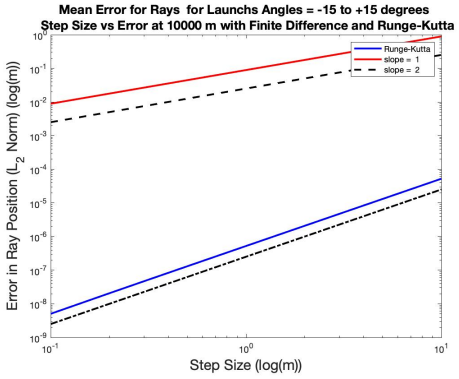

(c) Convergence Plots.

Figure 3-7: Using a less steep SSP gradient and extending the rays to 10^4 m: a) SSP (b) Initial ray trajectories are evenly spaced between 15° above and below the horizontal. Runge-Kutta and forward Euler Rays are computed using a step-size of 1 m with the reference ray trace using Runge-Kutta and a step-size of 10^{-3} m. (c) Convergence rates are identical to those observed when comparing to the analytical solution.

3.4 DO-Ray Feasibility and Implementation

Up to this point, we have discussed why stochastic acoustic computation is relevant, derived governing equations in order to develop and validate a deterministic model for Monte-Carlo comparison. We are hinging the ability of our algorithm's computational accuracy on the presumption that we can represent the variation of a field of ray traces, each corresponding to a specific ocean realization, with a reduced order representation of DO modes and coefficients. Such an approach and corresponding results have been shown to be very efficient for acoustic parabolic PDEs [5, 3, 2].

However, for our novel DO-ray approach, before implementing the algorithm, it is useful to make an empirical assessment as to whether it is possible and to what extent might we be able to reduce the ray trace field using a dynamic reduced-order approach so as the DO-Ray

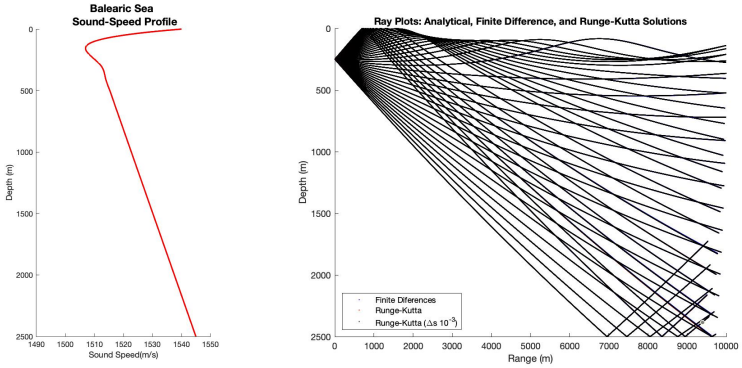

(a) Balearic Sea SSP (b) Ray plots

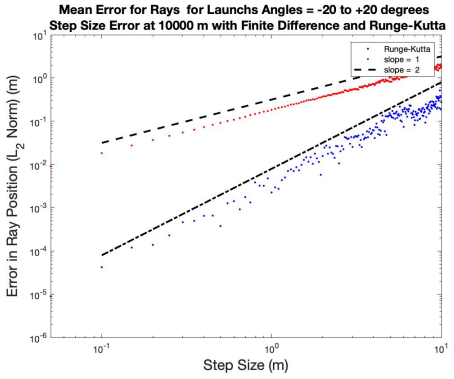

(c) Convergence Plots.

Figure 3-8: Using the Balearic Sea SSP and plotting the rays to 10^4 m. a) Balearic Sea SSP. (b) Initial ray trajectories are even spaced between 15° above and below the horizontal. Runge-Kutta and forward Euler Rays are computed using a step-size of 1 m with the reference ray trace using Runge-Kutta and a step-size of 10^{-3} m. (c) Convergence rates are identical to those observed when comparing to the analytical solution.

ODEs. In the next few sections, we perform this empirical analysis on a distribution of sound-speed profiles similar to those observed in the ocean environment along a single line of latitude. We then evaluate the convergence of our reduced order model as we incorporate more information in the form of additional DO modes.

3.4.1 Feasibility of DO-Ray Stochastic Computation

To evaluate the feasibility of a DO-Ray approach, we desire a distribution of realistic SSPs that are independent, from which we will generate the associated ray traces using our deterministic implementation. [65] provides an example of SSPs at 150°W longitude (see Figure 3-9(a)). For most deep water acoustic propagation over a mesoscale distance, it is unlikely to see the same variability in the SSP as we would if we were to consider an entire line of

longitude. Typically the deeper depths would be relatively constant, even over the course of a year, with most of the variability occurring in the upper $0 - 500$m depths. By observing the feasibility of reducing the acoustic fields ($\mathbf{X}$ and $\mathbf{\Xi}$) with a maximum level of variability over the entire water column, we can observe something akin to a "worse-case-scenario." Hence, we can suppose that for less variable SSP distribution, we may be able to achieve further reduction.

Using Figure 3-9(a) as an example, we created our SSPs by assuming uniform distribution of sound-speed at prescribed depth bands. We further increased the variability by using all permutations of the resultant sound-speed depth combinations. We obtain 5000 independent, uniformly distributed, SSPs loosely based on those in [65]. We then compute the ray traces for every realization. Examples are provided on Figure 3-10.

Recall that we hope to obtain a reduced order representation of the $\mathbf{X}$ and $\mathbf{\Xi}$ states at every step along the ray. We are able to assess the degree to which we can represent the state variables with fewer modes by observing the decay of the singular values of the state variables as we progress along the ray paths. At a step s:

- $\mathbf{U\Sigma V}^T = svd(\{\mathbf{X} - \overline{\mathbf{x}}\}\ or\ \{\mathbf{\Xi} - \overline{\boldsymbol{\xi}}\})$, where $\mathbf{\Sigma}$ is a diagonal matrix of the singular values decreasing in value from top left to bottom right.

We expect that as the ray length increases in distance, the relative positions and direction of ray travel will have a greater variance, and therefore the number of modes required to accurately represent the field should increase.

We performed the computations for every realization using 11, 101, and 1001 rays. The rays in every realization are evenly discretized between $-30°$ to $+30°$. For 11, 101, and 1001 rays the maximum number of singular values or modes that can be used to describe the stochastic field of 5000 oceans are 22, 202, and 2002 respectively.

Figures 3-11 and 3-12 illustrate the feasibility of representing our ray trace stochastic fields using a reduced number of singular values or modes. After a few steps in all 5000 realizations, the stochastic field is not appreciably modified as displayed by the sharp drop off in the log(Singular Value) plot for each singular value in the diagonal $\mathbf{\Sigma}$ matrix. We observe that as the step size increases (i.e. longer rays) the complexity of the stochastic field grows for both ray position and orientation. If we assume that our desire is to capture the stochastic ray trace fields complexity at a ray length of 10 km, we can use these plots for

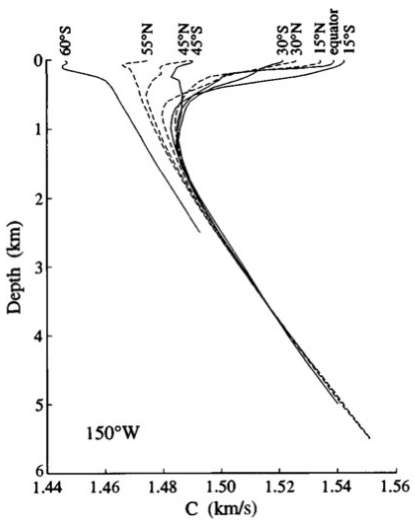

(a) Example SSPs

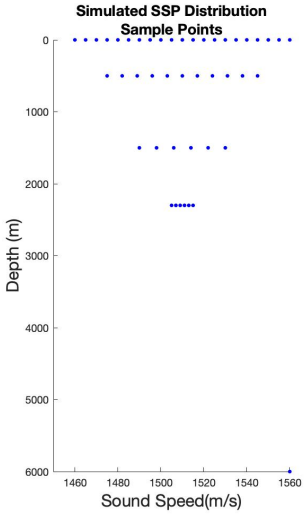

(b) SSP Sample Points

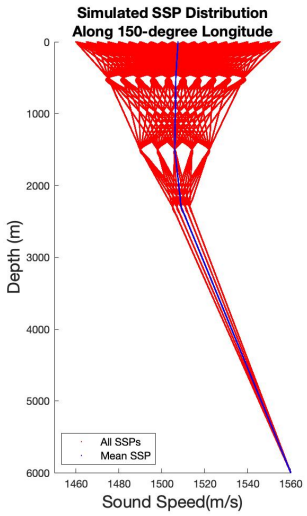

(c) Distribution of Simulated SSPs at 150° Longitude

Figure 3-9: (a) Figure adapted from [65], serving as a starting point to generate simulated SSPs. (b) Based on the previous figure, we created sample points at depths. By connecting all permutations for each depth/sound-speed combinations, we can create 5,000 SSPs. (c) Resultant SSP distribution with a mean SSP plotted for reference. The increase in variability is seen in that some simulated SSPs will take the maximum sound speed at the surface with a minimum sound speed at the 500m and vice versa.

qualitative insights.

First, we observe that the relative drop off in Singular Values becomes less steep as we progress in step length. At a ray length $O(10^2)$ m, the drop off gives insight as to how much of a step length is required to achieve desired amount of variability during the

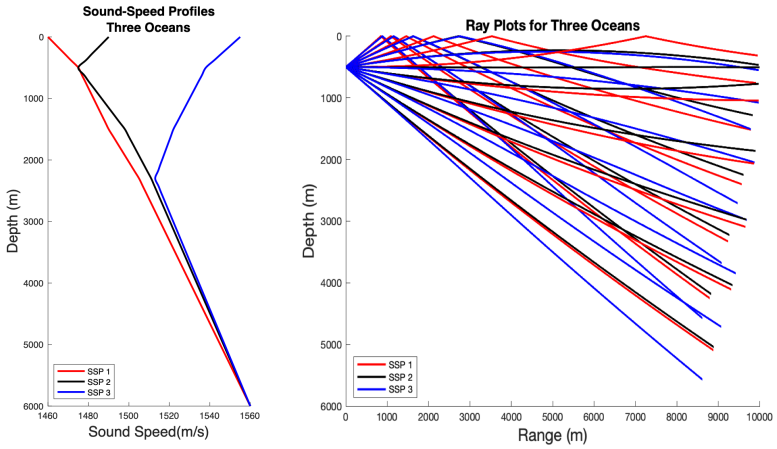

Figure 3-10: Plots show 11 rays with initial angles of $-30°$ to $+30°$, range marched to 10^4m. The difference in the SSPs results in significantly varied Ray Paths.

"initialization" of the DO-Ray implementation. This will be discussed later in this chapter. Second, at 10 km, we find that the singular values drop several orders of magnitude over a small fraction of the total number of singular values, indicating that we may be able to represent the field fairly accurately using a reduced-rank representation for both position and orientation; hence a reduced order representation is feasible.

In Figure 3-13, we see the extent to which we may achieve reduction in the number of modes. For example, when the field is represented by 11 vs 101 rays, we see that a decrease of two orders of magnitude for position ($\mathbf{X}$) occurs at around 6 and 25 singular values (30% and 20% of singular values), respectively. When we compare the number 101 vs 1001 Rays, we see that the number of modes to see the same decrease of two orders of magnitude is around 20 and 100 singular values (20% and 5% respectively). Hence, we are able to gain a greater percent reduction when we represent the realizations with a larger number of rays.

We only observe the relative magnitudes of the singular values as explicit magnitudes of the singular values do not necessarily provide physical insights such as how much the reduction affects the positional error. Knowing this, the first of our qualitative observations serves as a guideline for our DO-ray initialization and may have to be adjusted empirically. The amount of variability in the ray traces is highly dependent on the variability on the SSP between the different ocean realizations at the source position.

For the second of these qualitative assessments, it is important to make a correspondence to the number of modes used to represent the field and the expected error we can expect for the position and orientation error. In the next section, we observe the convergence of the

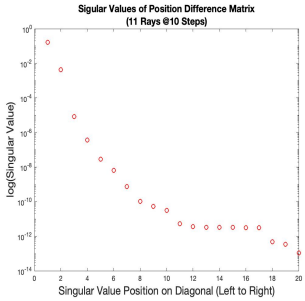

(a) 10 steps $\mathbf{X}$ - 11 Rays

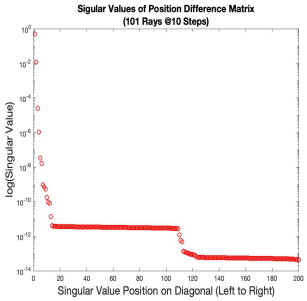

(b) 10 steps $\mathbf{X}$ - 101 Rays

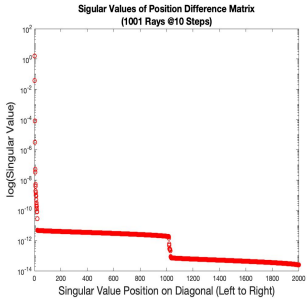

(c) 10 steps $\mathbf{X}$ - 1001 Rays

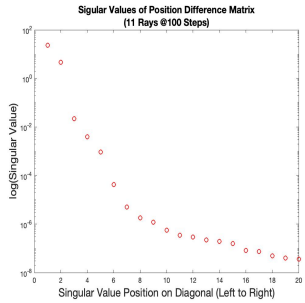

(d) 100 Steps $\mathbf{X}$ - 11 Rays

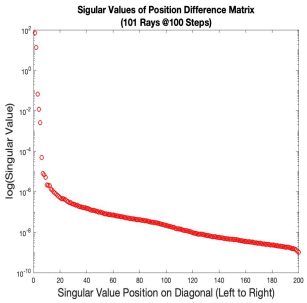

(e) 100 Steps $\mathbf{X}$ - 101 Rays

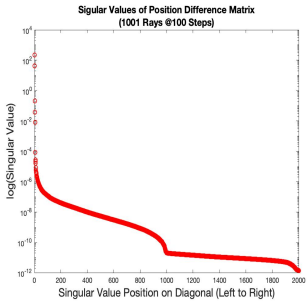

(f) 100 steps $\mathbf{X}$ - 1001 Rays

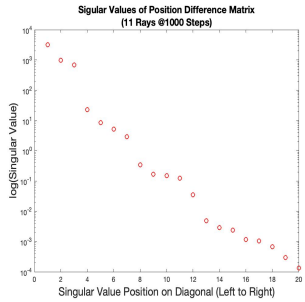

(g) 1000 Steps $\mathbf{X}$ - 11 Rays

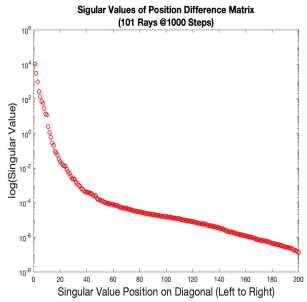

(h) 1000 Steps $\mathbf{X}$ - 101 Rays

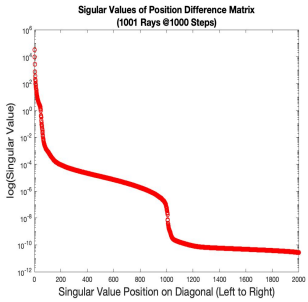

(i) 1000 steps $\mathbf{X}$ - 1001 Rays

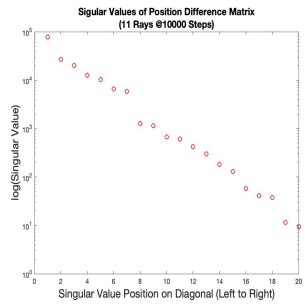

(j) 10000 Steps $\mathbf{X}$ - 11 Rays

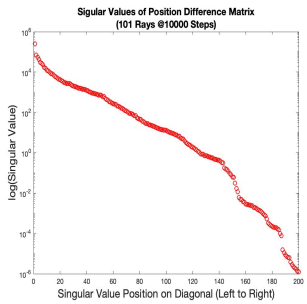

(k) 10000 Steps $\mathbf{X}$ - 101 Rays

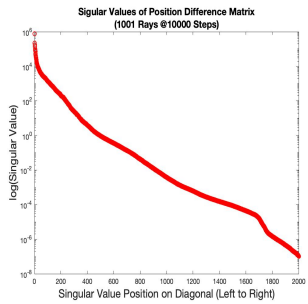

(l) 10000 steps $\mathbf{X}$ - 1001 Rays

Figure 3-11: Singular Values plotted for $(\mathbf{X} - \overline{\mathbf{x}})$ marched to the specified number of 1 m steps for 11, 101, and 1001 Ray stochastic fields. As the fields propagate, more singular values or modes will be required to accurately capture the variability in ray position.

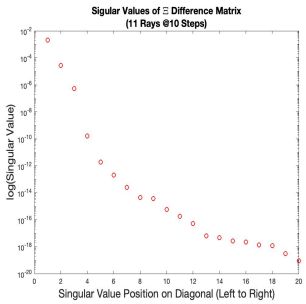

(a) 10 steps $\boldsymbol{\Xi}$ - 11 Rays

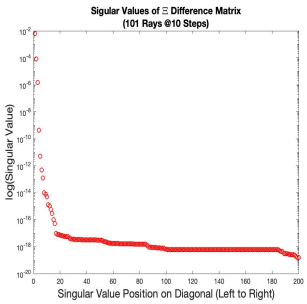

(b) 10 steps $\boldsymbol{\Xi}$ - 101 Rays

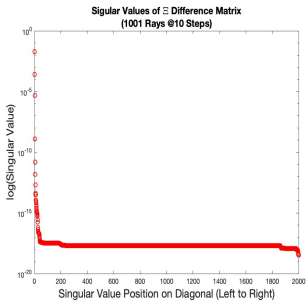

(c) 10 steps $\boldsymbol{\Xi}$ - 1001 Rays

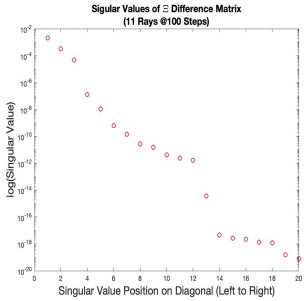

(d) 100 Steps $\boldsymbol{\Xi}$ - 11 Rays

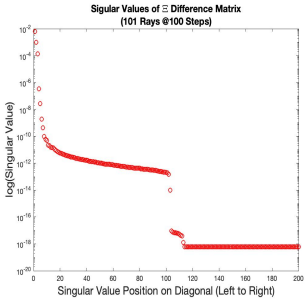

(e) 100 Steps $\boldsymbol{\Xi}$ - 101 Rays

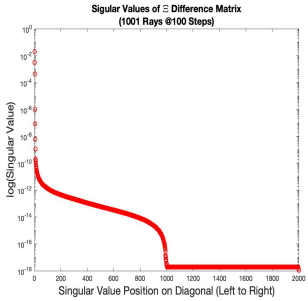

(f) 100 steps $\boldsymbol{\Xi}$ - 1001 Rays

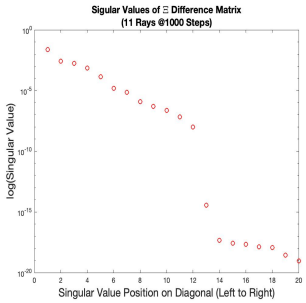

(g) 1000 Steps $\boldsymbol{\Xi}$ - 11 Rays

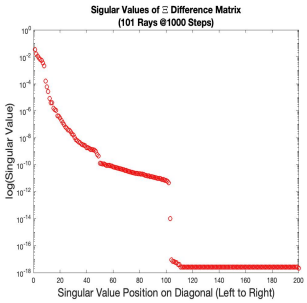

(h) 1000 Steps $\boldsymbol{\Xi}$ - 101 Rays

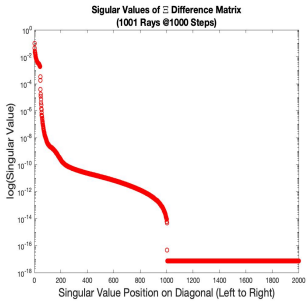

(i) 1000 steps $\boldsymbol{\Xi}$ - 1001 Rays

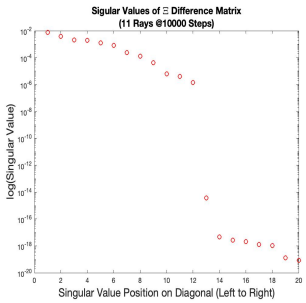

(j) 10000 Steps $\boldsymbol{\Xi}$ - 11 Rays

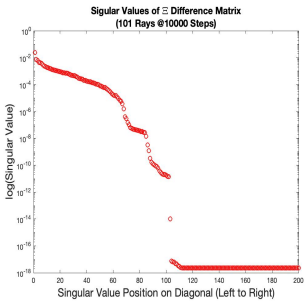

(k) 10000 Steps $\boldsymbol{\Xi}$ - 101 Rays

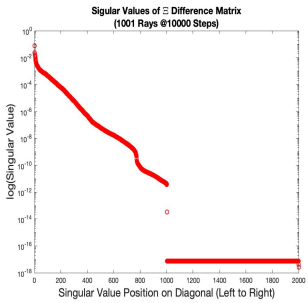

(l) 10000 steps $\boldsymbol{\Xi}$ - 1001 Rays

Figure 3-12: Singular Values plotted for $(\boldsymbol{\Xi} - \overline{\boldsymbol{\xi}})$ marched to the specified number of 1 m steps for both 11, 101, and 1001 Ray stochastic realization fields. As the field propagates, more singular values or modes will be required to accurately capture the variability in ray orientation.

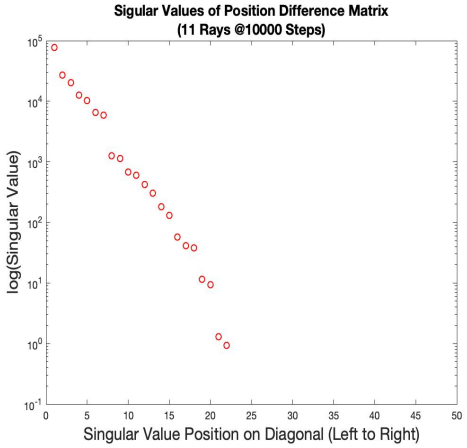

(a) 10000 steps $\mathbf{X}$ - 11 Rays

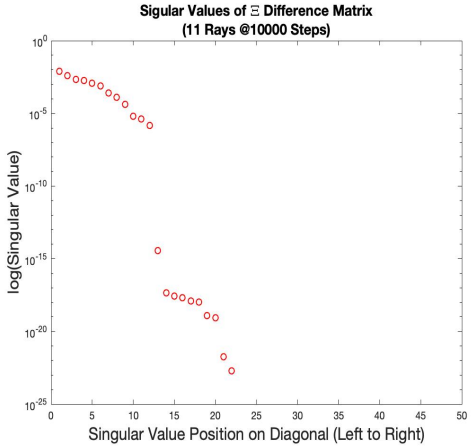

(b) 10000 steps $\boldsymbol{\Xi}$ - 11 Rays

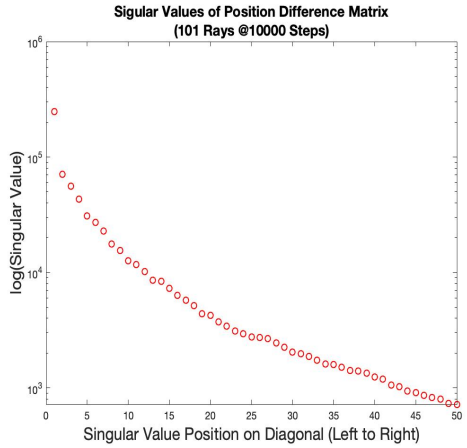

(c) 10000 steps $\mathbf{X}$ - 101 Rays

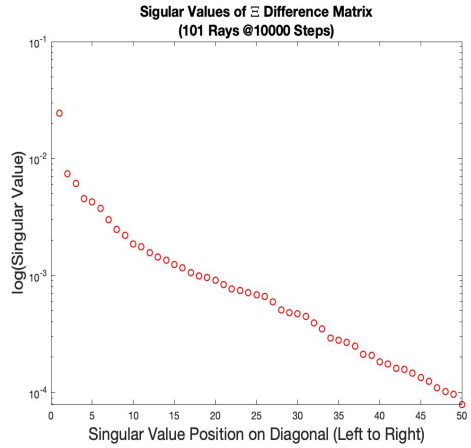

(d) 10000 steps $\boldsymbol{\Xi}$ - 101 Rays

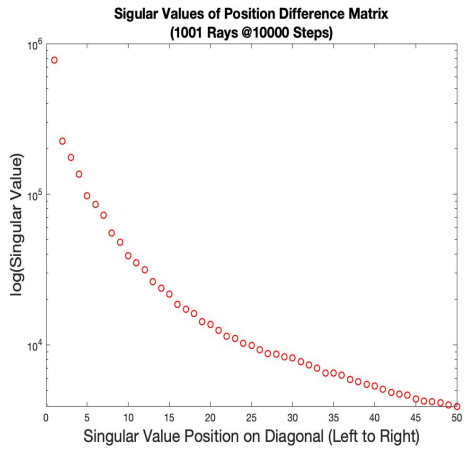

(e) 10000 steps $\mathbf{X}$ - 1001 Rays

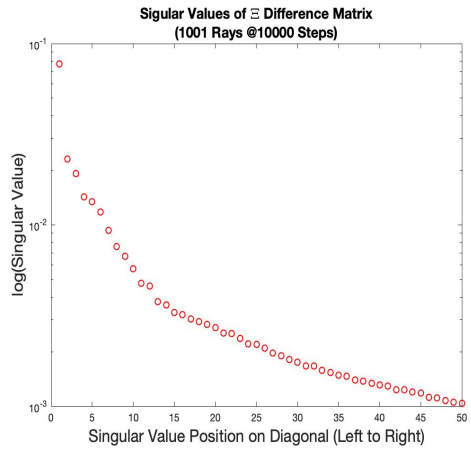

(f) 10000 steps $\boldsymbol{\Xi}$ - 1001 Rays

Figure 3-13: Singular Values plotted for $(\mathbf{X} - \overline{\mathbf{x}})$ and $(\boldsymbol{\Xi} - \overline{\boldsymbol{\xi}})$ marched to 10^4 m for 11, 101, and 1001 Ray stochastic fields. All x-axis are 0 to 50 modes to better allow for for comparing relative drop-off vs. number of modes.

errors as we increase the number of modes for both position and orientation.

3.4.2 Expected Convergence with Number of Mode

Based on the previous section's results, we know it is feasible to use a reduced rank representation to accurately represents the ray trace field, though we have yet to show the extent. We now aim to show how well the stochastic field is represented with a reduced number of singular values and vectors. In other words and for example, when we reduce the number of modes, what is the cost in accuracy at a range of 10^4 m? Using the same realizations from the previous section, we subsequently computed a truncated SVD for all reduced order representations at 10^4 m.

In Figure 3-14 we confirm the qualitative assessments from the previous section with some additional insight. We can achieve an average positional error across all ray and realizations of less than 10 m using 20 of 2002 singular modes/values (1001 Rays); however after the initial rate of convergence, we see that we need to add modes at a higher rate to achieve the same increase in accuracy. Still, these plots confirm that it is feasible to use reduced-order representations for $\mathbf{X}$ by using only approximately 50%, 30%, and 7% of the available modes to represent the fields of 11, 101, and 1001 rays respectively with an expected average error of approximately 1 m.

After performing similar analysis on $\mathbf{\Xi}$, we see similar results. Figure 3-15 shows that with a similar number of modes, the error we observe in our orientation, direction of the ray relative to the horizontal, is only a small fraction of a degree. Based on these results, we can represent the orientation for 1001 rays over a field of 5000 oceans with only 80 modes and expect an error of less than 0.2°.

We also investigate the contribution of the orientation error to the position error over each step. Figure 3-16 is a geometrical representation of how an error in the orientation may result in an error in the range and depth position. For a step size of 1 m, and by making use of the trigonometric identities and the small angle approximation we have:

$$\begin{aligned} \sin(\theta + \theta_e) &= \sin\theta\cos\theta_e + \cos\theta\sin\theta_e \\ &\approx d + r\theta_e = d + d_e \\ r\theta_e &\approx d_e \end{aligned} \tag{3.14}$$

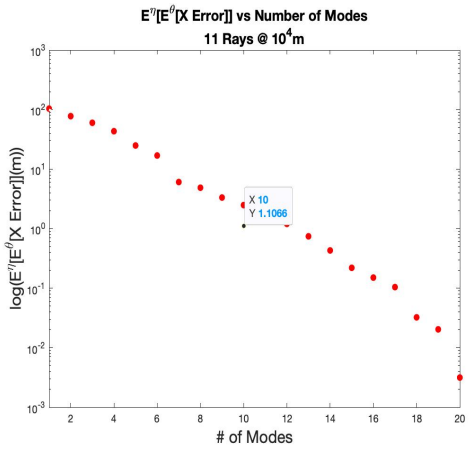

(a) 10000 steps **X** - 11 Rays

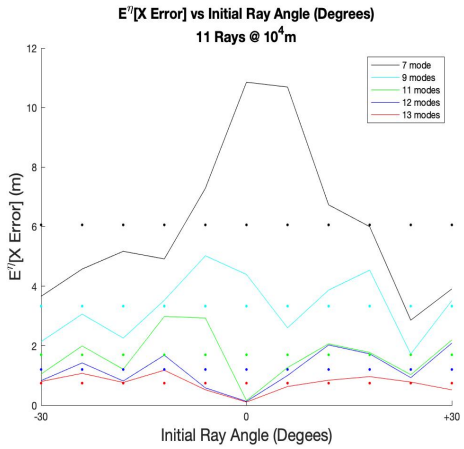

(b) 10000 steps **X** - 11 Rays

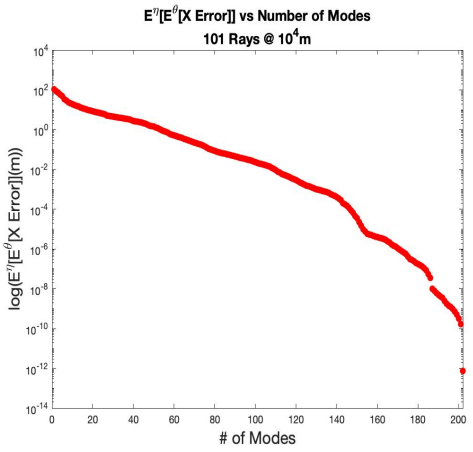

(c) 10000 steps **X** - 101 Rays

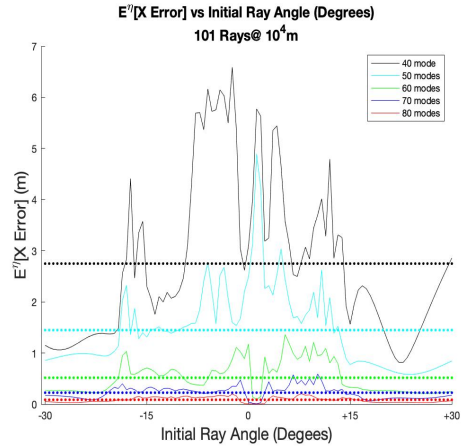

(d) 10000 steps **X** - 101 Rays

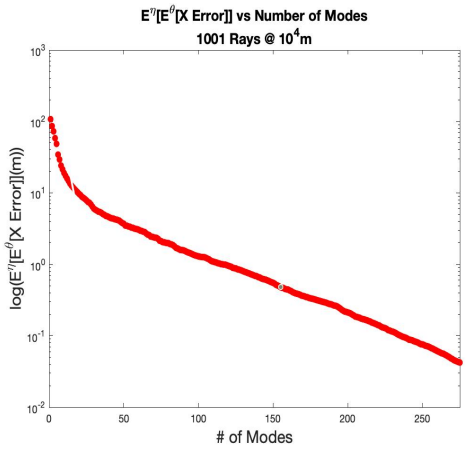

(e) 10000 steps **X** - 1001 Rays

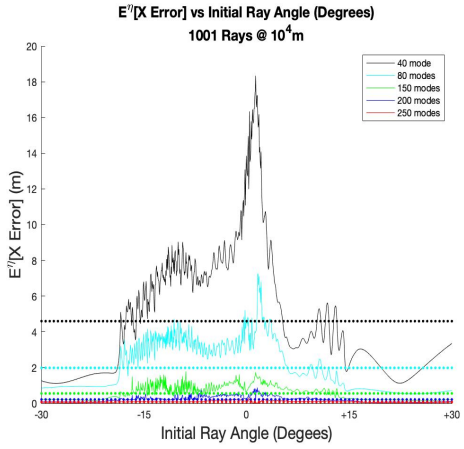

(f) 10000 steps **X** - 1001 Rays

Figure 3-14: Plots on the left for 11, 101, and 1001 Rays show how the positional error converges as we increase the number of modes. Sloped lines are provided to provide relative orders of convergence. The plots on the right show how the error changes for individual rays with dotted lines to indicate the average errors across all rays.

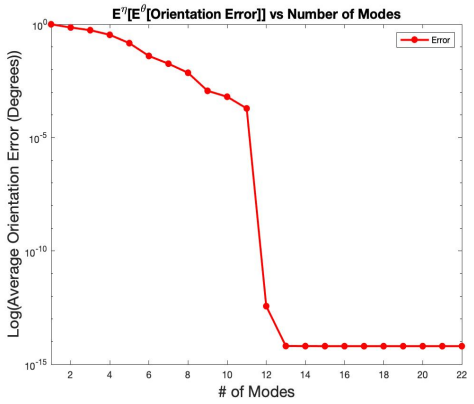

(a) 10000 steps Ξ - 11 Rays

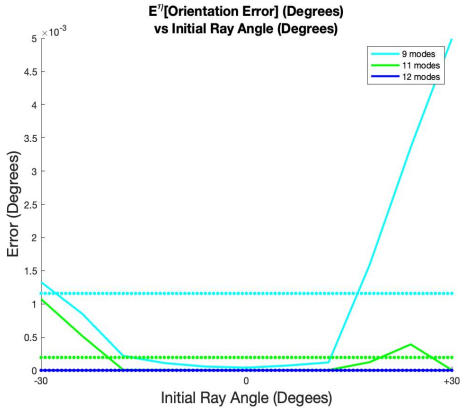

(b) 10000 steps Ξ - 11 Rays

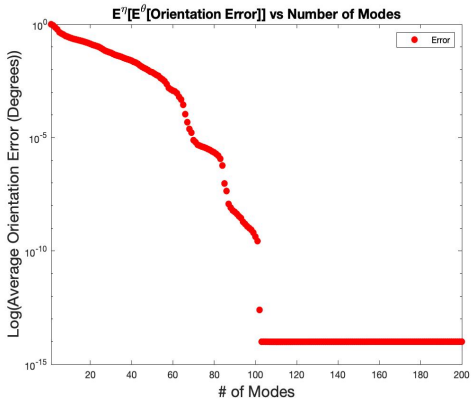

(c) 10000 steps Ξ - 101 Rays

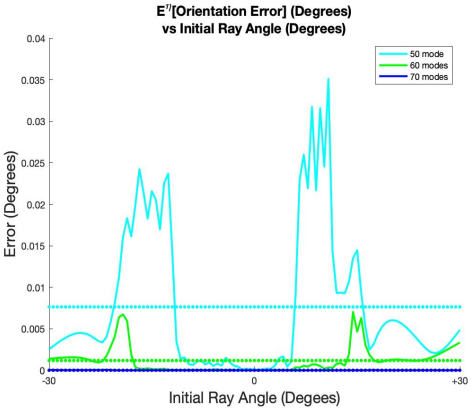

(d) 10000 steps Ξ - 101 Rays

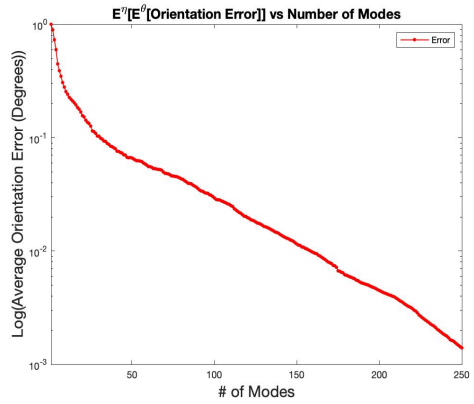

(e) 10000 steps Ξ - 1001 Rays

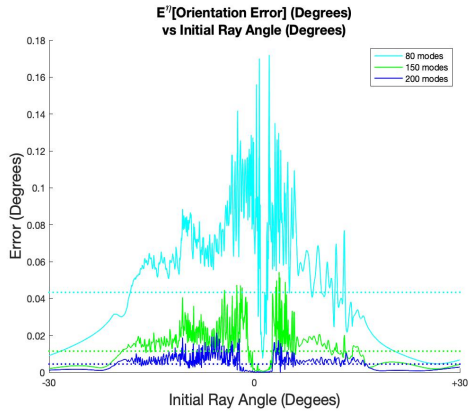

(f) 10000 steps Ξ - 1001 Rays

Figure 3-15: Plots on the left for 11, 101, and 1001 Rays show how the orientation error converges as we increase the number of modes. The plots on the right show how the error changes for individual rays with dotted lines to indicate the average errors across all rays. While the reduced representation is on the Ξ field, we converted the y-axis to degrees in order to give a physical interpretation of the expected error vs the number of modes used.

We also have:

$$\begin{aligned} \cos(\theta + \theta_e) &= \cos\theta\cos\theta_e + \sin\theta\sin\theta_e \\ &\approx r + d\theta_e = r + r_e \\ d\theta_e &\approx r_e \end{aligned} \tag{3.15}$$

Therefor the magnitude of the positional error induce by our small orientation error in one step can be approximated as:

$$|\mathbf{x}_e| \approx \sqrt{(r\theta_e)^2 + (d\theta_e)^2} = \theta_e \text{ (in radians)} \tag{3.16}$$

Therefore we see that a 0.2° orientation error at a given step corresponds to a 3.5mm error in position on the following step for a 1m step size.

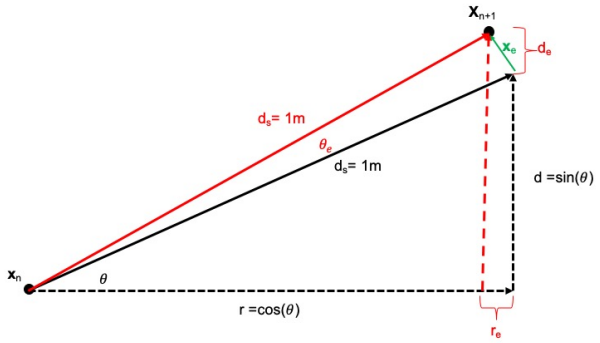

Figure 3-16: Geometric representation of a ray path and the error introduced by the error in orientation.

In summary, we computed ray traces for 5000 very different ocean environments. By observing the decay of the singular values as we increased the ray lengths, we see that at each step we can use a reduced-rank representation to predict the field of stochastic ray traces. We then computed physical values for orientation and range error to see how they decay as we incorporate additional modes. By doing this we not only confirm the feasibility of a reduced-order representation, but also gain intuition of how many steps are needed for initialization, as well as the number of singular values needed for an accurate representation of the field.

3.5 Dynamically Orthogonal Field Equations (DO) Derivation

Now that our assumptions regarding the opportunity for reduction are supported in the previous section, we derive the stochastic DO-Ray differential equations. The derivations may be burdensome with notations. For simplicity, when annotating state variables or ocean realizations, we do not always include the dependent variable. To understand the derivation it is useful to introduce the following definitions and concept:

- When we use the term field ($\mathbf{X}$ and $\mathbf{\Xi}$), we are considering multiple realizations, typically O(10^3 to 10^4) and possibly much more, with each realization characterized by an $\mathbf{x}$ and $\boldsymbol{\xi}$ pair forming a column of the matrices $\mathbf{X}$ and $\mathbf{\Xi}$. After subtracting the mean of all realizations we perform a singular value decomposition to obtain the DO modes and coefficients.
  - For example, $\mathbf{U}\mathbf{\Sigma}\mathbf{V}^T = svd(\mathbf{X} - \mathbb{E}^\eta[\mathbf{X}])$, where the DO modes $\tilde{\mathbf{x}}$ are the columns of $\mathbf{U}$, and the DO coefficients, corresponding to a particular realization, are the rows of $\mathbf{\Sigma}\mathbf{V}^T$.
- Realizations of stochastic state variables $\boldsymbol{\xi}(s;\eta)$ and $\mathbf{x}(s;\eta)$ dependent on "s" and correspond to a particular ocean realization. They also have their stochastic representations for a particular realization "η":

  $\boldsymbol{\xi}(s;\eta) \equiv \boldsymbol{\xi} = \overline{\boldsymbol{\xi}} + \tilde{\boldsymbol{\xi}}_i \gamma_i$

  $\mathbf{x}(s;\eta) \equiv \mathbf{x} = \overline{\mathbf{x}} + \tilde{\mathbf{x}}_i \beta_i$
- The stochastic means and DO modes are only a function of "s":

  $\overline{\boldsymbol{\xi}}_i(s) \equiv \overline{\boldsymbol{\xi}}_i$ and $\tilde{\boldsymbol{\xi}}_i(s) \equiv \tilde{\boldsymbol{\xi}}_i$

  $\overline{\mathbf{x}}(s) \equiv \overline{\mathbf{x}}$ and $\tilde{\mathbf{x}}_i(s) \equiv \tilde{\mathbf{x}}_i$
- The DO coefficients are dependent on "η" and correspond to a particular ocean realization:

  $\gamma_i(s;\eta) \equiv \gamma_i$

  $\beta_i(s;\eta) \equiv \beta_i$
- The sound speed along a stochastic ray depends on position $\mathbf{x}(s;\eta)$ and correspond to a particular ocean:

$$c(\mathbf{x}(s;\eta);\eta) \equiv c(\mathbf{x})$$

3.5.1 Evolution of the Stochastic Mean $\left(\frac{d\overline{\boldsymbol{\xi}}(s)}{ds}, \frac{d\overline{\mathbf{x}}(s)}{ds}\right)$

We begin with the stochastic versions of (3.3) and (3.4). Inserting the decomposition (3.1) and (3.2) respectively, we obtain:

$$\begin{aligned} \frac{d}{ds}(\overline{\boldsymbol{\xi}} + \tilde{\boldsymbol{\xi}}_i\gamma_i) &= -\frac{1}{c(\mathbf{x})^2}\nabla c(\mathbf{x}) \\ \frac{d}{ds}(\overline{\mathbf{x}} + \tilde{\mathbf{x}}_i\beta_i) &= c(\mathbf{x})\boldsymbol{\xi} \end{aligned} \tag{3.17}$$

We then take the expectation ($\mathbb{E}^\eta$) of (3.17) over all ocean realizations:

$$\begin{aligned} \frac{d}{ds}\mathbb{E}^\eta[\overline{\boldsymbol{\xi}}] + \frac{d\mathbb{E}^\eta[\gamma_i]}{ds}\tilde{\boldsymbol{\xi}}_i + \mathbb{E}^\eta[\gamma_i]\frac{d\tilde{\boldsymbol{\xi}}_i}{ds} &= \mathbb{E}^\eta\left[-\frac{1}{c(\mathbf{x})^2}\nabla c(\mathbf{x})\right] \\ \frac{d}{ds}\mathbb{E}^\eta[\overline{\mathbf{x}}] + \frac{d\mathbb{E}^\eta[\beta_i]}{ds}\tilde{\mathbf{x}}_i + \mathbb{E}^\eta[\beta_i]\frac{d\tilde{\mathbf{x}}_i}{ds} &= \mathbb{E}^\eta\Big[c(\mathbf{x})\boldsymbol{\xi}\Big] \end{aligned} \tag{3.18}$$

Applying the fact that $\mathbb{E}^\eta[\gamma_i(s;\eta)] = 0$ and $\mathbb{E}^\eta[\beta_i(s;\eta)] = 0$ by definition, we are left with:

$$\begin{aligned} \frac{d\overline{\boldsymbol{\xi}}}{ds} &= \mathbb{E}^\eta\left[-\frac{1}{c(\mathbf{x})^2}\nabla c(\mathbf{x})\right] \\ \frac{d\overline{\mathbf{x}}}{ds} &= \mathbb{E}^\eta\Big[c(\mathbf{x})\boldsymbol{\xi}\Big] \end{aligned} \tag{3.19}$$

to describe how the stochastic mean of the acoustic ray trace field propagates.

3.5.2 Evolution of the DO Coefficients $\left(\frac{d\gamma_i(s;\eta)}{ds}, \frac{d\beta_i(s;\eta)}{ds}\right)$

Starting again with (3.17), we subtract (3.19) and take the projection onto $\tilde{\boldsymbol{\xi}}_j(s)$ and $\tilde{\mathbf{x}}_j(s)$, respectively, to obtain:

$$\begin{aligned} \frac{d\gamma_i}{ds}\langle\tilde{\boldsymbol{\xi}}_i, \tilde{\boldsymbol{\xi}}_j\rangle + \gamma_i\left\langle\frac{d\tilde{\boldsymbol{\xi}}_i}{ds}, \tilde{\boldsymbol{\xi}}_j\right\rangle &= \left\langle -\frac{1}{c(\mathbf{x})^2}\nabla c(\mathbf{x}) - \mathbb{E}^\eta\left[-\frac{1}{c(\mathbf{x})^2}\nabla c(\mathbf{x})\right], \tilde{\boldsymbol{\xi}}_j\right\rangle \\ \frac{d\beta_i}{ds}\langle\tilde{\mathbf{x}}_i, \tilde{\mathbf{x}}_j\rangle + \beta_i\left\langle\frac{d\tilde{\mathbf{x}}_i}{ds}, \tilde{\mathbf{x}}_j\right\rangle &= \left\langle c(\mathbf{x})\boldsymbol{\xi} - \mathbb{E}^\eta\Big[c(\mathbf{x})\boldsymbol{\xi}\Big], \tilde{\mathbf{x}}_j\right\rangle \end{aligned} \tag{3.20}$$

Applying the DO condition described in Chapter 2, we obtain:

$$\begin{aligned}\frac{d\gamma_j}{ds} &= \left\langle -\frac{1}{c(\mathbf{x})^2}\nabla c(\mathbf{x}) - \mathbb{E}^\eta\left[-\frac{1}{c(\mathbf{x})^2}\nabla c(\mathbf{x})\right], \tilde{\boldsymbol{\xi}}_j \right\rangle \\ \frac{d\beta_j}{ds} &= \left\langle c(\mathbf{x})\boldsymbol{\xi} - \mathbb{E}^\eta\left[c(\mathbf{x})\boldsymbol{\xi}\right], \tilde{\mathbf{x}}_j \right\rangle\end{aligned} \tag{3.21}$$

to describe how the DO coefficients evolve with each step "s".

3.5.3 Evolution of the DO Modes$\left(\frac{d\tilde{\boldsymbol{\xi}}_i(s)}{ds}, \frac{d\tilde{\mathbf{x}}_i(s)}{ds}\right)$

Starting again with (3.17), we project onto the stochastic space by multiplying with the stochastic DO coefficients (γ_k,β_k) and take the expectation to obtain:

$$\begin{aligned}\frac{d\overline{\boldsymbol{\xi}}}{ds}\mathbb{E}^\eta[\gamma_k] + \mathbb{E}^\eta\left[\frac{d[\gamma_i]}{ds}\gamma_k\right]\tilde{\boldsymbol{\xi}}_i + \mathbb{E}^\eta[\gamma_i\gamma_k]\frac{d\tilde{\boldsymbol{\xi}}_i}{ds} &= \mathbb{E}^\eta\left[-\frac{\gamma_k}{c(\mathbf{x})^2}\nabla c(\mathbf{x})\right] \\ \frac{d\overline{\mathbf{x}}}{ds}\mathbb{E}^\eta[\beta_k] + \mathbb{E}^\eta\left[\frac{d[\beta_i]}{ds}\beta_k\right]\tilde{\mathbf{x}}_i + \mathbb{E}^\eta[\beta_i\beta_k]\frac{d\tilde{\mathbf{x}}_i}{ds} &= \mathbb{E}^\eta\left[c(\mathbf{x})\boldsymbol{\xi}\beta_k\right]\end{aligned} \tag{3.22}$$

We can also multiply (3.21) by the stochastic DO coefficients (γ_k,β_k) and take the expectation to obtain a representation of the second terms in (3.22):

$$\begin{aligned}\mathbb{E}^\eta\left[\frac{d[\gamma_i]}{ds}\gamma_k\right] &= \mathbb{E}^\eta\left[\left\langle -\frac{1}{c(\mathbf{x})^2}\nabla c(\mathbf{x}) - \mathbb{E}^\eta\left[-\frac{1}{c(\mathbf{x})^2}\nabla c(\mathbf{x})\right], \tilde{\boldsymbol{\xi}}_j\right\rangle\gamma_k\right] \\ \mathbb{E}^\eta\left[\frac{d[\beta_i]}{ds}\beta_k\right] &= \mathbb{E}^\eta\left[\left\langle c(\mathbf{x})\boldsymbol{\xi} - \mathbb{E}^\eta\left[c(\mathbf{x})\boldsymbol{\xi}\right], \tilde{\mathbf{x}}_j\right\rangle\beta_k\right]\end{aligned} \tag{3.23}$$

After substituting (3.23) into (3.22) and rearranging to solve for the DO modes, we arrive at:

$$\begin{aligned}\frac{d\tilde{\boldsymbol{\xi}}_i}{ds} &= \left[\mathbb{E}^\eta\left[-\frac{\gamma_k}{c(\mathbf{x})^2}\nabla c(\mathbf{x})\right] - \mathbb{E}^\eta\left[\left\langle -\frac{1}{c(\mathbf{x})^2}\nabla c(\mathbf{x}) - \mathbb{E}^\eta\left[-\frac{1}{c(\mathbf{x})^2}\nabla c(\mathbf{x})\right], \tilde{\boldsymbol{\xi}}_j\right\rangle\gamma_k\right]\tilde{\boldsymbol{\xi}}_i\right]\left\{\mathbb{E}^\eta[\gamma_i\gamma_k]\right\}^{-1} \\ \frac{d\tilde{\mathbf{x}}_i}{ds} &= \left[\mathbb{E}^\eta\left[c(\mathbf{x})\boldsymbol{\xi}\beta_k\right] - \mathbb{E}^\eta\left[\left\langle c(\mathbf{x})\boldsymbol{\xi} - \mathbb{E}^\eta\left[c(\mathbf{x})\boldsymbol{\xi}\right], \tilde{\mathbf{x}}_j\right\rangle\beta_k\right]\tilde{\mathbf{x}}_i\right]\left\{\mathbb{E}^\eta[\beta_i\beta_k]\right\}^{-1}\end{aligned} \tag{3.24}$$

to describe how the the DO modes of the stochastic acoustic ray trace field propagate with each step "s".

3.6 Stochastic DO-Ray Algorithms and Reduced-Order Representations

In this section we first write the previously derived DO equations in a realization matrix form. Looking at these matrices, we can see where we are introducing the reduced-order representation of our stochastic field.

3.6.1 Matrix Representations

Prior to computing and evolving the stochastic field consisting of H realizations, we select two computational parameters from which we will construct a reduced representation:

- the number of rays, R, used to form the ray trace,
- the number of DO modes, M, necessary to capture the variation between the H (# of oceans) different traces.

Here we define the matrices used in the matrix notation of the DO-Ray equations and specify the dimensions of each:

- $\mathbf{X}$ is comprised of all ray positions for all realizations at a particular range-step s. $\mathbf{X}_r$ and $\mathbf{X}_d$ correspond to range and depth components respectively. Both $\mathbf{X}_r$ and $\mathbf{X}_d$ are $R \times H$ size matrices. Similarly $\boldsymbol{\Xi}$ is comprised of all $\boldsymbol{\xi}$ for all realizations at a particular step along the ray. $\boldsymbol{\Xi}_r$ and $\boldsymbol{\Xi}_d$ correspond to range and depth components respectively. Both $\boldsymbol{\Xi}_r$ and $\boldsymbol{\Xi}_d$ are a$R \times H$ size matrices.
- Both $\mathbf{X}$ and $\boldsymbol{\Xi}$ can be decomposed into their respective means, DO modes, and DO coefficients for a particular range-step "s".

  $$\mathbf{X}_{r,d} = \overline{\mathbf{x}}_{r,d} + \tilde{\mathbf{X}}_{r,d} B$$

  $$\boldsymbol{\Xi}_{r,d} = \overline{\boldsymbol{\xi}}_{r,d} + \tilde{\boldsymbol{\Xi}}_{r,d} \Gamma$$

- The range and depth components of $\overline{\boldsymbol{\xi}}_{r,d}$ and $\overline{\mathbf{x}}_{r,d}$ are vectors of length R.
- DO mode matrices: $dim(\tilde{\mathbf{X}}_{r,d}) = R \times M$; $dim(\tilde{\boldsymbol{\Xi}}_{r,d}) = R \times M$.
- DO coefficient matrices: $dim(B) = dim(\Gamma) = M \times H$
- $\mathbf{C} = c_{\eta=1:H}(\mathbf{X})$; $dim(\mathbf{C}) = R \times H$.

- $\mathbf{C}_x = \frac{1}{c^2_{\eta=1:H}(\mathbf{X})}$; $dim(\mathbf{C}_x) = R \times H$.

- $\nabla_{r,d}\mathbf{C} = \nabla_{r,d}C(\mathbf{X})$, where ∇_r and ∇_d represent the range and depth components of the gradients respectively. $dim(\nabla_{r,d}\mathbf{C}) = R \times H$

Evolution of the DO Means

From Equation (3.19) we can put the equation in matrix form:

$$\frac{d\overline{\mathbf{x}}_{r,d}}{ds} = \mathbb{E}^{\eta}\Big[\mathbf{C}. * (\overline{\boldsymbol{\xi}}_{r,d} + \tilde{\boldsymbol{\Xi}}_{r,d}\Gamma)\Big] \tag{3.25}$$

and

$$\frac{d\overline{\xi}_{r,d}}{ds} = \mathbb{E}^{\eta}\Big[\mathbf{C}. * \nabla_{r,d}\mathbf{C}\Big] \tag{3.26}$$

Evolution of the DO Coefficients

From Equation (3.21):

$$\begin{aligned}\frac{d}{ds}[B] = \tilde{\mathbf{X}}_r^T\big(\mathbf{C}. * \overline{\boldsymbol{\xi}_r} + \mathbf{C}. * (\tilde{\boldsymbol{\Xi}}_r\Gamma) - \frac{d\overline{\mathbf{x}_r}}{ds}\big) \\ + \tilde{\mathbf{X}}_d^T\big(\mathbf{C}. * \overline{\boldsymbol{\xi}_d} + \mathbf{C}. * (\tilde{\boldsymbol{\Xi}}_d\Gamma) - \frac{d\overline{\mathbf{x}_d}}{ds}\big)\end{aligned} \tag{3.27}$$

and

$$\begin{aligned}\frac{d}{ds}[\Gamma] = \tilde{\boldsymbol{\Xi}}_r^T\big(-\mathbb{E}^{\eta}\big[\mathbf{C}_x. * \nabla_r\mathbf{C}\big] - \mathbf{C}_x. * \nabla_r\mathbf{C}\big) \\ + \tilde{\boldsymbol{\Xi}}_r^T\big(-\mathbb{E}^{\eta}\big[\mathbf{C}_x. * \nabla_d\mathbf{C}\big] - \mathbf{C}_x. * \nabla_d\mathbf{C}\big)\end{aligned} \tag{3.28}$$

Evolution of the DO Modes

From Equation (3.24):

$$\begin{aligned}\frac{d\tilde{\mathbf{X}}_r}{ds} &= \left[\frac{1}{\eta}\mathbf{C}_x. * (\overline{\boldsymbol{\xi}}_r + \tilde{\boldsymbol{\Xi}}_r\Gamma)B^T - \tilde{\mathbf{X}}_r\left(\frac{1}{\eta}\left(\frac{dB}{ds}B^T\right)\right)\right]Cov\big\{B^T\big\}^{-1} \\ \frac{d\tilde{\mathbf{X}}_d}{ds} &= \left[\frac{1}{\eta}\mathbf{C}_x. * (\overline{\boldsymbol{\xi}}_d + \tilde{\boldsymbol{\Xi}}_d\Gamma)B^T - \tilde{\mathbf{X}}_d\left(\frac{1}{\eta}\left(\frac{dB}{ds}B^T\right)\right)\right]Cov\big\{B^T\big\}^{-1}\end{aligned} \tag{3.29}$$

and

$$\begin{aligned}\frac{d\tilde{\boldsymbol{\Xi}}_r}{ds} &= \left[\frac{1}{H}\big((\mathbf{C}_{x\cdot} * \nabla_r \mathbf{C})\Gamma^T\big) - \tilde{\boldsymbol{\Xi}}_r\left(\frac{1}{H}\left(\frac{d\Gamma}{ds}\Gamma^T\right)\right)\right] Cov\{\Gamma^T\}^{-1} \\ \frac{d\tilde{\boldsymbol{\Xi}}_d}{ds} &= \left[\frac{1}{H}\big((\mathbf{C}_{x\cdot} * \nabla_d \mathbf{C})\Gamma^T\big) - \tilde{\boldsymbol{\Xi}}_d\left(\frac{1}{H}\left(\frac{d\Gamma}{ds}\Gamma^T\right)\right)\right] Cov\{\Gamma^T\}^{-1}\end{aligned} \tag{3.30}$$

3.6.2 Reduced Order Representation of the Nonlinear Stochastic SSP along Stochastic Acoustic Rays

Now that we see the discrete matrix-form DO-Ray evolution equations, it is apparent that though we have reduced representations of the acoustic field, the computational cost can be higher with a DO-Ray computation as compared to a Monte Carlo approach. Hence, we now delve into why our present DO-Ray implementation can be less efficient than a direct Monte-Carlo scheme. Later, we provide ideas on how this can be remedied.

At each step in the evolution, we presently compute the sound-speed for each individual ray, for all ocean realizations, at every step ($H \times R$ computations). This inefficiency exists for both Monte-Carlo and DO implementations; however, where we gained efficiency in reducing our representation of the stochastic field, in the above implementation, we lose some efficiency in having to reconstitute all realizations in order to evaluate the sound speeds for the next step along each advancing ray. It is important to understand why we cannot obtain the additional reduction in the sound-speed distribution with the above equations, in order to provide guidance on how one may be able to increase efficiency in future work.

Consider an arbitrary distribution of SSP measurements for which we can form functions $c_{1:H}(\mathbf{x})$ similarly to how we form the sound speed profiles earlier in this chapter. As we decompose the stochastic fields of the acoustic ray state variables, we could decompose c into its mean, DO modes and coefficients:

$$c(\mathbf{x}(s;\eta);\eta) = \overline{c}(\mathbf{x}(s;\eta)) + \tilde{c}_j(\mathbf{x}(s;\eta))\alpha_j(\eta) \tag{3.31}$$

where our stochastic location field $\mathbf{x}$ along a stochastic ray is both a function of the step along the ray and of the ocean realization. Presently, the sound speed profiles are frozen in time and are only dependent on the realization selected and spatial location. Inserting the

stochastic representations of $\mathbf{x}$ in (3.31), we have:

$$c(\overline{\mathbf{x}} + \tilde{\mathbf{x}}_i\beta_i(\eta);\eta) = \overline{c}(\overline{\mathbf{x}} + \tilde{\mathbf{x}}_i\beta_i(\eta)) + \tilde{c}_j(\overline{\mathbf{x}} + \tilde{\mathbf{x}}_i\beta_i(\eta))\,\alpha_j(\eta)\,. \tag{3.32}$$

To exemplify the computational issues involved with the nonlinear evaluation of the stochastic sound-speed along stochastic rays, we discuss the evolution of the stochastic mean (3.19) with the added reduced order in $c_{1:H}(\mathbf{x})$. We start by inserting (3.32) into (3.17) and take the expectations over all ocean realizations to obtain the revised RHS of (3.18) and (3.19):

$$\begin{aligned} LHS_{\boldsymbol{\xi}} &= \mathbb{E}^{\eta}\Bigg[-\frac{1}{\Big(\overline{c}(\overline{\mathbf{x}} + \tilde{\mathbf{x}}_i\beta_i(\eta)) + \tilde{c}_j(\overline{\mathbf{x}} + \tilde{\mathbf{x}}_i\beta_i(\eta))\alpha_j(\eta)\Big)^2}\nabla\Big(\overline{c}(\overline{\mathbf{x}} + \tilde{\mathbf{x}}_i\beta_i(\eta)) + \tilde{c}_j(\overline{\mathbf{x}} + \tilde{\mathbf{x}}_i\beta_i(\eta))\,\alpha_j(\eta)\Big)\Bigg] \\ LHS_{\mathbf{x}} &= \mathbb{E}^{\eta}\Bigg[\Big(\overline{c}(\overline{\mathbf{x}} + \tilde{\mathbf{x}}_i\beta_i(\eta)) + \tilde{c}_j(\overline{\mathbf{x}} + \tilde{\mathbf{x}}_i\beta_i(\eta))\,\alpha_j(\eta)\Big)\boldsymbol{\xi}(\eta)\Bigg] \end{aligned} \tag{3.33}$$

Consider the latter equation of (3.33). Without going into the details of computing the RHS, we need to compute $\mathbb{E}^{\eta}\big[\big(\overline{c}(\overline{\mathbf{x}} + \tilde{\mathbf{x}}_i\beta_i(\eta)) + \tilde{c}_j(\overline{\mathbf{x}} + \tilde{\mathbf{x}}_i\beta_i(\eta))\,\alpha_j(\eta)\big)\boldsymbol{\xi}\big]$ or more simply $\mathbb{E}^{\eta}[c(\mathbf{x}(s;\eta);\eta)\boldsymbol{\xi}]$. Unless we have an equation that describes the functional relationship between the position and the sound speed along a particular ray, there is no analytical way to compute this expectation over all realizations. There are nonetheless a few approximations that we discuss next, with an increasing level of stochastic accuracy.

Local sound-speed mean approximation. First, we could make an approximation for the stochastic ray traces, with the most simple being $\overline{\mathbf{x}} + \tilde{\mathbf{x}}_i\beta_i \approx \overline{\mathbf{x}}$. With this approximation we arrive at:

$$c(\mathbf{x}(s;\eta);\eta) \approx \overline{c}(\overline{\mathbf{x}}) + \tilde{c}_j(\overline{\mathbf{x}})\alpha_j(\eta) \tag{3.34}$$

and thus $\mathbb{E}^{\eta}[c(\mathbf{x}(s;\eta);\eta)] \approx \mathbb{E}^{\eta}\big[\overline{c}(\overline{\mathbf{x}}) + \tilde{c}_j(\overline{\mathbf{x}})\alpha_j(\eta)\big]$. This zeroth-order stochastic approximation is similar to the assumption we made with the example application of EOFs in tomography in that we are assuming that perturbation in the rays across all realizations are relatively small. Therefore the sound-speed for all realizations is approximated as the sound speed for the mean profile plus a DO decomposition. Consider a distribution of constant positive sound speed profiles for which we have computed the mean profile. When considering the ray paths after some significant number of range steps the mean ray position may be a decent approximation and the sound-speed gradient exact as it is constant and positive.

Let's discuss this zeroth-order approximation of the sound-speed and imagine the situation where the sound speed has a probability distribution of constant both positive and negative sound speed gradients. Even though we have a better approximation to account for the ray path error in the different realizations, the effect of the sound speed gradients on the ray path, where the mean is no longer an accurate approximation, will result in inaccurate representations of how the ray will bend. Using the mean sound-speed gradient as an approximation would result in an altered ray path as the gradients may have opposite signs.

It is feasible to construct scenarios under which this methodology could make the approximations above and reduce the computational cost of the DO-Ray methodology; however these could be overly specific and therefore are not considered in this thesis.

This illustrates an important point when considering the DO-Ray computational method based on the mean ocean only. The mean ray propagation in a non-Gaussian distribution could be nonphysical and is unlikely to approximate all of the other realizations. We also note that propagation and dynamics of the DO modes are only basis functions that describe the most variance and do not always correspond to specific acoustic physical process. They are intermediate computational quantities from which physical realizations can be reconstructed by linear combinations of the DO modes multiplied by the DO coefficients.

Local sound-speed Taylor-Series approximation. Second, if we were to deem that the error in ray position after the requisite number of steps would result in too large an error in sound-speed computation, we could consider consider first-order Taylor series expansion of the sound-speed functions around $\overline{\mathbf{x}}$ to better account for the difference in ray position:

$$c(\mathbf{x}) \approx c(\overline{\mathbf{x}}) + \nabla c(\overline{\mathbf{x}})(\mathbf{x} - \overline{\mathbf{x}}) \tag{3.35}$$

We can then apply such a first-order relation to the mean sound speed function and the DO modes function. This appears promising in that we have a representation of the $\mathbf{x} - \overline{\mathbf{x}}$ term: $\mathbf{x}_i \beta_i$. Hence, applying a first-order Taylor series expansion to both he sound-speed mean and the DO modes, our first-order stochastic approximation is:

$$c(\mathbf{x}) \approx \left(\overline{c}(\overline{\mathbf{x}}) + \nabla \overline{c}(\overline{\mathbf{x}}) \tilde{\mathbf{x}}_i \beta_i\right) + \left(\tilde{c}_j(\overline{\mathbf{x}}) \alpha_j + \nabla \tilde{c}_j(\overline{\mathbf{x}}) \alpha_j \tilde{\mathbf{x}}_i \beta_i\right) \tag{3.36}$$

This is the first-order stochastic approximation. Similar relations can be derived for the

other terms in the DO equations. Higher-order Taylor series can also be considered for additional accuracy in the stochastic space, but the computational costs of using such approximation quickly become large. In general, first-order and sometimes higher-order Taylor approximations have been very useful and efficient for stochastic DO energy-optimal and time-optimal path planning [84, 83, 82, 85, 87] as well as in stochastic biogeochemical modeling and inference [29]. We can expect that they would be also very useful for stochastic DO rays and this should be investigated.

Local sound-speed function. A third additional way to achieve the desired reduction to through other stochastic function approximation. However, it also results in a significant loss of generality and assumes knowledge of how the sound speed changes as a function of position on the ray as opposed to depth or position in the water column. Since the crux of the problem in evaluating the nonlinear $c(\mathbf{x}(s;\eta);\eta)$ is not knowing the analytical functional relationship and a simple (linear) representation, we could create an accurate but easy-to-deal with functional relationship with a stochastic dependency.

For instance, consider $\frac{dc(s)}{ds} = constant$, but assume the best approximation of the stochastic slope of the sound speed is to be determined ($m = \overline{m}+\alpha_j$). Instead of representing the stochastic sound-speed as $c(\mathbf{x};\eta) = \overline{c}(\mathbf{x}) + \tilde{c}_j(\mathbf{x})\alpha_j(\eta)$, we could represent it as:

$$c(\overline{\mathbf{x}} + \tilde{\mathbf{x}}_i\beta_i;\eta) = (\overline{m} + \alpha_j) * (\overline{\mathbf{x}} + \tilde{\mathbf{x}}_i\beta_i) + c_0 \tag{3.37}$$

Thus, considering the mean as an example,

$$\mathbb{E}^\eta[c(\mathbf{x}(s;\eta);\eta)] = \mathbb{E}^\eta[(\overline{m} + \alpha_j) * (\overline{\mathbf{x}} + \tilde{\mathbf{x}}_i\beta_i) + c_0] = \overline{m}\overline{\mathbf{x}} + \tilde{\mathbf{x}}\mathbb{E}^\eta[\alpha_j\beta_i] \tag{3.38}$$

The parameters in these equations could be optimized locally by least-squares or in the sense of variance as for the DO approximation. For equation (3.37), the result would remain a first-order approximation and be similar to the above first-order Taylor series approximation which was an expansion around the local range-dependent mean sound speed field.

Given an approximation for $c(s)$, we could extend this approach to any (higher-order) function that approximates $c(s)$ locally and incorporate a stochastic term. Legendre polynomials can be used to approximate functions for sound speed; however, the computational expense and complexity increase with the increase of the order of polynomials required to accurately represent the SSPs. All all these approaches are related to local polynomial chaos

expansion [70, 27], which can become very expensive if the order is increased and not so accurate if the stochastic fields to be approximated are dynamic and variable [70].

3.6.3 DO-Ray Computational Cost vs Monte Carlo

Consider a matrix form of our governing ODEs (3.3) and (3.4):

$$\frac{d\mathbf{X}_{r,d}}{ds} = \mathbf{C}. * \mathbf{\Xi}_{r,d} \tag{3.39}$$

and

$$\frac{d\mathbf{\Xi}_{r,d}}{ds} = \mathbf{C}_x. * \nabla_{r,d}\mathbf{C}\,. \tag{3.40}$$

For a paralleled Monte Carlo approach, the number of floating point operations (FLOPS) to compute the RHS of any of the range or depth component matrices is $R \times H$ FLOPS. This is the exact same number of FLOPS in computing the value inside the expectation of (3.25) and (3.26), with the added number of FLOPS to recombine the mean, DO modes, and DO coefficients. Without even considering the cost of (3.27) through (3.30), since our present DO implementation does not use the efficient approximation of Section 3.6.2, the implementation is less efficient than Monte Carlo. To understand why, we start with an ODE of a form where where a DO implementation offers computational savings.

Consider an ODE of the form:

$$\frac{d\mathbf{X}}{ds} = A\mathbf{X} \tag{3.41}$$

as opposed to using the hadamard product $(.*)$ as in our computations, with A being a $R \times R$ matrix. The number of FLOPS to compute the RHS of (3.41) is $RH(R-1)$. If we represented $\mathbf{X}$ in a reduced form the computation of $A\overline{\mathbf{x}}$ and $A\tilde{\mathbf{X}}$ are $2R^2 - R$ and $2R^2M - RM$ respectively. Therefore computational savings is achievable if we can represent $\mathbf{X}$ with less than $\frac{H-2}{2}$ modes.

This appears to be a moot point, but we still consider why we cannot represent (3.40)

and (3.41) in the form of (3.41). Consider $\mathbf{X}_r(s;\eta)$ consisting of R rays:

$$\begin{aligned} \frac{d\mathbf{X}_r}{ds} &= c(\mathbf{X})\boldsymbol{\Xi}_r; \\ c(\mathbf{X}) &= \begin{bmatrix} c_1(s) & & \\ & \ddots & \\ & & c_R(s) \end{bmatrix} \end{aligned} \tag{3.42}$$

In this case we could modify the equation to remove the hadamard product making $c(\mathbf{x})$ a diagonal matrix with the rays sound speed at step s along the diagonal for each ray. Observing the ODEs in this form illustrates why our present implementation will fail to provide computational savings, the computations do not rely on mutual information between rays.

Our use of a characteristic or Lagrangian approach when we discretized the wave-front to discrete rays traveling perpendicular to the wave, our derivation removed any correlation in space between the rays. Since each ray is computed independently without concern for its neighbors, we cannot hope to achieve computational savings with the DO-Ray equations as implemented.

Based on the preceding paragraphs, it follows to ask, "Why is a DO-Ray approach is worth implementing?" Though in deriving the equations that would govern ray trajectories we removed the opportunity to capture ray inter-dependencies, that does not mean they are no longer present. As each ocean SSP will govern how a group of rays evolves, a Lagrangian approach allows us to see how the energy propagates with a certain number of rays to represent the field. We should be able to capture the majority of the information about our wave front with a reduced representation of the rays as shown shown in our feasibility section. First, we could use the reductions discussed in Section (3.6.2). Second, we could utilize the wave-front information itself. We will indeed show that a low rank representation of the discretized wavefront can be marched in the ray domain ("s") and produce accurate representations of the stochastic field, even if more expensive in our present implementation. With this being possible, if we implement a DO wavefront or a modified DO-Ray scheme using Section (3.6.2), we could use reduce the computational cost below that of Monte-Carlo. We discuss these opportunities in Chapter 5.

3.6.4 Specific Stochastic DO-Ray Implementation

We now outline the specifics of how we implemented the stochastic DO-Ray equations. This outline will also further crystallize the above computational discussion. Since ultimately DO-Ray is compared to a Monte-Carlo implementation of the deterministic model, we list both.

To implement a Monte-Carlo computation of a determinisitc model with uncertain initial conditions, we assume that each ray is computed independently. The computation for all rays in all ocean realizations can then be computed in parallel through following Algorithm:

- Create initial state matrices $\mathbf{X}$ and $\mathbf{\Xi}$.
- Compute (or table look-up) $c(s)$ and $\nabla c(s)$ for all rays in all realizations.
- For s = 1:$\frac{RayLength}{\Delta s}$
  - Integrate the system of ODEs (Finite Difference or Runge-Kutta) to evolve $\mathbf{X}(s)$ and $\mathbf{\Xi}(s)$ to $\mathbf{X}(s+1)$ and $\mathbf{\Xi}(s+1)$.
  - Identify reflections and modify $\mathbf{X}$ and $\mathbf{\Xi}$ accordingly.
  - Compute (or table look-up) $c(s+1)$ and $\nabla c(s+1)$ for all rays in all realizations at the new $\mathbf{X}(s+1)$.
- End.

Our present DO-Ray implementation for the stochastic reduced-order model computes all rays and realizations in parallel, but requires additional steps as outlined below:

- Perform Monte Carlo runs and create initial state matrices $\mathbf{X}$ and $\mathbf{\Xi}$ and compute the reduced order representations: mean, DO modes, and DO coefficients.
- Compute (or table look-up) $c(s)$ and $\nabla c(s)$ for all rays in all realizations.
- For s = 1:$\frac{RayLength}{\Delta s}$
  - Integrate the system of ODEs (Finite Difference or Runge-Kutta) to evolve mean, DO modes, and DO coefficients, separately.
  - Adjust DO modes and coefficients to ensure orthonormal basis is maintained.
  - Identify reflections and modify DO modes, and DO coefficients.

• Compute (or table look-up) $c(s+1)$ and $\nabla c(s+1)$ for all rays in all realizations at the new $\mathbf{X}(s+1)$.

- End.

While both algorithms have the same basic integration steps, there are several differences. We will describe these below; however, it is important to point out that our present algorithm will not be computationally efficient as compared to a Monte Carlo implementation. Since it has additional computational steps, such as evolving three ODE's instead of two, we are increasing the computational expense. We would have to gain efficiency using the reduced order nature of the DO ray field. Later in this chapter we will explore how we may improve the computational efficiency our implementation; however, we leave this for future work.

3.7 Stochastic DO-Ray Computational Schemes

3.7.1 Initialization

Consider a field of ray traces where the SSPs are stochastic random varaables, but the source is at the same range and depth. Since the ray trajectories are identical at the start, with a small variation in the sound speed after a 1 m step, there is very little variation in the field of ray traces such that the entire field can be represented by its mean. Hence the linear combinations of the DO modes and coefficients are at or very near zero. Because of this, we can perform Monte-Carlo computations for each of the realizations to "initialize" the field.

In order to initialize the evolution equations (3.17) through (3.21), we compute an ensemble of deterministic ray traces for each of the sound-speed profiles sampled from a distribution. The range, or number of steps for which each of these must be computed is determined by the variation in the sound-speed profile distributions, but can be generally stated that we should march far enough to establish individual correspondence between the individual SSPs and their associated ray traces [83, 4].

Once we have computed the subsequent ensemble of ray-traces, we can compute our initial mean, DO modes, and DO coefficients of the stochastic field. We compute the initial conditions for the modes and stochastic coefficients at step "s" through the singular value decomposition (SVD) of the ensemble of realizations. Upon establishing these initial conditions, the evolution equations are then computed using the preferred direct integration

scheme (Finite Difference, Runge-Kutta, etc.). When properly initialized, the correspondence for each sound-speed profile to its associated ray trace will be maintained throughout the evolution of the DO-Ray equations.

3.7.2 Re-Orthonormalization

Earlier in this chapter, we analytically derived the DO-Ray equations. A key to that derivation was that we satisfy the DO condition and that the modes of our stated variables form an orthonormal basis. While this is true for an analytical solution, once we implement the numerical solution (e.g. using Finite Differences), after our first time step, the modes will no longer be orthonormal due to numerical errors [97]. Thus, we require an efficient way to correct the numerical modes such that they are numerically orthonormal to each other, while they remain close to their predicted orientation in the stochastic subspace and the realizations are closely maintained. In matrix form, let $\mathbf{U}$ be a matrix containing the computed modes at a given range-step. We desire a matrix $\mathbf{A}$ such that:

$$\tilde{\mathbf{U}} = \mathbf{U}\mathbf{A} \tag{3.43}$$

where $\mathbf{A}$ is as close to the identity matrix as possible. For an in-depth derivation and analysis of the method used, we direct the reader to [55, 96, 88].

We start with the Gram matrix of the evolved DO modes, $\mathbf{K}$. Since the modes should be orthonormal the numerical errors induced can be expressed as $(\mathbf{K} - \mathbf{I})$, where $\mathbf{I}$ is the identity matrix, and $(\mathbf{K}-\mathbf{I})$ is very "small" in terms of its Frobenius norm. We assume that there exists a matrix $\mathbf{A}$ also close to $\mathbf{I}$ such that $\mathbf{A}^T\mathbf{K}\mathbf{A} = \mathbf{I}$. Since $\mathbf{I}$ is symmetric positive definite, we restrict this closest $\mathbf{A}$ to be also symmetric positive definite and come to the following [55]:

$$\mathbf{A} = \mathbf{V}\mathbf{\Sigma}^{-1/2}\mathbf{V}^T = \mathbf{K}^{-1/2} \tag{3.44}$$

Using this information, we construct a simple algorithm to obtain $\mathbf{A}$:

- Compute Gram matrix, $\mathbf{K}$ of the DO modes
- Perform Eigen Decomposition to obtain $\mathbf{V}\mathbf{\Sigma}\mathbf{V}^T$
- Compute $\mathbf{A}$, $\mathbf{A} = \mathbf{V}\mathbf{\Sigma}^{-1/2}\mathbf{V}^T$

While this algorithm will re-establish the orthonormal basis of our stochastic subspace, because we altered the DO modes, we must also perform a similar update to the DO coefficients in order to preserve accurate physical realizations. Let the superscript "*" denote the post-reorthonormalization matrices. Let the matrix $\mathbf{Z}$ perform a similar function for the stochastic coefficents as $\mathbf{A}$ did for the modes, but instead ensures that realizations are preserved: $\mathbf{B}^* = \mathbf{BZ}$ and $\tilde{\mathbf{X}}\mathbf{B}^T = \tilde{\mathbf{X}}^*\mathbf{B}^{*T}$. Hence, we have:

$$\begin{aligned} \tilde{\mathbf{X}}^* &= \tilde{\mathbf{X}}\mathbf{A}; \mathbf{B}^* = \mathbf{BZ} \\ \tilde{\mathbf{X}}\mathbf{B} &= \tilde{\mathbf{X}}^*\mathbf{B}^* = \tilde{\mathbf{X}}\mathbf{A}\mathbf{Z}^T\mathbf{B}^T \\ \mathbf{Z} &= \mathbf{A}^{-T} \end{aligned} \tag{3.45}$$

3.7.3 Surface and Bottom Reflections

Because we are operating in a ray domain, our boundary conditions, specifically the ocean surface and bottom cannot be incorporated into the solver of our system of differential equations. This also needs to be addressed in the Monte-Carlo and DO-Ray approaches. Earlier in this chapter, we covered two implementations for the deterministic implementations. We now cover ways to implement them both in the DO-Ray approach and the potential drawbacks for each.

Singular Value Decomposition Recompute for Hard Implementation

Consider 10^4 ocean realizations, with each ocean realization consisting of ray traces of 10 rays. To evaluate whether a ray has interfaced, we have to evaluate every ray position in every realization and check if the ray has reached the interface. We would then compute the reflected ray paths according to (3.12). In the deterministic implementation, we are set to continue marching along in the new ray direction. Because of the reduced order of the DO-Ray methodology, changing one ray direction is not a trivial matter. There is no simple correspondence to altering a one or more ray's parameters in the fields $\mathbf{X}$ and $\mathbf{\Xi}$ and the alteration to the DO Modes and DO coefficients. Therefore, should this occur to continue to evolve the mean, DO modes, and DO coefficients, we must recompute a truncated SVD of the fields $\mathbf{X}$ and $\mathbf{\Xi}$ adding significant computational expense to this step.

With only a few rays, this additional SVD computation may only be required on relatively few number of steps making the added computational expense manageable. In the case of

10^4 rays, a bundle of rays are likely to interface a boundary at every step over an long interval of steps increasing computational costs.

Singular Value Decomposition Rank-1 Update for Hard Implementation

While there is no simple correspondence between altering one or more ray parameters in the fields $\mathbf{X}$ and $\mathbf{\Xi}$, and altering the DO Modes and DO coefficients, there have been advances in approximating how the SVD matrices are altered when performing updates to individual parameters of the reconstructed matrices.

For example, [11] explains in detail how we may approximate the updates to the SVD matrices $\mathbf{U}$, $\mathbf{\Sigma}$, and $\mathbf{V}$, and how significant computational expense be mitigated in the event of low-rank updates, specifically rank-1 updates. Here we will present the methodology and direct the reader to [11] for a more detailed explanation.

For the stochastic field matrix $\mathbf{X}^* = \mathbf{X} - \overline{\mathbf{x}}$, we aim to evolve the SVD ($\mathbf{U}$, $\mathbf{\Sigma}$, and $\mathbf{V}$) and thus evolve the stochastic fields using the DO-Ray differential equations. Now, if we alter one component in $\mathbf{X}$, we can represent the alteration as the multiplication of two vectors $\mathbf{a}$ and $\mathbf{b}$ as follows:

$$\mathbf{X} + \mathbf{a}\mathbf{b}^T = \mathbf{U}'\mathbf{\Sigma}'\mathbf{V}'^T . \tag{3.46}$$

$\mathbf{U}'\mathbf{\Sigma}'\mathbf{V}'^T$ are computed my making use of a modified Gram-Schmidt algorithm and the diagonalization of a $(rank(\mathbf{X}^*)+1)$ by $(rank(\mathbf{X}^*)+1)$ matrix. While this shows significant savings over the full SVD computations, there are several drawbacks to using this method in the present DO-Ray implementation. First, this rank-1 update is more efficient than a full SVD; however to recompute the DO modes and coefficients, we perform a truncated SVD, and therefore may not result in computational savings. Second, the significant computational savings is achieved for rank one updates. If reflections occurred in multiple realization, the update would have to occur in series for each reflection also adding computational cost. Lastly, just as with the previous section, this method is inefficient where a bundle of rays are likely to interface a boundary at every step over an interval of steps. For these reasons, in general cases, the rank-1 update implementation will not show noticeable improvement over recomputing the SVD for our applications.

Reflecting SSPs

When confronted with reflections in the DO-Ray methodology, the ideal situations would be to only consider cases where rays will not interface with the boundary (e.g. deep sound channel propagation). With this in mind, by reflecting the sound speed profile functions over the surface and bottom boundaries, thus defining sound-speed functions at negative depths and depths greater than the ocean bottom, we allow the DO-Ray computation to continue into the reflected domains, where we can reflect the rays back into the actual ocean domain as a post processing step. This removes the computational cost of evaluating for interactions and the need to compute truncated SVDs as the rays propagate. The obvious drawback to this method is that we are restricted to flat-surface and bottom interactions removing any range dependent bathymetry. Still, due to the gained efficiency and non-algorithm intrusive nature of this method, we choose reflecting SSPs as our boundary reflection implementation method in Chapter 4 demonstrations.

Chapter 4

Test Cases and Stochastic DO-Ray Implementation Results

In this chapter we implement and evaluate the DO-Ray algorithm as outlined in Chapter 3. We present three scenarios of stochastic ocean states (varied SSPs), and compute ray traces for all oceans using both Monte Carlo and DO-Ray implementations. Using these scenarios, our aim is to understand how the reduced representation of the Rays affect the accuracy of the stochastic computation. To assess accuracy we can first look at how the reduced order method explicitly alters the specific ray paths, similar to how we assessed the accuracy in Chapter 3. We also observe how the accuracy converges with respect to the step size and the number of DO-modes used in the computation.

We start with a manufactured distribution to assess DO-Ray in an idealized (i.e. propagation patterns are easily verified), non-Gaussian scenario. We then look at two realistic scenarios for the stochastic ocean acoustic environment with assumed Gaussian distributions. While we aim to assess the feasibility of a reduced order representation of a wave-front, discretized as rays, a practical application would be to use these calculations to infer the correct realization or ocean environment in a Matched-Field Processing or Bayesian Learning algorithm with a measurement of a signal parameter (e.g. TL or travel time). Hence, DO-Ray's ability to accurately capture the variability in a ray trace is the ultimate assessment of its feasibility. With this in mind, for all cases the acoustic source is located at a point of relatively high variability. Of course, the sound signal is assumed to satisfy the high frequency approximation for Ray Methods.

4.1 Constant Gradient Sound Speed Profile Distribution

In Chapter 3, constant gradient SSPs were useful in validating the results of our deterministic implementation due to the ability to compare it to an analytical solution. The constant negative gradient SSPs are idealized as they are typically not observed in nature over an entire column of deep water (+2000m). As a test case they are useful because the physics are easily understood and validated. There are real ocean environments that have a relatively constant positive sound speed gradient. Referring back to (1.1), we know that the sound speed of the ocean is dependent on three factors: Temperature, Pressure, and Salinity. In the polar regions, the water column temperature and salinity can be considered almost uniform at all depths [65]. Under these conditions, sound-speed varies only according to pressure (depth) resulting in a constant, positive, sound-speed gradient. In shallow water at mid-latitudes, the sun heats the surface resulting in warmer water near the surface and gradually getting cooler at deeper depths, the resultant sound speed profile would have a negative gradient. This negative gradient is less likely in deep water as eventually the effect of the sun's warming would be overtaken by the ocean depth transitioning to a positive gradient at deeper depths.

To illustrate the feasibility of a reduced representation of the stochastic ray trace fields produced by constant gradient profiles, we combine constant negative and constant positive gradient distributions in order to sample from a non-Gaussian distribution of SSPs. The combinations of these idealized sound speed distributions in a 2000m depth ocean allows us to observe DO-Ray performance when considering stochastic ray traces that have fundamentally different characteristics.

In Figure 4-1, we show our SSP probability density function (pdf) and 100 randomly sampled SSPs. We computed deterministic ray traces using the mean SSP and SSPs located near the edges of the pdf. We display the example SSPs and associated ray traces in Figure 4-2. We easily observe variability in the ray propagation as the rays corresponding to a negative sound speed gradient tend to bend toward the ocean floor, while the opposite occurs with the positive sound-speed gradient realization. In Figure 4-3 we can see the variation according to the initial launch angle at a specified Ray length, 10^4 m. Due to the reflections and refraction within the wave-guide we see a large variability with identical ray launch angles varying as much as 300m and also merging to nearly identical locations.

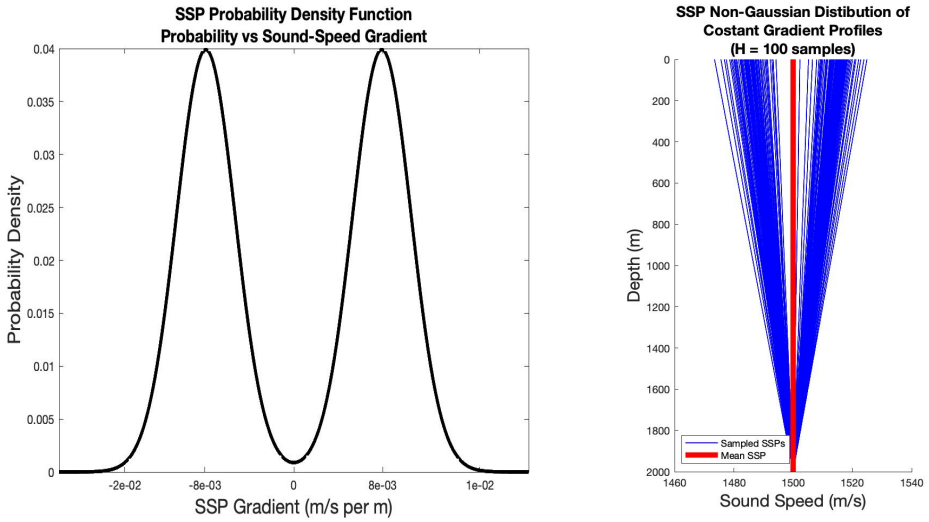

(a) PDF (b) SSPs

Figure 4-1: (a) We combine two separate normal distributions with means at ±8e-3 respectively into a non-Gaussian distribution (b) From this distribution, we can sample SSPs of different sound-Speed Gradients

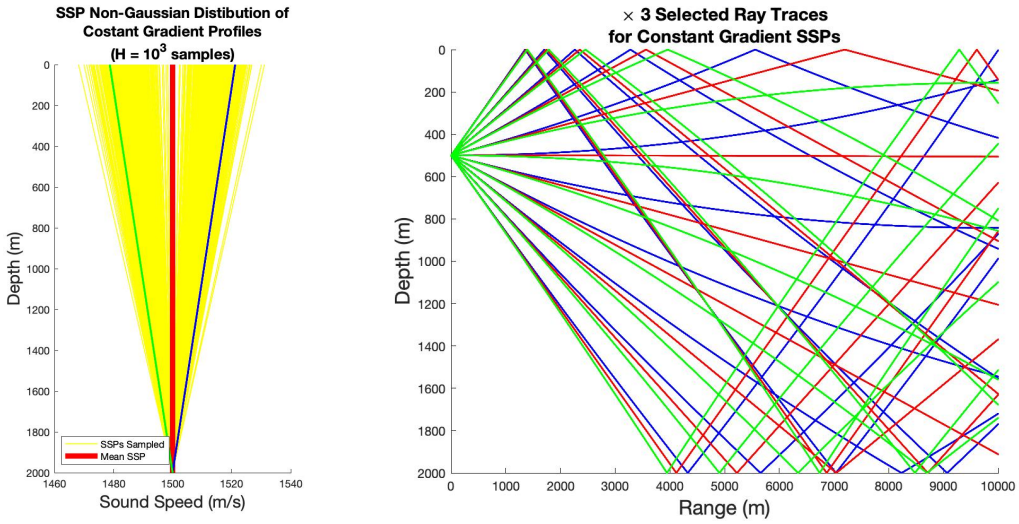

(a) (b)

Figure 4-2: (a) From our constant-Gradient SSP distribution, we sample 1000 SSPs. (b) We computed the associated ray traces for the highlighted red (mean), green and blue SSPs. Ray traces computed using 11 rays at evenly spaced angles between ±20°, 2nd-order Runge-Kutta with a 1m step-size.

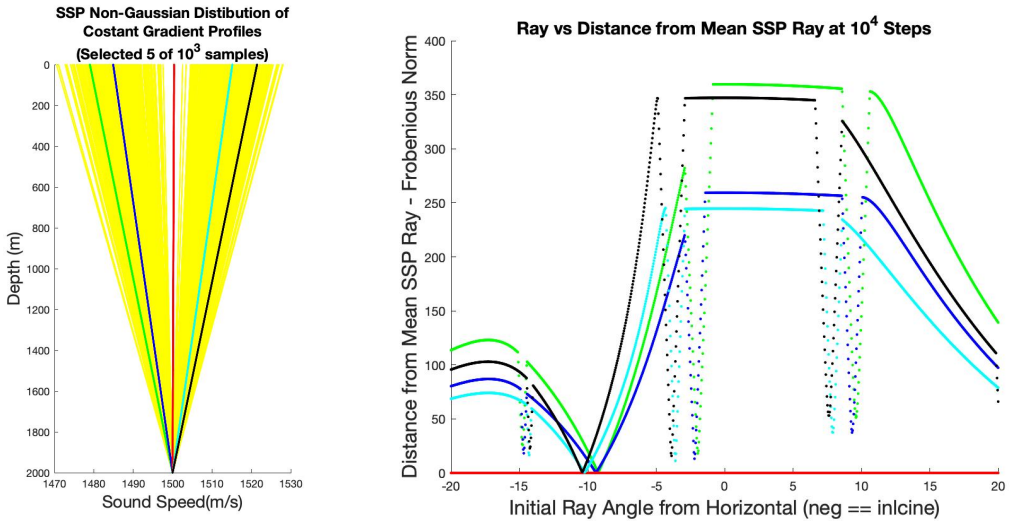

(a) (b)

Figure 4-3: (a) From our constant-Gradient SSP distribution, we sample 1000 SSPs. We computed the associated ray traces for the highlighted SSPs. (b) Plot shows the variability in the different SSPs according to each ray path. Due to the variability in SSPs, we observe the rays starting with the same initial conditions vary up to hundreds of meters after 10^4 steps. Some differences are near zero due to rays crossing similar spaces in the Cartesian plane however it is easily observed in Figure 4-2 that the rays are on different trajectories. Traces computed using our deterministic model with 1001 rays at evenly spaced angles between $\pm 20°$, 2nd-order Runge-Kutta with a 1m step-size.

4.1.1 DO-Ray Accuracy as Compared to Monte Carlo

Using the intuition gained from feasibility analysis done in Chapter 3, we sampled 1000 oceans from our constant-gradient distribution of SSPs and computed the associated ray traces with 1001 Rays. We make a realization-to-realization comparison of the Monte-Carlo and reduced-order DO-Ray computations to assess the accuracy of the ray positions after range marching to 10^4 m with a 1 m step-size.

Capturing the Stochastic non-Gaussian Variability

To assess DO-Ray's accuracy in capturing the variability of the environment, we first produce an assessment of how variable the environment is with respect to ray positions. How much does a ray, starting with the same initial condition, vary with the selected SSP. Figure 4-3 shows how the individual ray positions vary as compared to the position of the mean SSP. Some rays converge to nearly the same position as the rays cross the same point in the Cartesian plane due to reflection and refraction. Still with our SSP distribution, we see that after 10^4 steps to 10^4 m, the majority of the individual rays will vary a few hundred meters as compared to the mean SSP.

After computing the ray trace ensemble with DO-Ray, we compare the specified realizations within the ensemble to the deterministic implementation, a realization-to-realization comparison. We refer to Figure 4-4 for a qualitative representation of the accuracy of the DO-Ray implementation. The ray traces are nearly indiscernible as the DO-Ray overlays the deterministic solutions for all of the selected ocean SSPs.

Figure 4-5(a) gives us the error for each ray in the selected SSP environment. The subsequent figures contrast the selected SSPs for a specific number of DO modes used in the DO-Ray computations. We can make two important assessments. First looking at the vertical axis, we see that though the environments vary significantly, the error in the DO-ray computation is relatively small. More significant in these plots is the extent to which the computation captures the environment based on the SSPs likelihood in the probability density function. We observe the mean SSP as well as those on the edges of SSP pdf contain higher peak errors and overall more error as compared to the SSPs selected from near the local maximums of our pdf.

Figure 4-6 evaluates the effects of varying the number of DO modes within the particular

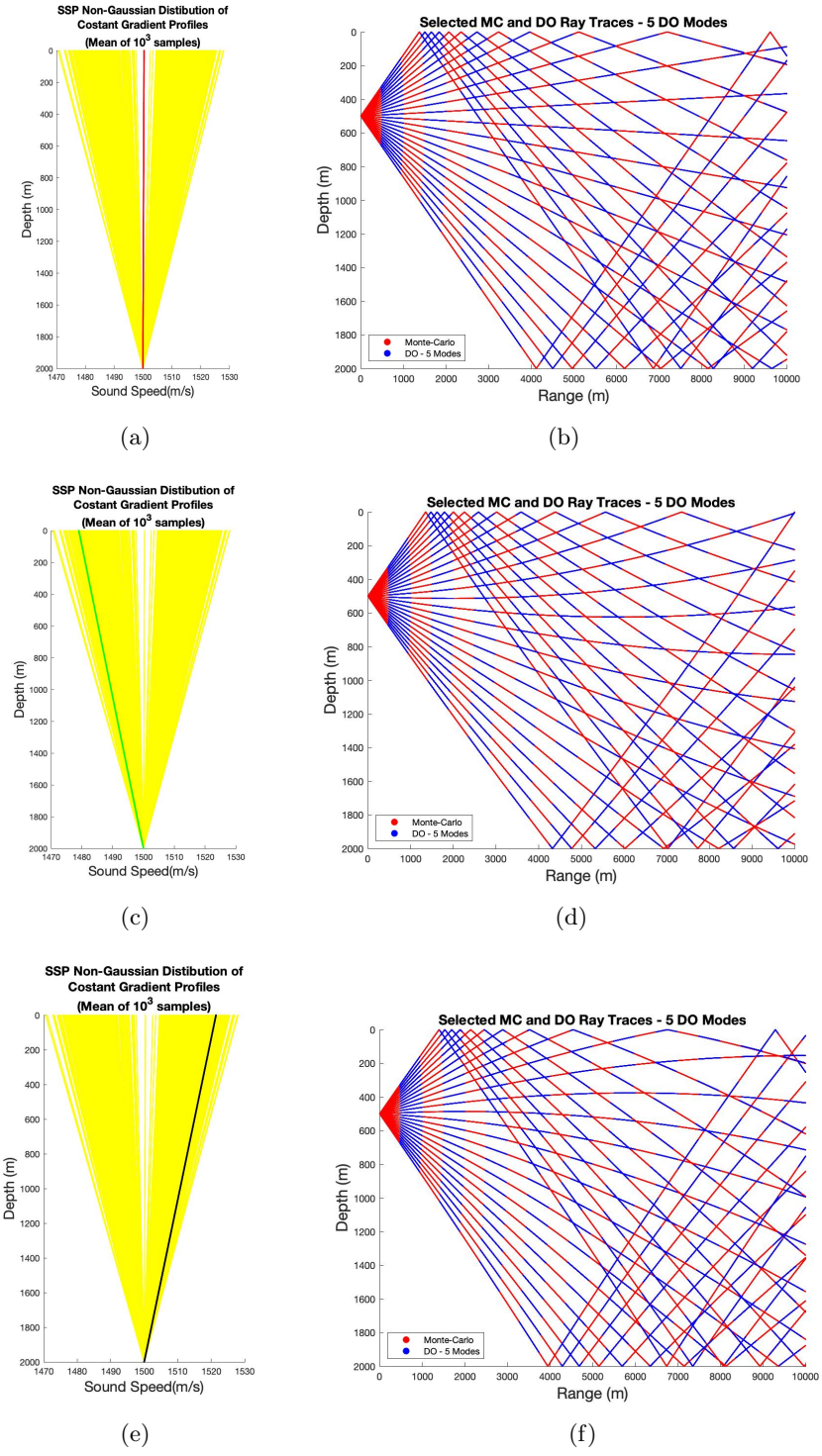

Figure 4-4: Panels (a), (c), and (e) Computed ray traces for highlighted SSPs. Panels (b), (d), and (f) show the DO-Ray Computed Ray Trace (5 DO modes) overlaid with deterministic (Monte Carlo) traces. All traces computed using with 1001 Rays (26 Plotted) evenly at evenly spaced angles between $\pm 20°$ with a 1m step-size. The deterministic model uses 1st-order Forward Difference.

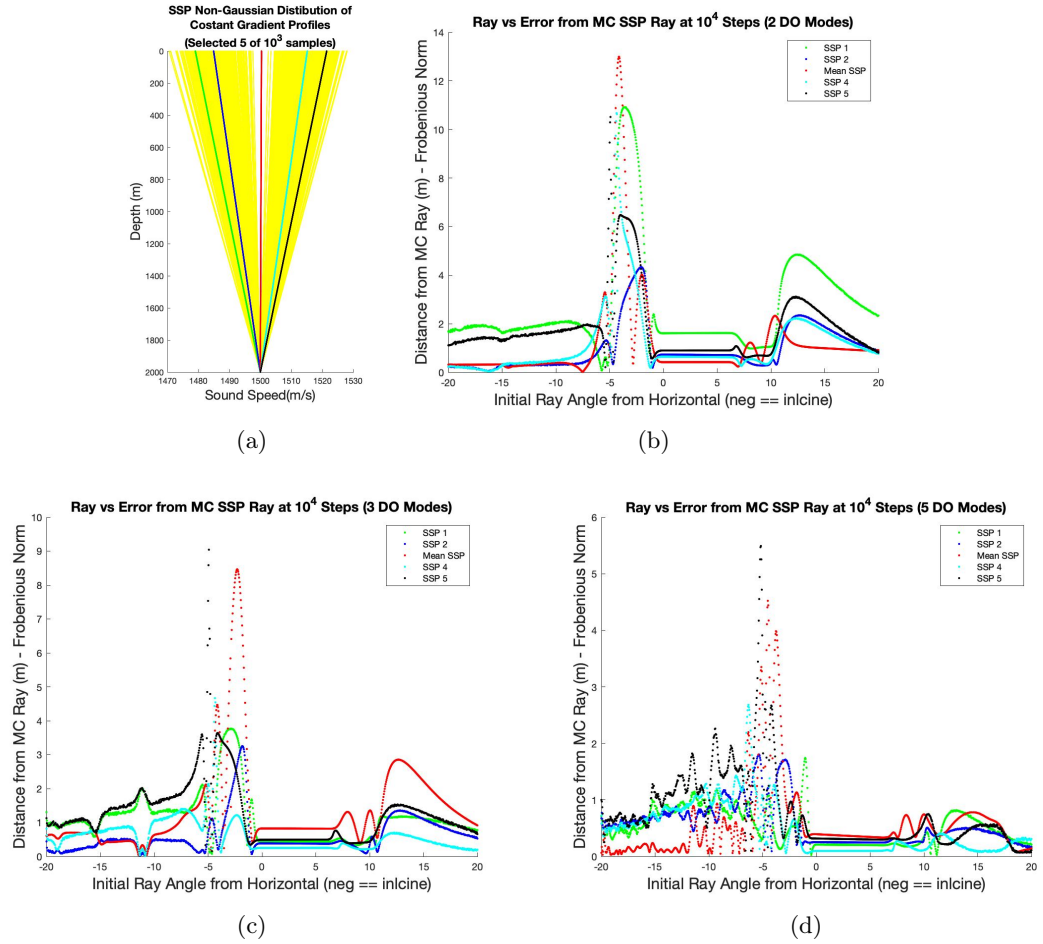

Figure 4-5: (a) Computed ray traces for highlighted SSPs. Panels (b) through (d) show the associated error as compared to the Monte Carlo solution using the specified number of modes. We observe that the DO-Ray methodology error is a very small fraction of the variability in the rays. We also observe that, generally, the methodology is better at capturing the variability in the SSPs of higher probability of occurrence (green and blue). Traces computed with 1001 rays evenly at evenly spaced angles between $\pm 20°$, 1st-order Forward Difference with a 1m step-size.

realizations. Again we can see that the peak error is reduced as we increase the number of modes.

Based on these two figures we know that the majority of the information contained in the wave-front field, can be captured using less than five of the 2002 DO-modes and maintain the accuracy of the individual rays to more than an order of magnitude less than the variability in the field. To make a better assessment of this, we can look at the convergence of the average error among the rays with the number of DO modes used in the computation.

Convergence with Number of DO Modes

When assessing the feasibility of a reduced-rank representation of the ray trace field, we observed through the singular values how many DO modes may be required to capture the majority of the information at every step. With stochastic DO-Ray predictions, we computed the ray traces by evolving the reduced-rank stochastic fields with different numbers of DO modes. In Figure 4-7 we illustrate how the error converges with the number of DO Modes used. For the mean profile we observe a 1st order convergence with the number of modes. The SSPs selected near the edges of the SSP pdf converge with less than first order convergence after the initial 10 DO Modes. Of note we observe that with less than 10 modes we are able to get an average accuracy less than 1 m for these realizations indicating that error due to numerical errors dominates the error associated with fewer modes.

Convergence with Step Size

For the DO-Ray computations, we implemented a first-order Finite Difference (Forward Difference) scheme and make realization to realization comparisons to our deterministic computations using second-order Runge-Kutta scheme with a step-size of 10^{-2}m. We plotted the results in Figure 4-8.

Here again, for our mean profile we observe the expected first-order convergence. For the profiles on the outer edges of SSP pdf we see a first order convergence, that decays as error is less than 1 m where the numerical errors are more significant than the errors due to step size.

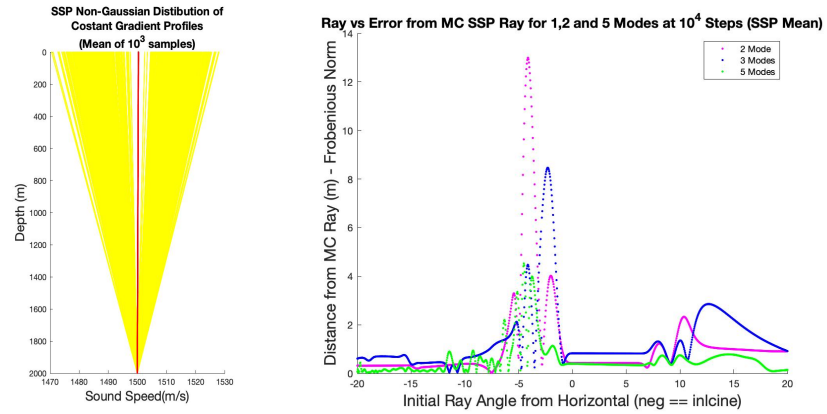

(a) (b)

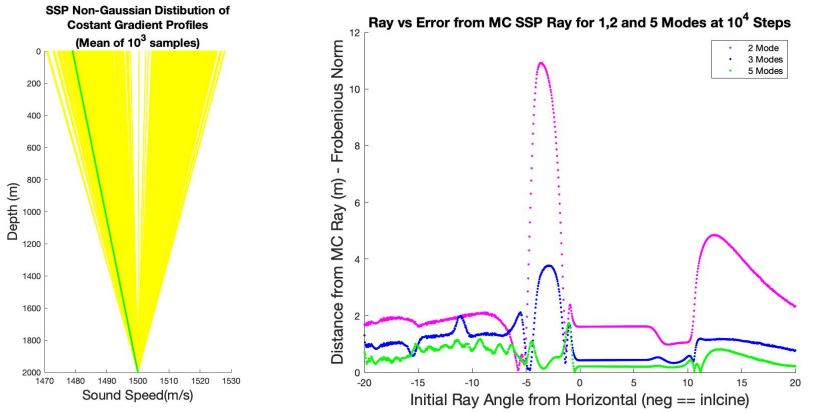

(c) (d)

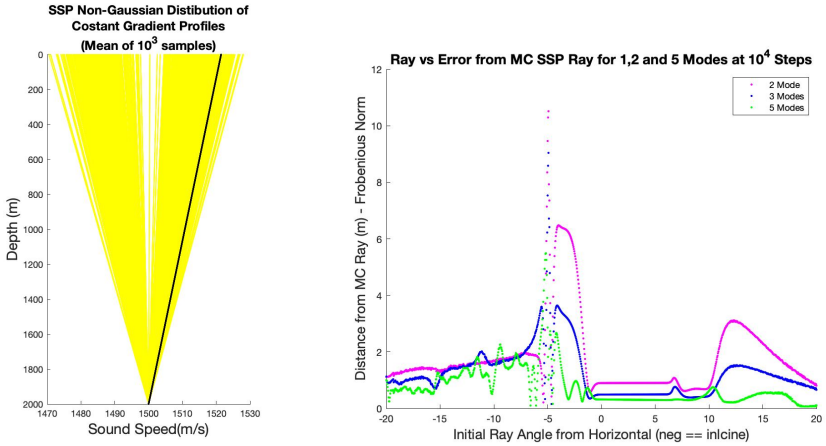

(e) (f)

Figure 4-6: Panels (a), (c), and (e) Computed ray traces for highlight SSPs. Panels (b), (d), and (f) show the associated error as compared to the Monte Carlo solution for a particular realization when using 2, 3, or 5 modes. Note errors in a realization and the trend as we increase the number of modes. For a particular realization the error approaches the deterministic solution. Ray traces computed 1001 rays at evenly spaced angles between $\pm 20°$, 1st-order Forward Difference with a 1m step-size.

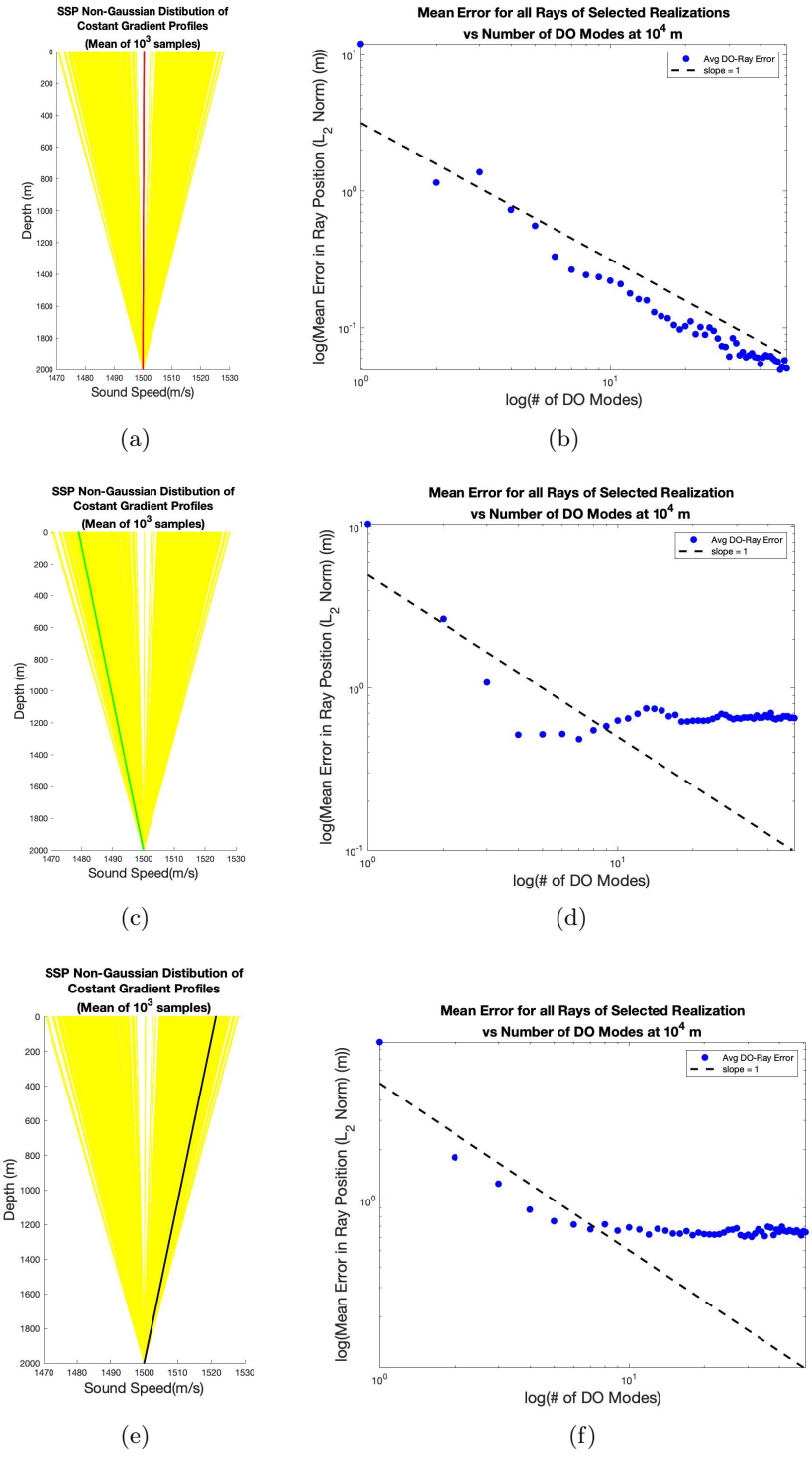

Figure 4-7: Panels (a), (c), and (e) Computed ray trace ensembles for highlighted SSPs with a varying number of DO modes. Panels (b), (d), and (e) show the convergence for selected realizations of the DO-Ray Methodology with the deterministic solution. 1st-Order convergence line plotted for reference. Deterministic traces computed using our deterministic model with 1001 rays evenly at evenly spaced angles between $\pm 20°$, 1st-order Forward Difference with a 1m step-size.

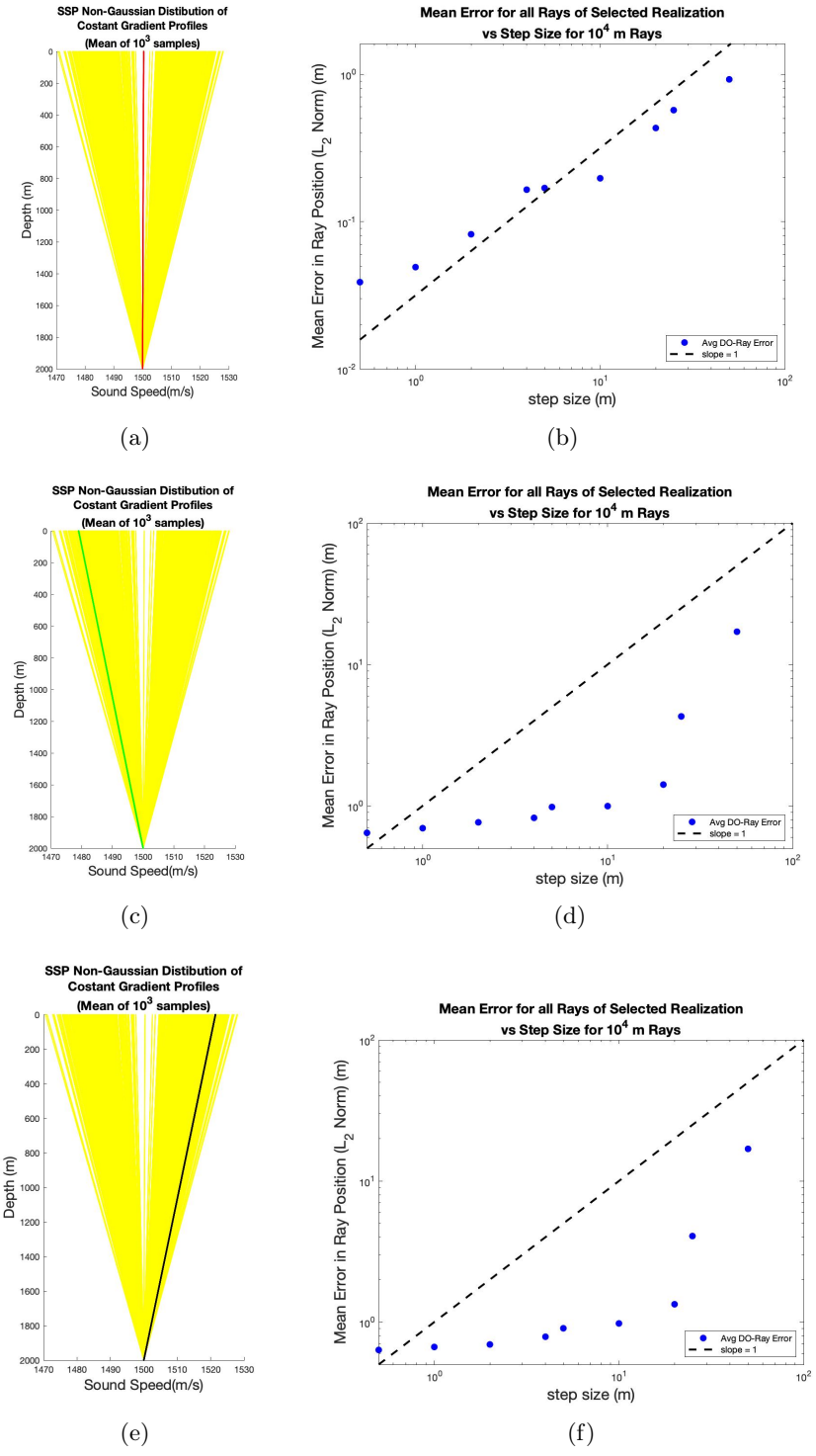

Figure 4-8: Panels (a), (c), and (e) Computed ray trace ensembles for highlighted SSPs with a varying step-size. Panels (b), (d), and (e) show the convergence for selected realizations of the DO-Ray Methodology with the deterministic solution. 1st-Order convergence line plotted for reference. DO-Ray computations used 10 DO modes. Deterministic traces computed using our deterministic model with 1001 rays evenly at evenly spaced angles between $\pm 20°$, second-order Runge-Kutta 0.01m step-size.

4.2 Deep Sound Channel Sound Speed Profile Distributions

Sound fixing and ranging (SOFAR) or deep sound channels (DSCs) are the result of specific ocean sound speed characteristics, principally a negative over a positive sound speed profile [65, 37]. Primarily observed in the mid-latitudes, having a minimum sound speed at deeper depths results in a condition where sound propagates in a duct, not interacting with the surface or bottom, making the only means of attenuation the absorption in the seawater [23]. In a deep sound channel, the acoustic energy of a source can be detected at ranges of several tens to hundreds of kilometers.

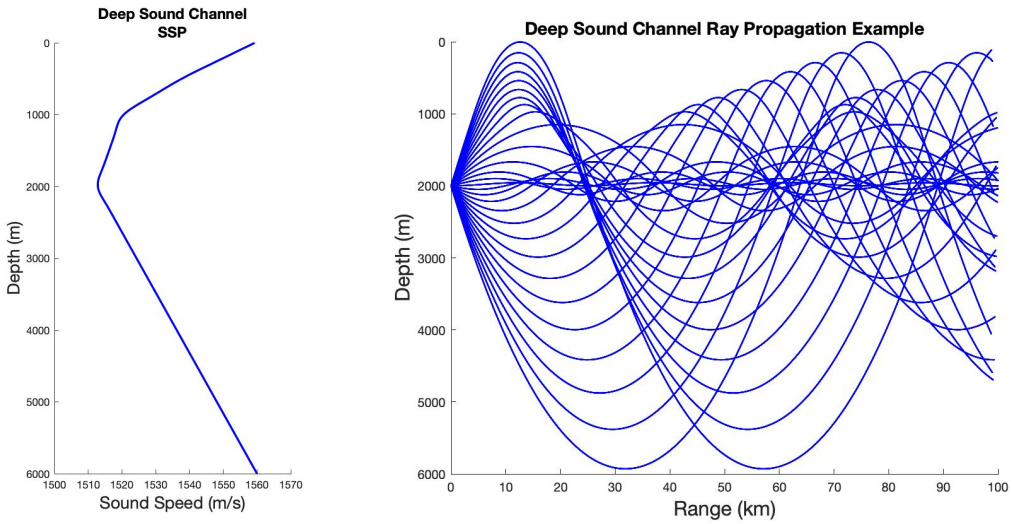

(a) SSP

(b) Ray Trace

Figure 4-9: Example of acoustic rays propagating in a deep sound channel with the acoustic source located at the deep sound channel axis (depth of minimum sound speed). Ray traces computed using 29 Rays evenly at evenly spaced angles between $\pm 14°$, 2nd-order Runge-Kutta with a 1m step-size.

Consider a situation where the state of an upper column is highly variable due to abnormal weather events or abnormal seasonal variation. For underwater communication, detection and localization, it is of tactical significance to determine whether DSC propagation exists. A simple way of examining the existence and extent of the SOFAR channel would be to measure sound intensities at the ranges where we would expect the energy to focus. Here we consider that we have the means to measure signals produced only from about 10 km distances.

In this scenario, we characterize the uncertainty as a Gaussian distribution of sound speed at the ocean surface, with sound-speed characteristics becoming more similar as depth

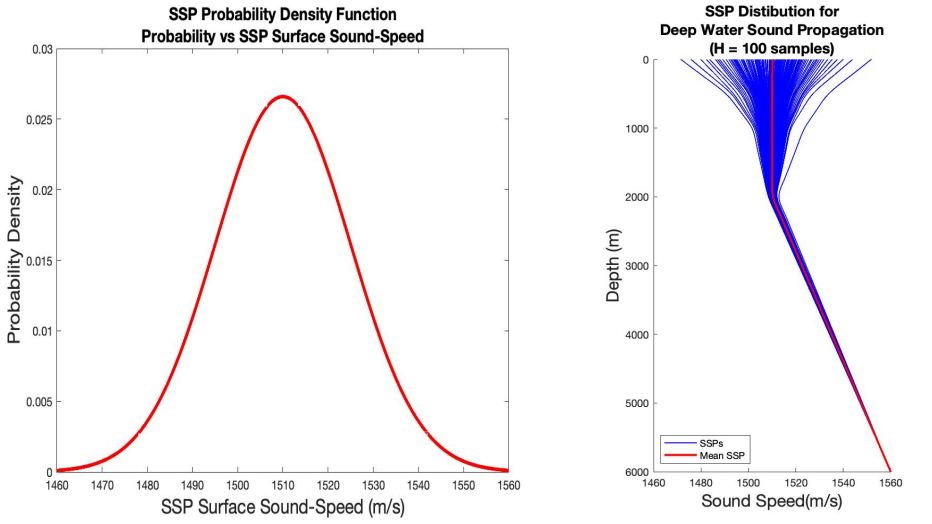

(a) (b)

Figure 4-10: From normal distribution of SSPs characterized by the surface sound-speed with a mean at 1500m/s (a) from which we can sample to obtain SSP realizations (b).

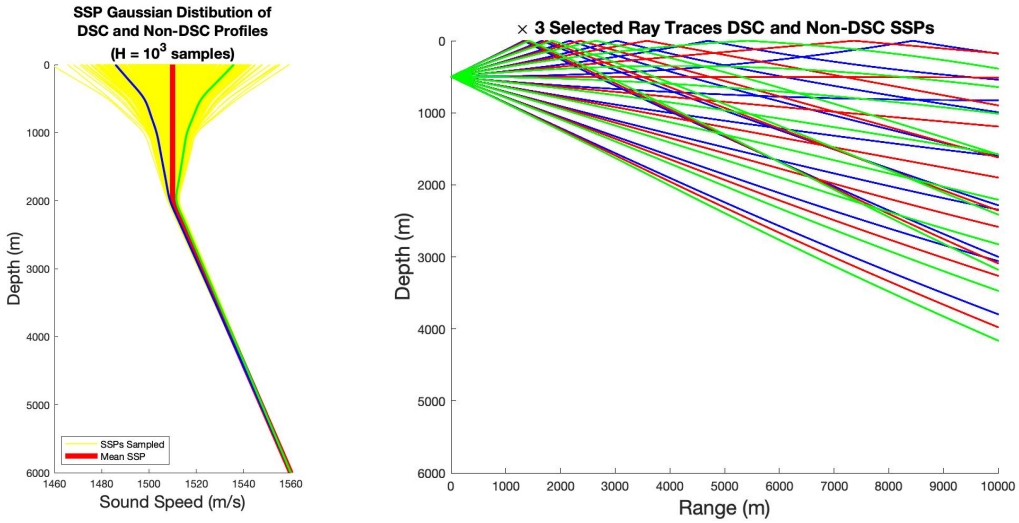

(a) SSP (b) Ray Trace

Figure 4-11: (a) From our SSP distribution, we sample 1000 SSPs. (b) We computed the associated ray traces for the highlighted red (mean), green and blue SSPs. Only the green SSP environment of the three would result in a DSC. Ray traces computed using 11 Rays evenly at evenly spaced angles between $\pm 20°$, 2nd-order Runge-Kutta with a 1m step-size.

increase (i.e. the SSP at deeper depths is unperturbed by surface events). In Figures 4-9 and 4-10, we show our sample distribution as well as computed ray traces for the mean SSP and two profiles closer to the edges of our Gaussian pdf. Only the SSP highlighted in green would result in a DSC propagation environment where with the other two, over long distances the sound is refracted back to the surface. The variability in the ray propagation is still observed at shorter ranges, hence a measurement at this range could confirm the existence or non-existence of a DSC.

Capturing the Stochastic non-Gaussian Variability

Using the same computational schemes as those used for the Constant gradient SSPs, we computed ray trace ensembles with the stochastic DO-Ray equations and algorithm, then computed specified realizations within the ensemble using a deterministic implementation for comparison. Figure 4-12 provides a qualitative representation of the accuracy of the DO-Ray implementation. Again the ray traces are nearly indiscernible at this range scale as the DO-Ray overlays the deterministic solutions for all of the selected ocean SSPs.

Convergence with Number of DO Modes

For this distribution of SSPs the variability in ray paths result in positions $\sim$1000 m apart, still with relatively few modes, we are able to recreate realizations within $1-10$ m accuracy. In Figure 4-13, we showcase the first order convergence up to about 200 of the available 2002 DO modes where the numerical errors begin to dominate the error.

4.3 Variable Sonic Layer Depth - Sound Speed Profile Distributions

For our final test case we consider a situation where the overall shape of the SSP is known; however, a key characteristic is uncertain. In the mid-latitudes (tropical and sub-tropical) the sound speed profiles can be sub-characterized into three layers [16, 37, 23]. The top layer (surface to a near surface depth of maximum sounds speed), has a nearly uniform temperature profile, where the variation in depth is a consequence of atmospheric events. Due these effects at the ocean surface, the sound-speed values down to depths of 500m may be affected. This layer is known as the sonic layer. We refer to the next layer as the

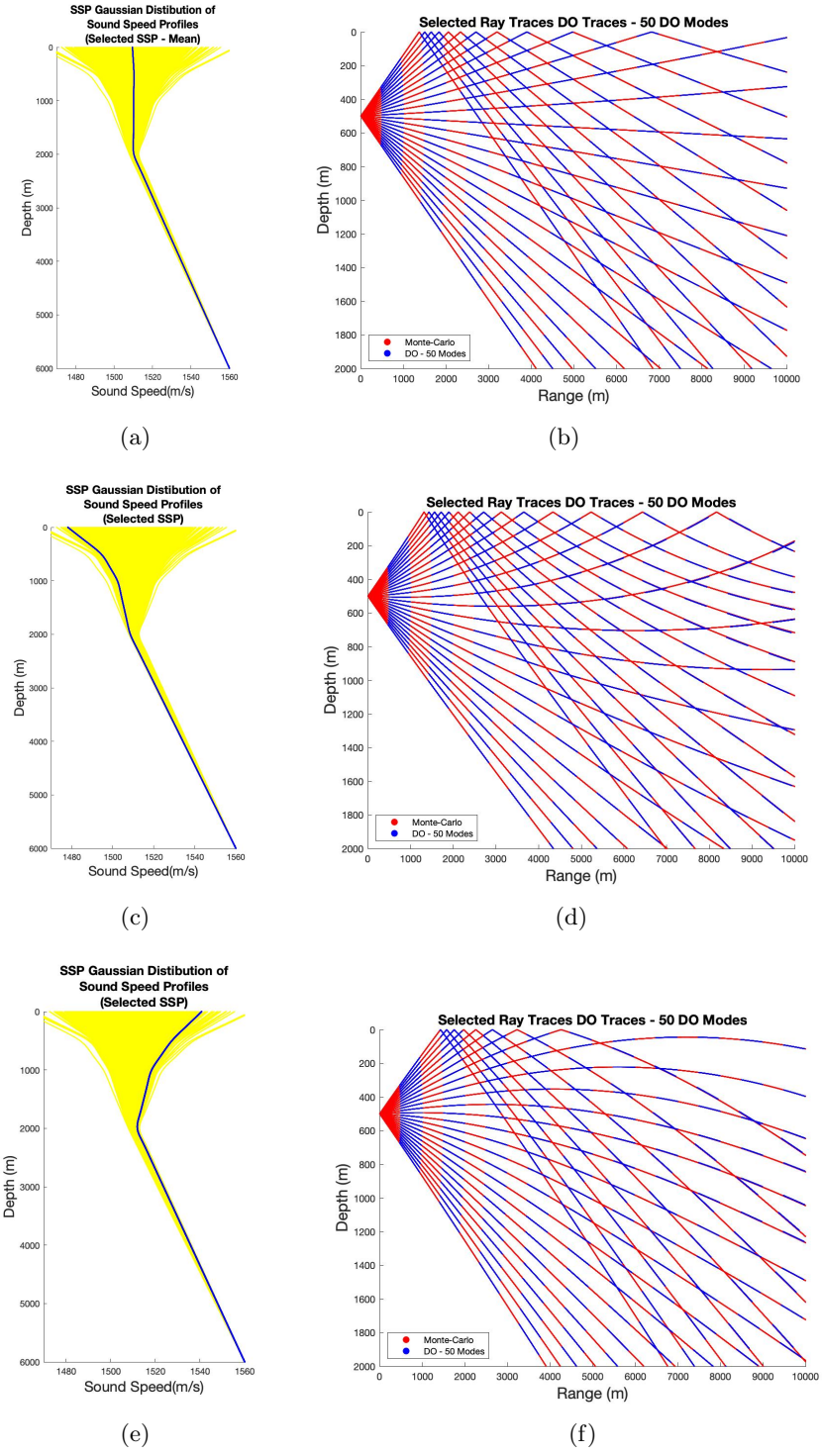

Figure 4-12: Panels (a), (c), and (e) Computed ray traces for highlight SSPs. Panel (b), (d), and (f) show the DO-Ray computed ray trace (50 DO modes) overlaid with deterministic (Monte Carlo) traces. All traces computed using with 1001 Rays (26 Plotted) evenly at evenly spaced angles between $\pm 20^{\circ}$ with a 1m step-size. The deterministic model uses 1st-order Forward Difference computational scheme.

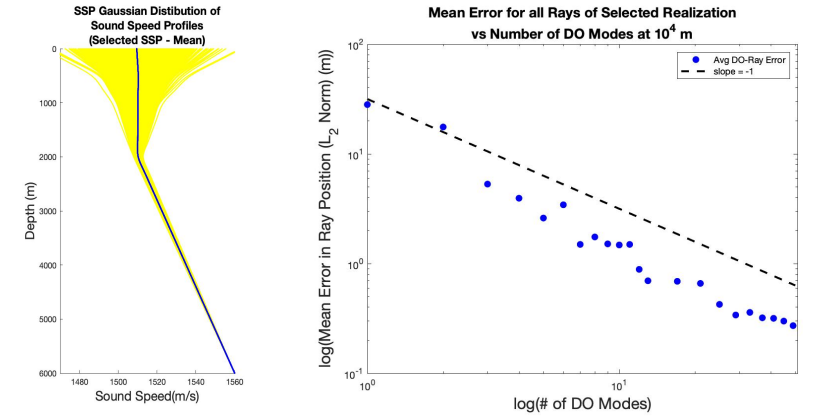

(a) (b)

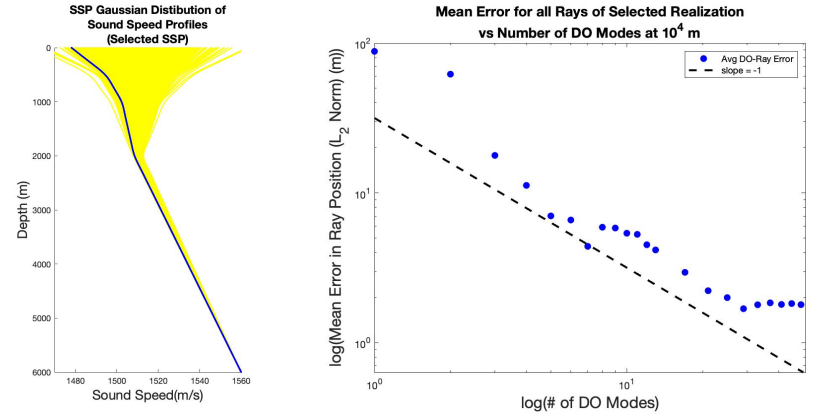

(c) (d)

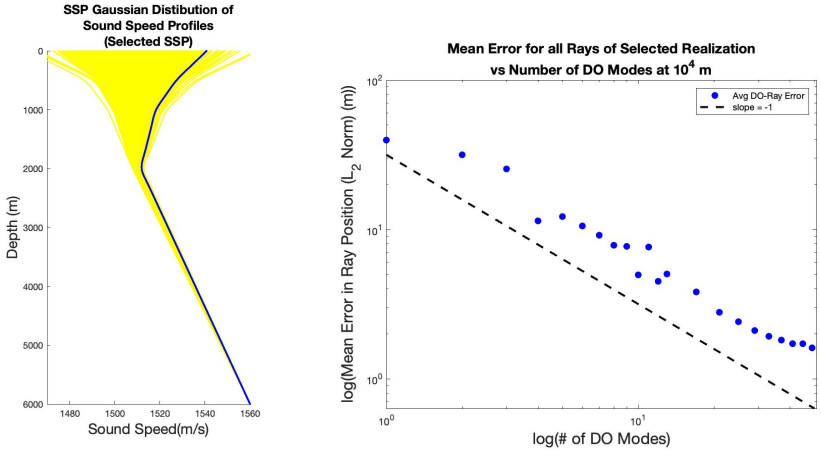

(e) (f)

Figure 4-13: Panels (a), (c), and (e) Computed ray trace ensembles for highlighted SSPs with a varying number of DO modes. Panels (b), (d), and (e) show the convergence for selected realizations of the DO-Ray Methodology with the deterministic solution. First order Convergence Line plotted for Reference. Deterministic traces computed using our deterministic model with 1001 Rays evenly at evenly spaced angles between $\pm 20°$, 1st-order Forward Difference with a 1m step-size.

thermocline, where the decrease in temperature with depth results in a negative sound speed gradient. At a certain depth, the temperature is relatively constant, and pressure becomes the dominant feature resulting in a positive gradient to the sea floor. This is known as the deep isothermal layer and can form a deep sound channel similar to the previous case [23].

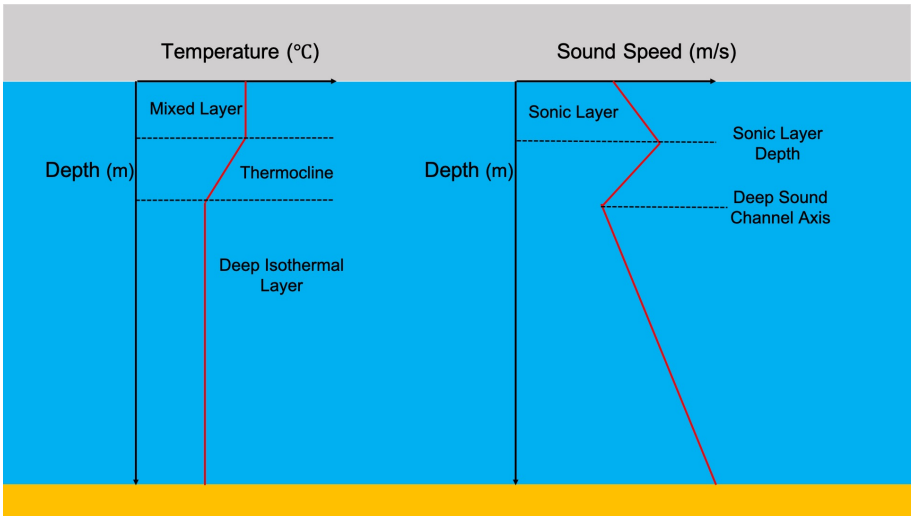

Figure 4-14: Relationship between temperature and sound speed profiles in the deep ocean adapted from [23]. Variation in atmospheric forcing can make the sonic layer depth variable over relatively short temporal scales (hrs or days).

In this test case, we assume uncertainty in the sonic layer depth consist of a Gaussian distribution with a mean layer depth at 250 m. Similarly to the previous test, we show in Figures 4-15 and 4-16 cases our sample distribution as well as computed ray traces for the mean SSP as well as two profiles closer to the edges of our Gaussian distribution. We observe that in all cases we see the characteristic propagation along a surface duct due to the relative sound-speed maximum at the sonic layer depth and the shadow zone created in the vicinity of the sonic layer depth due to the sound energy being refracted away from this depth.

Capturing the Stochastic non-Gaussian Variability

We achieve nearly similar results as observed with the Deep Sound Channel and Constant Gradient SSPs. However, due to the larger changes in the sound speed gradient and the position of the source in the vicinity of the maximum sound speed, we observe greater errors with similar convergence rates.

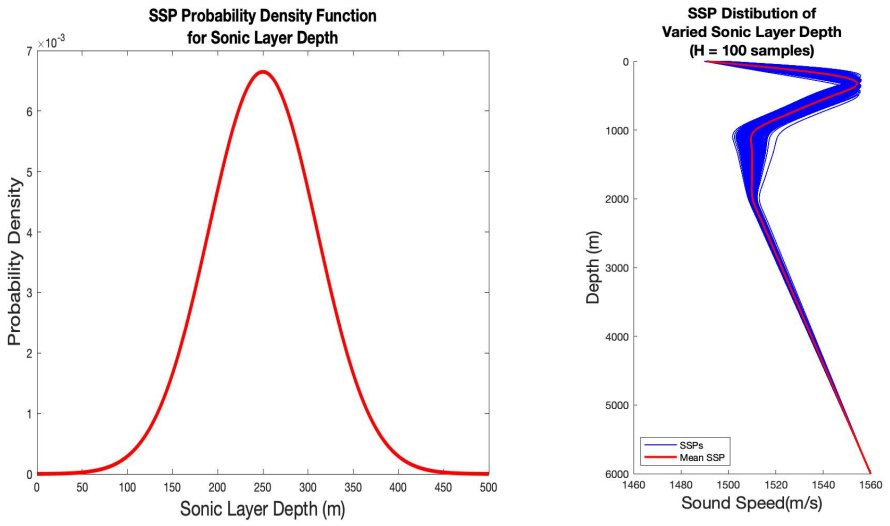

(a) (b)

Figure 4-15: (a) Normal distribution of SSPs characterized by the Sonic Layer Depth with a mean at 250m, (b) from which we can sample to obtain SSP realizations.

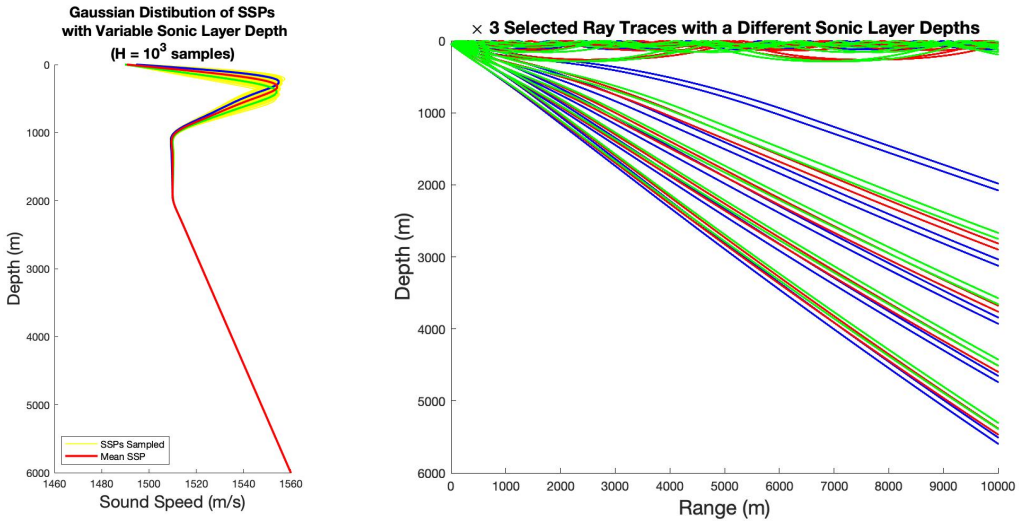

(a) SSP (b) Ray Trace

Figure 4-16: (a) From our SSP distribution of varied Sonic Layer Depths, we sample 1000 SSPs. (b) We computed the associated ray traces for the highlighted red (mean), green and blue SSPs. Ray traces computed using 16 Rays evenly at evenly spaced angles between $\pm 30°$, 1st-order Forward-Difference scheme with a 1m step-size.

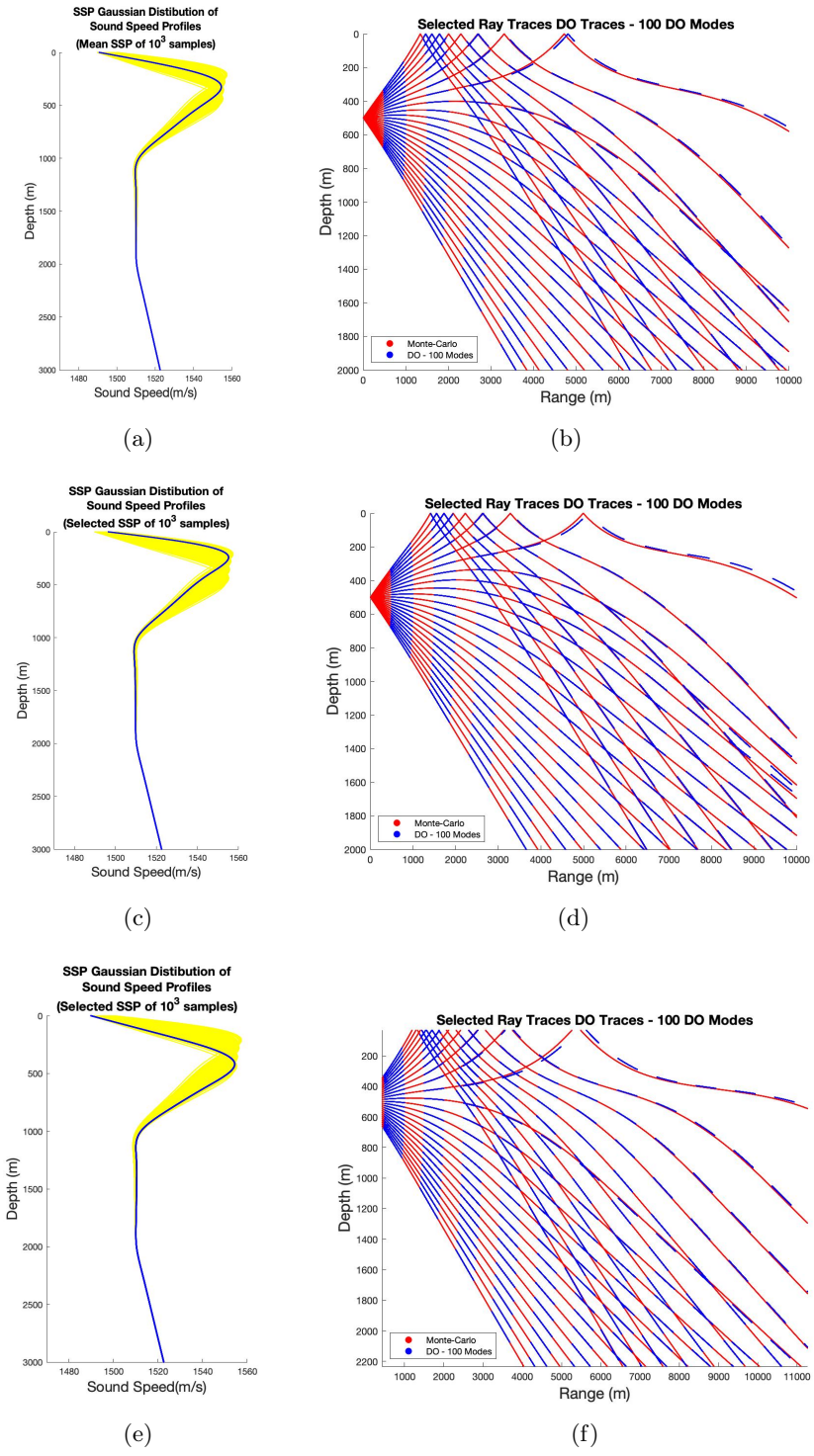

Figure 4-17: Panels (a), (c), and (e) Computed ray traces for highlight SSPs. Panels (b), (d), and (f) show the DO-Ray Computed Ray Trace (100 DO modes) overlaid with deterministic (Monte Carlo) traces. All traces computed using with 1001 Rays (26 plotted) evenly at evenly spaced angles between $\pm 20°$, 1st-order Forward-Difference computational scheme with a 1m step-size.

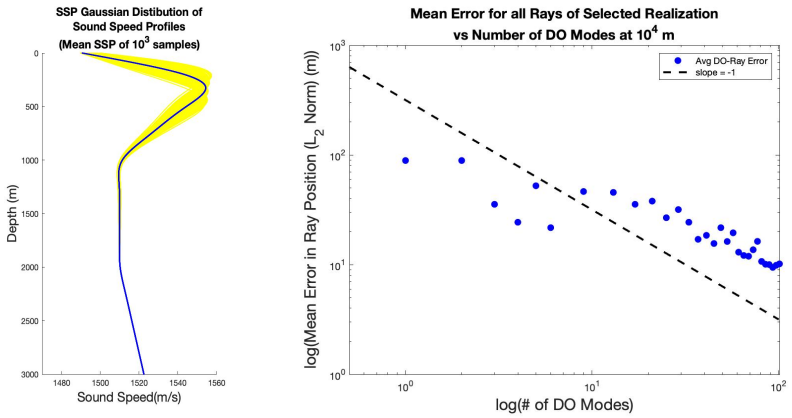

(a) (b)

Figure 4-18: (a) Computed ray trace ensembles for highlighted SSPs with a varying number of DO modes. (b) Convergence for selected realizations of the DO-Ray Methodology with respect to the deterministic solutions. First order Convergence Line is shown for Reference. Realizations computed with 1001 Rays evenly at evenly spaced angles between $\pm 20°$. Deterministic traces computed using our deterministic model 2nd-order Runge-Kutta Forward Difference with a 10^{-2}m step-size.

Chapter 5

Conclusions and Future Work

5.1 Review and Conclusion

Ocean Acoustic computation is inherently challenging. This is compounded when attempting to perform stochastic computations with constrained resources. Innovative computational techniques and reduced order models exist with varying degrees of success. In this work, we reviewed the foundations and several practical methods for acoustic computation: Parabolic Equation, Level Set, and Ray methods. We also reviewed stochastic computational methods to provide uncertainty quantification as well as reduced order models. For the first time, we combined the Ray Method for acoustic computation with the stochastic Dynamically Orthogonal Equations (DO-Ray). We derived the stochastic DO-Ray differential equations, developed related reduced-order algorithms, and demonstrated the ability to predict stochastic ray trace acoustics fields with the dynamically adaptive reduced-rank DO representation.

To provide a basis for evaluating the accuracy of the DO-Ray results, we implemented a deterministic ray tracing model. We validated our deterministic ray tracing computations with both idealized and realistic stochastic environments, in part by observing the expected error convergence rates. We derived the stochastic DO-Ray equations and discussed several of the computational and numerical challenges associated with our present DO-Ray implementation.

Lastly, we applied a DO-Ray methodology to three stochastic ocean scenarios: Constant Gradients, a variable Deep Sound Channel, and a stochastic Sonic-Layer Depth. We observed how the stochastic DO-Ray methodology accurately captures the non-Gaussian

uncertainty in the ocean acoustic environments, even if only a small fraction of the available DO modes is used, using realization-to-realization comparisons. Based on these results, we see that stochastic Ray-Trace field forecasting is feasible with a reduced rank-representation. The remaining challenge is how to make the details of the implementation computationally efficient when compared to a brute force Monte Carlo implementation.

5.2 Future Work

As stated previously, the stochastic DO-Ray methodology as implemented does not offer computational savings, but points to where they are feasible. By evolving the ray field it terms of its mean, DO modes, and DO coefficients, we gain information about the relative importance of the oceans and rays. By using this information, we may be able to either reduce the number of required "look-ups" performed in determining sound speed, reducing the dimension of the state matrices, or some combination of the two. Appendix A provides a more in-depth explanation of this way forward. We also discussed in this thesis the possible use of local approximations to represent the nonlinear ray to sound-speed function transformation, including local sound-speed mean, sound-speed Taylor-Series, and sound-speed function. The use of level-set approaches is also promising to capture all stochastic rays at once [9].

The application of the DO-Ray methodology in realistic 3D ocean acoustic environments is an additional research direction. Assuming the ability to gain efficiencies as described above, further investigation of the numerical schemes and implementation of the developed methodology in a third dimension may offer increased savings.

How uncertainty in the ocean seabed and surface are also topics requiring investigation. Ray trajectories, especially over mesoscale distances, are highly dependent on the ocean floor and surface characteristics. The ability to capture surface and seabed variation in stochastic computation would advance the practical application to stochastic shallow water and under-ice acoustic predictions.

Lastly, this methodology could be coupled with Bayesian Assimilation techniques to improve the forecasting of the ocean and acoustic [76, 43]. This offers advantages over previously mentioned techniques in such as tomography [65], matched field processing [18, 8], by allowing for the richer dynamics-based estimation of non-Gaussian statistics using

stochastic differential physical laws. The results will be a more complete characterization of the coupled probability densities and a more powerful joint estimation of the ocean and acoustic states and their posterior uncertainties, combining multivariate observations with dynamical models based on principled information theory.

THIS PAGE INTENTIONALLY LEFT BLANK

Appendix A

Gaining Computational Efficiency over Monte-Carlo Implementation

We start with a matrix representation of the deterministic implementation for ray tracing:

$$\frac{d\boldsymbol{\Xi}_{r,d}}{ds} = -\mathbf{C}_x. * \nabla_{r,d}\mathbf{C} \tag{A.1}$$

$$\frac{d\mathbf{X}_{r,d}}{ds} = \mathbf{C}. * \boldsymbol{\Xi}_{\boldsymbol{r,d}} \tag{A.2}$$

Using direct integration, to compute the RHS (equation "right-hand-side") at every step "s," we perform four Hadamard products between $R \times H$ matrices along with the required "look-up" functions for matrices of the same size. The entire computation of the RHS for the ray trace ensemble is $R * H * L +$ "sound-speed look-ups", where L is the number of steps. This is referred to as the "MC" cost, or the cost of Monte-Carlo implementation. To better assess where DO-Ray may gain efficiency we characterize its computational cost as:

- *DO*: RHS computed as a reduced-order model (ROM), where reconstructing full realization matrices is not required (i.e. all computations are completed in terms of mean, DO modes and coefficients). Based on discussion in Chapter 3, the lack of mutual information between ray computations in DO-Ray makes this efficiency infeasible with the ray method equations as derived.

- DO_{MC}: A computational cost where by using the information and efficiencies gained with DO-Ray, we obtain computational savings, even though a portion of the RHS

must be computed with Monte-Carlo (e.g. look-up of sound speed for specific realizations).

- MC: Cost of Monte-Carlo implementation.
- $DO+MC$: A computational cost where all of the same matrix multiplications for MC are still done, with the added cost of DO.

$$DO < DO_{MC} < MC < DO + MC \tag{A.3}$$

As described in Chapter 3 and as presently implemented in Chapter 4, the computational cost of our DO-RAY algorithm is characterized as DO+MC. The RHS of the above ODEs must do all of the computations for MC in addition to the added computations of DO. We assess this is due to the step of re-combining the mean, modes and coefficients of $\mathbf{X}$ in order to compute $\mathbf{C}_x$, and $\mathbf{\Xi}_{r,d}$ to perform the required Hadamard products $\mathbf{C}_x. * \mathbf{\Xi}_{r,d}$.

A.1 Possible Solutions and Implementations

Through this work, we know that there exists a reduced representation of the ray trace field. DO-Ray allows us to capture the relative importance of the Rays/Oceans for propagating the wavefronts in space (characterized by the DO modes and coefficients); therefore, we should be able to reduce the computational cost of of the RHS of our ODE's to DO_{MC}. By using the information evolved in the stochastic subspace, we could reduce the number of look-ups required for RHS computation, perform fewer matrix operations, or a combination of the two. The main idea here is to use information stored in the DO modes and coefficients to create a smaller matrix representation (of size $\tilde{R} \times \tilde{H}$ where $\tilde{R} \leq R$ and $\tilde{H} \leq H$) in order to compute the RHS of equations (3.19), (3.21) and (3.24). The use of local approximations to represent the nonlinear ray to sound-speed function transformation, including local sound-speed mean, sound-speed Taylor-Series, and sound-speed function, should lead to the needed efficiency.

A.1.1 Reducing Number of Oceans and/or Rays

Here we assume that some number of oceans ($\tilde{H} < H$) can represent the entirety of realizations. Therefore we could reduce the number of operations by performing look-ups for a

reduced number of oceans and/or rays to compute: $\mathbf{C}$, $\mathbf{C}_x$, and $\nabla\mathbf{C}$. While taking advantage of the DO organization to construct the smaller ensemble is not a trivial task, we can look into the following:

- Reductions through Gaussian-Mixture Model (GMM) Fit of the rays or realizations. We could fit a GMM of DO coefficients obtained at every range step, then use this fit to compute the terms on the RHS.
- Reductions Through Maximum Likelihood Estimator (MLE) of DO Coefficients. Can be done for Rays or Ocean Realizations.
- Reduction by sampling oceans and rays: $\tilde{R} < R$ and $\tilde{H} < H$. Reconstruct the smaller ensemble by clustering the ocean-angles ray realizations of the original ensemble.

By implementing any of the above we hope to reduce the number of "look-up" operations, while maintaining the size of the matrices. This would add the computational cost associated with GMMs, a MLE, or Clustering.

A.1.2 Reduction by Using Ensemble of Ray Traces to Obtain ROM

We could march an ensemble of rays to a specified ray length and evaluate the relative importance. Based on the DO coefficients we pick the rays/oceans that best represent a ROM to continue the evolution of the fields. By doing this we reduce the dimensions of our mean (e.g. $\overline{x}$ becomes $\tilde{R} \times 1$ instead of $R \times 1$), DO modes and coefficients as well as $\mathbf{C}$, $\mathbf{C}_x$, and $\nabla\mathbf{C}$ matrices reducing the number of multiplications at every step. Using DO-Ray information, we reduce the number of look-ups and Matrix products.

We are still faced with how to pick which rays/oceans are relevant based on the DO-Ray terms which is not intuitive. Doing so based on past trends means we will be using assumptions based ray behavior on one section of the SSP. If the rays have not transitioned into highly variable portions of the ocean environments, then the rays picked to be of significance will not accurately represent the variability in the oceans. We also must reform the full representation at a later step (i.e. propagate, then interpolate back between in order to reconstitute the entire ray field).

THIS PAGE INTENTIONALLY LEFT BLANK

Bibliography

[1] Philip Abbot, Ira Dyer, and Chris Emerson. Acoustic propagation uncertainty in the shallow east china sea. *IEEE Journal of Oceanic Engineering*, 31(2):368–383, 2006.

[2] Wael H. Ali and Pierre F. J. Lermusiaux. Acoustics bayesian inversion with gaussian mixture models using the dynamically orthogonal field equations. *TBD*, 2020. In preparation.

[3] Wael H. Ali and Pierre F. J. Lermusiaux. Dynamically orthogonal equations for stochastic underwater sound propagation: Theory, schemes and applications. *TBD*, 2020. In preparation.

[4] Wael Hajj Ali. Dynamically orthogonal equations for stochastic underwater sound propagation. Master's thesis, Massachusetts Institute of Technology, Computation for Design and Optimization Program, Cambridge, Massachusetts, September 2019.

[5] Wael Hajj Ali, Manmeet S. Bhabra, Pierre F. J. Lermusiaux, Andrew March, Joseph R. Edwards, Katherine Rimpau, and Paul Ryu. Stochastic oceanographic-acoustic prediction and Bayesian inversion for wide area ocean floor mapping. In *OCEANS 2019 MTS/IEEE SEATTLE*, pages 1–10, Seattle, October 2019. IEEE.

[6] Wael Hajj Ali, Mohamad H. Mirhi, Abhinav Gupta, Chinmay S. Kulkarni, Corbin Foucart, Manan M. Doshi, Deepak N. Subramani, Chris Mirabito, Patrick J. Haley, Jr., and Pierre F. J. Lermusiaux. Seavizkit: Interactive maps for ocean visualization. In *OCEANS 2019 MTS/IEEE SEATTLE*, pages 1–10, Seattle, October 2019. IEEE.

[7] Arthur B Baggeroer, WA Kuperman, and Henrik Schmidt. Matched field processing: Source localization in correlated noise as an optimum parameter estimation problem. *The Journal of the Acoustical Society of America*, 83(2):571–587, 1988.

[8] Arthur B Baggeroer, William A Kuperman, and Peter N Mikhalevsky. An overview of matched field methods in ocean acoustics. *IEEE Journal of Oceanic Engineering*, 18(4):401–424, 1993.

[9] Manmeet Singh Bhabra. Level set methods for stochastic acoustic modelling. Master's thesis, Massachusetts Institute of Technology CAMBRIDGE, MASSACHUSETTES, inprep.

[10] Leif Bjørnø, Thomas Herbert Neighbors, and David Bradley. *Applied underwater acoustics*. Elsevier, 2017.

[11] Matthew Brand. Fast low-rank modifications of the thin singular value decomposition. *Linear algebra and its applications*, 415(1):20–30, 2006.

[12] Li-Tien Cheng, Myungjoo Kang, Stanley Osher, Hyeseon Shim, and Yen-Hsi Tsai. Reflection in a level set framework for geometric optics. *Computer Modeling in Engineering and Sciences*, 5(4):347–360, 2004.

[13] M. E. G. D. Colin, T. F. Duda, L. A. te Raa, T. van Zon, P. J. Haley, Jr., P. F. J. Lermusiaux, W. G. Leslie, C. Mirabito, F. P. A. Lam, A. E. Newhall, Y.-T. Lin, and J. F. Lynch. Time-evolving acoustic propagation modeling in a complex ocean environment. In *OCEANS - Bergen, 2013 MTS/IEEE*, pages 1–9, 2013.

[14] Bruce D Cornuelle. Acoustic tomography. *IEEE Transactions on Geoscience and Remote Sensing*, GE-20(3):326–332, 1982.

[15] Dennis B Creamer. On using polynomial chaos for modeling uncertainty in acoustic propagation. *The Journal of the Acoustical Society of America*, 119(4):1979–1994, 2006.

[16] Benoit Cushman-Roisin and Jean-Marie Beckers. *Introduction to geophysical fluid dynamics: physical and numerical aspects*. Academic press, 2011.

[17] JA Davis, DeWayne White, and RC Cavanagh. Norda parabolic equation workshop. *Rep. TN-143, Naval Ocean Research and Development Activity, Stennis Space Center, MS*, 1982.

[18] Stan E Dosso. Quantifying uncertainty in geoacoustic inversion. i. a fast gibbs sampler approach. *The Journal of the Acoustical Society of America*, 111(1):129–142, 2002.

[19] T. F. Duda, Y.-T. Lin, A. E. Newhall, K. R. Helfrich, W. G. Zhang, M. Badiey, P. F. J. Lermusiaux, J. A. Colosi, and J. F. Lynch. The “Integrated Ocean Dynamics and Acoustics" (IODA) hybrid modeling effort. In *Proceedings of the international conference on Underwater Acoustics - 2014 (UA2014)*, pages 621–628, 2014.

[20] Timothy F. Duda, Ying-Tsong Lin, Arthur E. Newhall, Karl R. Helfrich, James F. Lynch, Weifeng Gordon Zhang, Pierre F. J. Lermusiaux, and John Wilkin. Multiscale multiphysics data-informed modeling for three-dimensional ocean acoustic simulation and prediction. *Journal of the Acoustical Society of America*, 146(3):1996–2015, September 2019.

[21] Timothy F. Duda, Ying-Tsong Lin, W. Zhang, Bruce D. Cornuelle, and Pierre F. J. Lermusiaux. Computational studies of three-dimensional ocean sound fields in areas of complex seafloor topography and active ocean dynamics. In *Proceedings of the 10th International Conference on Theoretical and Computational Acoustics*, Taipei, Taiwan, 2011.

[22] Timothy F. Duda, Weifeng Gordon Zhang, Karl R. Helfrich, Arthur E. Newhall, Ying-Tsong Lin, James F. Lynch, Pierre F. J. Lermusiaux, Patrick J. Haley, Jr., and John Wilkin. Issues and progress in the prediction of ocean submesoscale features and internal waves. In *OCEANS'14 MTS/IEEE*, 2014.

[23] Paul C Etter. *Underwater acoustic modeling and simulation*. CRC press, 2018.

[24] Florian Feppon and Pierre F. J. Lermusiaux. Dynamically orthogonal numerical schemes for efficient stochastic advection and Lagrangian transport. *SIAM Review*, 60(3):595–625, 2018.

[25] Florian Feppon and Pierre F. J. Lermusiaux. A geometric approach to dynamical model-order reduction. *SIAM Journal on Matrix Analysis and Applications*, 39(1):510–538, 2018.

[26] Steven Finette. Propagation of uncertainty for acoustic fields using polynomial chaos expansions. *The Journal of the Acoustical Society of America*, 114(4):2461–2461, 2003.

[27] Steven Finette. A stochastic response surface formulation of acoustic propagation through an uncertain ocean waveguide environment. *The Journal of the Acoustical Society of America*, 126(5):2242–2247, 2009.

[28] Steven Finette, Marshall H Orr, Altan Turgut, John R Apel, Mohsen Badiey, Chingsang Chiu, Robert H Headrick, John N Kemp, James F Lynch, Arthur E Newhall, et al. Acoustic field variability induced by time evolving internal wave fields. *The Journal of the Acoustical Society of America*, 108(3):957–972, 2000.

[29] Abhinav Gupta, Patrick J. Haley, Deepak N. Subramani, and Pierre F. J. Lermusiaux. Fish modeling and Bayesian learning for the Lakshadweep Islands. In *OCEANS 2019 MTS/IEEE SEATTLE*, pages 1–10, Seattle, October 2019. IEEE.

[30] Robert H Headrick. Basin-scale tidal measurements using acoustic tomography. Technical report, MASSACHUSETTS INST OF TECH CAMBRIDGE, 1990.

[31] Andrew H Jazwinski. Mathematics in science and engineering. *Stochastic processes and filtering theory*, 64, 1970.

[32] Finn B Jensen, William A Kuperman, Michael B Porter, and Henrik Schmidt. *Computational Ocean Acoustics*. Springer Science & Business Media, 2011.

[33] Herman Kahn and Andy W Marshall. Methods of reducing sample size in monte carlo computations. *Journal of the Operations Research Society of America*, 1(5):263–278, 1953.

[34] Joseph B Keller. Rays, waves and asymptotics. *Bulletin of the American mathematical society*, 84(5):727–750, 1978.

[35] Lawrence E Kinsler, Austin R Frey, Alan B Coppens, and James V Sanders. Fundamentals of acoustics. *Fundamentals of Acoustics, 4th Edition, by Lawrence E. Kinsler, Austin R. Frey, Alan B. Coppens, James V. Sanders, pp. 560. ISBN 0-471-84789-5. Wiley-VCH, December 1999.*, page 560, 1999.

[36] Chinmay S. Kulkarni and Pierre F. J. Lermusiaux. Advection without compounding errors through flow map composition. *Journal of Computational Physics*, 398:108859, December 2019.

[37] William A Kuperman and James F Lynch. Shallow-water acoustics. *Physics Today*, 57(10):55–61, 2004.

[38] J Nathan Kutz, Steven L Brunton, Bingni W Brunton, and Joshua L Proctor. *Dynamic mode decomposition: data-driven modeling of complex systems*. SIAM, 2016.

[39] John E Kutzbach. Empirical eigenvectors of sea-level pressure, surface temperature and precipitation complexes over north america. *Journal of Applied Meteorology*, 6(5):791–802, 1967.

[40] Frans-Peter A. Lam, Patrick J. Haley, Jr., Jeroen Janmaat, Pierre F. J. Lermusiaux, Wayne G. Leslie, Mathijs W. Schouten, Lianke A. te Raa, and Michel Rixen. At-sea real-time coupled four-dimensional oceanographic and acoustic forecasts during Battlespace Preparation 2007. *Journal of Marine Systems*, 78(Supplement):S306–S320, November 2009.

[41] Olivier Le Maître and Omar M Knio. *Spectral methods for uncertainty quantification: with applications to computational fluid dynamics*. Springer Science & Business Media, 2010.

[42] P. F. J. Lermusiaux. Data assimilation via Error Subspace Statistical Estimation, part II: Mid-Atlantic Bight shelfbreak front simulations, and ESSE validation. *Monthly Weather Review*, 127(7):1408–1432, July 1999.

[43] P. F. J. Lermusiaux. Uncertainty estimation and prediction for interdisciplinary ocean dynamics. *Journal of Computational Physics*, 217(1):176–199, 2006.

[44] P. F. J Lermusiaux. Adaptive modeling, adaptive data assimilation and adaptive sampling. *Physica D: Nonlinear Phenomena*, 230(1):172–196, 2007.

[45] P. F. J. Lermusiaux and C.-S. Chiu. Four-dimensional data assimilation for coupled physical-acoustical fields. In N. G. Pace and F. B. Jensen, editors, *Acoustic Variability, 2002*, pages 417–424, Saclantcen, 2002. Kluwer Academic Press.

[46] P. F. J. Lermusiaux, C.-S. Chiu, G. G. Gawarkiewicz, P. Abbot, A. R. Robinson, R. N. Miller, P. J. Haley, Jr, W. G. Leslie, S. J. Majumdar, A. Pang, and F. Lekien. Quantifying uncertainties in ocean predictions. *Oceanography*, 19(1):92–105, 2006.

[47] P. F. J. Lermusiaux, C.-S. Chiu, and A. R. Robinson. Modeling uncertainties in the prediction of the acoustic wavefield in a shelfbreak environment. In E.-C. Shang, Q. Li, and T. F. Gao, editors, *Proceedings of the 5th International conference on theoretical and computational acoustics*, pages 191–200. World Scientific Publishing Co., May 21-25 2002. Refereed invited manuscript.

[48] P. F. J. Lermusiaux, P. J. Haley, Jr., S. Jana, A. Gupta, C. S. Kulkarni, C. Mirabito, W. H. Ali, D. N. Subramani, A. Dutt, J. Lin, A. Shcherbina, C. Lee, and A. Gangopadhyay. Optimal planning and sampling predictions for autonomous and Lagrangian platforms and sensors in the northern Arabian Sea. *Oceanography*, 30(2):172–185, June 2017. Special issue on Autonomous and Lagrangian Platforms and Sensors (ALPS).

[49] P. F. J. Lermusiaux, A. R. Robinson, P. J. Haley, and W. G. Leslie. Advanced interdisciplinary data assimilation: Filtering and smoothing via error subspace statistical estimation. In *Proceedings of The OCEANS 2002 MTS/IEEE conference*, pages 795–802. Holland Publications, 2002.

[50] P. F. J. Lermusiaux, D. N. Subramani, J. Lin, C. S. Kulkarni, A. Gupta, A. Dutt, T. Lolla, P. J. Haley, Jr., W. H. Ali, C. Mirabito, and S. Jana. A future for intelligent autonomous ocean observing systems. *Journal of Marine Research*, 75(6):765–813, November 2017. The Sea. Volume 17, The Science of Ocean Prediction, Part 2.

[51] Pierre Lermusiaux. *Error subspace data assimilation methods for ocean field estimation: theory, validation and applications*. PhD thesis, Harvard University, Cambridge, Massachusetts, September 1997.

[52] Pierre F. J. Lermusiaux and A. R. Robinson. Data assimilation via Error Subspace Statistical Estimation, part I: Theory and schemes. *Monthly Weather Review*, 127(7):1385–1407, 1999.

[53] Pierre F. J. Lermusiaux, Jinshan Xu, Chi-Fang Chen, Sen Jan, L.Y. Chiu, and Yiing-Jang Yang. Coupled ocean–acoustic prediction of transmission loss in a continental shelfbreak region: Predictive skill, uncertainty quantification, and dynamical sensitivities. *IEEE Journal of Oceanic Engineering*, 35(4):895–916, October 2010.

[54] W. G. Leslie, P. J. Haley, Jr., P. F. J. Lermusiaux, M. P. Ueckermann, O. Logutov, and J. Xu. MSEAS Manual. MSEAS Report 06, Department of Mechanical Engineering, Massachusetts Institute of Technology, Cambridge, MA, 2010.

[55] Jing Lin and Pierre F. J. Lermusiaux. Minimum-correction second-moment matching: Theory, algorithms and applications. *Numerische Mathematik*, 2020. Sub-judice.

[56] Ying-Tsong Lin, A. E. Newhall, T. F. Duda, P. F. J. Lermusiaux, and P. J. Haley. Merging multiple-partial-depth data time series using objective empirical orthogonal function fitting. *IEEE Journal of Oceanic Engineering*, 35(4):710–721, October 2010.

[57] T. Lolla and P. F. J. Lermusiaux. A Gaussian mixture model smoother for continuous nonlinear stochastic dynamical systems: Applications. *Monthly Weather Review*, 145:2763–2790, July 2017.

[58] T. Lolla and P. F. J. Lermusiaux. A Gaussian mixture model smoother for continuous nonlinear stochastic dynamical systems: Theory and scheme. *Monthly Weather Review*, 145:2743–2761, July 2017.

[59] T. Lolla, P. F. J. Lermusiaux, M. P. Ueckermann, and P. J. Haley, Jr. Time-optimal path planning in dynamic flows using level set equations: Theory and schemes. *Ocean Dynamics*, 64(10):1373–1397, 2014.

[60] Tapovan Lolla, Mattheus P. Ueckermann, Konur Yiğit, Patrick J. Haley, Jr., and Pierre F. J. Lermusiaux. Path planning in time dependent flow fields using level set methods. In *IEEE International Conference on Robotics and Automation (ICRA), 14-18 May 2012*, pages 166–173, 2012.

[61] Edward N Lorenz. Empirical orthogonal functions and statistical weather prediction. *Tech. Report. Stat. Forecast Proj. Report. 1 Dep. Meteorol.*, 1956.

[62] Sheri L Martinelli. An application of the level set method to underwater acoustic propagation. *Communications in Computational Physics*, 12(5):1359–1391, 2012.

[63] Sheri Lynn Martinelli. *A Level-Sets-Based Wavefront Propagation Method for Underwater Acoustics*. PhD thesis, Brown University PROVIDENCE, RHODE ISLAND, 2012.

[64] Herman Medwin and Clarence S Clay. *Fundamentals of acoustical oceanography*. Academic press, 1997.

[65] Walter Munk, Peter Worcester, and Carl Wunsch. *Ocean acoustic tomography*. Cambridge university press, 2009.

[66] Gerald R North. Empirical orthogonal functions and normal modes. *Journal of the Atmospheric Sciences*, 41(5):879–887, 1984.

[67] Office of Naval Research. Task force ocean broad area announcement. unpublished, 2019.

[68] Stanley Osher, Li-Tien Cheng, Myungjoo Kang, Hyeseon Shim, and Yen-Hsi Tsai. Geometric optics in a phase-space-based level set and eulerian framework. *Journal of Computational Physics*, 179(2):622–648, 2002.

[69] Antares Parvulescu. Matched-signal ("mess") processing by the ocean. *The Journal of the Acoustical Society of America*, 98(2):943–960, 1995.

[70] Akash Phadnis. Uncertainty quantification and prediction for non-autonomous linear and nonlinear systems. Master's thesis, Massachusetts Institute of Technology, Department of Mechanical Engineering, Cambridge, Massachusetts, September 2013.

[71] Michael B Porter and A Tolstoy. The matched field processing benchmark problems. *Journal of Computational Acoustics*, 2(03):161–185, 1994.

[72] Purnima Ratilal and Nicholas C Makris. Mean and covariance of the forward field propagated through a stratified ocean waveguide with three-dimensional random inhomogeneities. *The Journal of the Acoustical Society of America*, 118(6):3532–3559, 2005.

[73] John M Richardson. A design for maintaining maritime superiority. *Naval War College Review*, 69(2):4, 2016.

[74] H Bryan Riley and John A Tague. Matched field processing: An overview. In *The 24th Southeastern Symposium on System Theory and The 3rd Annual Symposium on Communications, Signal Processing Expert Systems, and ASIC VLSI Design*, pages 180–184. IEEE, 1992.

[75] A. R. Robinson, P. J. Haley, P. F. J. Lermusiaux, and W. G. Leslie. Predictive skill, predictive capability and predictability in ocean forecasting. In *Proceedings of "The OCEANS 2002 MTS/IEEE" conference*, pages 787–794. Holland Publications, September 2002.

[76] A. R. Robinson and P. F. J. Lermusiaux. Prediction systems with data assimilation for coupled ocean science and ocean acoustics. In A. Tolstoy et al, editor, *Proceedings of the Sixth International Conference on Theoretical and Computational Acoustics*, pages 325–342. World Scientific Publishing, 2004. Refereed invited Keynote Manuscript.

[77] A. R. Robinson, P. F. J. Lermusiaux, and N. Q. Sloan III. Data assimilation. In Kenneth H. Brink and Allan R. Robinson, editors, *The Global Coastal Ocean-Processes and Methods*, volume 10 of *The Sea*, chapter 20, pages 541–594. John Wiley and Sons, New York, 1998.

[78] Themistoklis P. Sapsis and Pierre F. J. Lermusiaux. Dynamically orthogonal field equations for continuous stochastic dynamical systems. *Physica D: Nonlinear Phenomena*, 238(23–24):2347–2360, December 2009.

[79] Themistoklis P. Sapsis and Pierre F. J. Lermusiaux. Dynamical criteria for the evolution of the stochastic dimensionality in flows with uncertainty. *Physica D: Nonlinear Phenomena*, 241(1):60–76, 2012.

[80] T. Sondergaard and P. F. J. Lermusiaux. Data assimilation with Gaussian Mixture Models using the Dynamically Orthogonal field equations. Part I: Theory and scheme. *Monthly Weather Review*, 141(6):1737–1760, 2013.

[81] T. Sondergaard and P. F. J. Lermusiaux. Data assimilation with Gaussian Mixture Models using the Dynamically Orthogonal field equations. Part II: Applications. *Monthly Weather Review*, 141(6):1761–1785, 2013.

[82] D. N. Subramani, P. J. Haley, Jr., and P. F. J. Lermusiaux. Energy-optimal path planning in the coastal ocean. *Journal of Geophysical Research: Oceans*, 122:3981–4003, 2017.

[83] D. N. Subramani and P. F. J. Lermusiaux. Energy-optimal path planning by stochastic dynamically orthogonal level-set optimization. *Ocean Modeling*, 100:57–77, 2016.

[84] D. N. Subramani, T. Lolla, P. J. Haley, Jr., and P. F. J. Lermusiaux. A stochastic optimization method for energy-based path planning. In S. Ravela and A. Sandu, editors, *DyDESS 2014*, volume 8964 of *LNCS*, pages 1–12. Springer, 2015.

[85] D. N. Subramani, Q. J. Wei, and P. F. J. Lermusiaux. Stochastic time-optimal path-planning in uncertain, strong, and dynamic flows. *Computer Methods in Applied Mechanics and Engineering*, 333:218–237, 2018.

[86] Deepak Subramani and P. F. J. Lermusiaux. Probabilistic ocean predictions with dynamically-orthogonal primitive equations. *In preparation*, 2020.

[87] Deepak N. Subramani and Pierre F. J. Lermusiaux. Risk-optimal path planning in stochastic dynamic environments. *Computer Methods in Applied Mechanics and Engineering*, 353:391–415, August 2019.

[88] Deepak Narayanan Subramani. *Probabilistic Regional Ocean Predictions: Stochastic Fields and Optimal Planning*. PhD thesis, Massachusetts Institute of Technology, Department of Mechanical Engineering, Cambridge, Massachusetts, February 2018.

[89] Matthew Michael Swezey. Ocean acoustic uncertainty for submarine applications. Master's thesis, Massachusetts Institute of Technology, Department of Mechanical Engineering, Cambridge, Massachusetts, June 2016.

[90] FD Tappert. Parabolic equation method in underwater acoustics. *The Journal of the Acoustical Society of America*, 55(S1):S34–S34, 1974.

[91] Fred D Tappert. The parabolic approximation method. In *Wave propagation and underwater acoustics*, pages 224–287. Springer, 1977.

[92] Aaron M Thode, GL D'Spain, and WA Kuperman. Matched-field processing, geoacoustic inversion, and source signature recovery of blue whale vocalizations. *The Journal of the Acoustical Society of America*, 107(3):1286–1300, 2000.

[93] A Tolstoy. Linearization of the matched field processing approach to acoustic tomography. *The Journal of the Acoustical Society of America*, 91(2):781–787, 1992.

[94] A Tolstoy, O Diachok, and LN Frazer. Acoustic tomography via matched field processing. *The Journal of the Acoustical Society of America*, 89(3):1119–1127, 1991.

[95] Alexandra Tolstoy. *Matched field processing for underwater acoustics*. World Scientific, 1993.

[96] M. P. Ueckermann, P. F. J. Lermusiaux, and T. P. Sapsis. Numerical Schemes and Studies for Dynamically Orthogonal Equations of Stochastic Fluid and Ocean Flows. MSEAS Report 11, Department of Mechanical Engineering, Massachusetts Institute of Technology, Cambridge, MA, 2011.

[97] M. P. Ueckermann, P. F. J. Lermusiaux, and T. P. Sapsis. Numerical schemes for dynamically orthogonal equations of stochastic fluid and ocean flows. *Journal of Computational Physics*, 233:272–294, January 2013.

[98] V Vinje, E Iversen, K Åstebøl, and H Gjøystdal. Estimation of multivalued arrivals in 3d models using wavefront construction—part i 1. *Geophysical Prospecting*, 44(5):819–842, 1996.

[99] D. Wang, P. F. J. Lermusiaux, P. J. Haley, W. G. Leslie, and H. Schmidt. Adaptive acoustical-environmental assessment for the focused acoustic field-05 at-sea exercise. In *Oceans 2006*, page 6, Boston, MA, 18-21 Sept 2006.

[100] Ding Wang, Pierre F. J. Lermusiaux, Patrick J. Haley, Jr., Donald Eickstedt, Wayne G. Leslie, and Henrik Schmidt. Acoustically focused adaptive sampling and on-board routing for marine rapid environmental assessment. *Journal of Marine Systems*, 78(Supplement):S393–S407, November 2009.

[101] Anne-Cathrin Wölfl, Helen Snaith, Sam Amirebrahimi, Colin W Devey, Boris Dorschel, Vicki Ferrini, Veerle AI Huvenne, Martin Jakobsson, Jennifer Jencks, Gordon Johnston, et al. Seafloor mapping–the challenge of a truly global ocean bathymetry. *Frontiers in Marine Science*, 6:283, 2019.

[102] J. Xu, P. F. J. Lermusiaux, P. J. Haley Jr., W. G. Leslie, and O. G. Logutov. Spatial and Temporal Variations in Acoustic propagation during the PLUSNet-07 Exercise in Dabob Bay. In *Proceedings of Meetings on Acoustics (POMA)*, volume 4, page 11. Acoustical Society of America 155th Meeting, 2008.

[103] Wen Xu and Henrik Schmidt. System-orthogonal functions for sound speed profile perturbation. *IEEE Journal of Oceanic Engineering*, 31(1):156–169, 2006.